AB INITIO STUDY OF THE WORK FUNCTIONS OF ELEMENTAL METAL CRYSTALS

THÈSE N° 1955 (1999)

PRÉSENTÉE AU DÉPARTEMENT DE PHYSIQUE

ÉCOLE POLYTECHNIQUE FÉDÉRALE DE LAUSANNE

POUR L'OBTENTION DU GRADE DE DOCTEUR ÈS SCIENCES

PAR

Caspar FALL
Ingénieur physicien diplômé EPFL
de nationalité britannique

acceptée sur proposition du jury:

Prof. A. Baldereschi, directeur de thèse
Dr W. Andreoni, corapporteur
Prof. F. Bassani, corapporteur
Dr N. Binggeli, corapporteur
Prof. K. Kern, corapporteur

Lausanne, EPFL
1999

Version Abrégée

CETTE thèse s'inscrit dans le cadre de l'étude théorique des surfaces de métaux. Nous calculons de manière quantique, *ab initio*, les propriétés électroniques de surfaces propres de métaux élémentaires en tenant compte de la structure atomique du matériau. Notre but est de comprendre les mécanismes atomiques responsables de la dépendance du potentiel d'extraction avec la géométrie de la surface, en tenant compte de son orientation cristallographique, de la relaxation et de la reconstruction atomique, ainsi que de l'effet des arêtes cristallines.

Nous présentons une méthode stable pour obtenir le potentiel d'extraction à partir de calculs auto-consistants dans une géométrie en couche mince. En appliquant une technique basée sur une moyenne macroscopique, nous pouvons mesurer précisement le saut de potentiel électrostatique à la surface du métal. En combinant cette grandeur avec le niveau de Fermi d'un crystal de taille infinie, nous pouvons réduire les effets de taille sur le potentiel d'extraction et en determiner des valeurs très précises.

L'origine microscopique de l'anisotropie du potentiel d'extraction est approfondie pour le sodium, l'aluminium, le cuivre et l'or. Pour ces métaux, nous montrons que les faces principales, classés par potentiel d'extraction croissant, sont dans le même ordre que les valeurs expérimentales et que l'ordre dans l'aluminium est différent que dans la plupart des autres métaux. L'origine de l'anisotropie du potentiel d'extraction est reliée à la nature orbitale des états électroniques au niveau de Fermi.

Cette étude de surfaces métalliques est étendue à des facettes cristallines finies. Par des calculs de la structure électronique de nano-fils à partir de principes premiers, nous obtenons la variation du potentiel électrostatique à l'extérieur de plusieurs arêtes cristallines infiniment longues. Nous mettons en évidence le mécanisme microscopique qui permet à deux potentiels d'extraction différents de coexister de part et d'autre d'une même arête.

Mots clés: Surfaces métalliques, propriétés électroniques, potentiel d'extraction, fonctionnelle de densité.

Abstract

THIS thesis is concerned with the theoretical study of the physical characteristics of metallic surfaces. *Ab initio* quantum calculations are performed to determine the electronic properties of clean elemental metal surfaces, fully accounting for the material's atomic structure. We aim to understand the atomic-scale mechanisms responsible for the dependence of the work function on the surface geometry, including the crystallographic orientation of the surface, the atomic relaxation and reconstruction, as well as the effect of surface edges.

We present an accurate method to derive work functions from self-consistent thin-film calculations. By applying a technique based on a macroscopic average, we filter the atomic oscillations in the electronic density to measure precisely the electrostatic potential step at the crystal surface. Combining this quantity with the Fermi energy of a bulk crystal is shown to reduce size effects on the work functions and to yield very precise values.

The microscopic origin of the work function anisotropy is studied in sodium, aluminium, copper and gold. For these metals, we find that the trends of increasing work functions for the principal surface orientations reproduce the experimental data and that the trend in aluminium is different from most other metals. The origin of the work function anisotropy is discussed in relation with the orbital character of the electronic states at the Fermi energy.

Our study of metal surfaces is extended to the facets of a finite crystal. First-principles studies of the electronic structure of nanowires enable us to obtain the electrostatic potential outside a variety of infinitely-long facet edges. In particular, we determine the microscopic mechanism that allows two different work functions to coexist on either side of a facet edge.

Keywords: Metal surfaces, electronic properties, work function, density functional calculations.

Sometimes there are airs grave and gentle,
Religious, or, perhaps, sentimental,
    Or the limerick's lyric,
    Or else panegyric,
Or struggles with things elemental.

E. O. Parrott

Contents

List of Figures

List of Tables

On a tropical beach walked Niels Bohr,
Transfixed by the waves flowing pure.
    Then he looked at the sand,
    And thought it quite grand
How those waves met the grains at the shore.

David Morin, Eric Zaslow, E'beth Haley, John Golden, and Nathan Salwen

Chapter 1

Introduction

THE work function, which is the minimum energy required to extract an electron from a crystal, is one of the most fundamental parameters of metal surfaces, and is important to understand a wide range of physical phenomena, such as adsorption, catalysis promotion, photoemission and thermionic emission processes. The first measurements of work functions were performed at the beginning of this century, notably by Langmuir, to gain fundamental insights into the electronic properties of metals and to improve on cathodes employed by the developing electric light industry. The quest for stable thermionic sources and sensitive photodetectors then drove further research into work functions.

Nowadays, with the development of ultra-high vacuum techniques, clean and stable metallic surfaces can be produced, allowing reproducible surface conditions to be obtained. Accurate values of the work functions of most metals have thus been established [1, 2]. With the adsorption of atoms or molecules, the surface electronic structure is modified and the work function can change by several eV. Since work function changes as small as a few meV can be measured, low densities of adsorbates can be identified and monitored. The work function thus also serves as a sensitive diagnostic of structural and chemical surface conditions. In this work, as a first step, we study theoretically the work functions of clean surfaces, without any adsorbates.

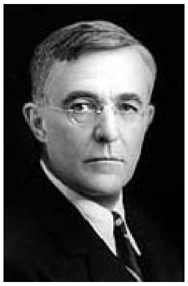

I. Langmuir
1881–1957

Work functions of metals generally depend on the crystalline orientation of the surface, a phenomenon known as the work function anisotropy. Experimentally, the work function was first seen to depend on the crystallographic surface plane in tungsten monocrystals. Studies of other elemental face-centered and body-centered cubic metals have confirmed that a significant fraction of the work function, up to approximately 15%, can differ between two clean low-index surfaces of the same metal.

Work functions and their anisotropies have been the focus of a number of early models, based on phenomenological observations [3] or model systems [4, 5]. These results served to highlight trends in the work functions of different materials. Present-day state-of-the-art theoretical investigations have improved upon these simplified models but have nevertheless failed to resolve a number of issues satisfactorily. In particular, a quantitative theoretical understanding of the origin of the work function anisotropy is lacking for most metals. A global trend of increasing work function with the packing density of the surface plane has been noted experimentally for clean surfaces, but is not present in some metals, such as aluminium. This anomaly, observed in a common simple *sp* metal, has not been resolved up to now. More generally, the mechanisms controlling the ordering of the work functions of the principle surface orientations have not been fully explained and current understanding for most metals is based on simplified models [5–8] that generally lack self-consistency.

The local work function, which is defined as the energy required to take an electron from the Fermi level to a specified position outside the metal, is another important quantity for understanding and modelling electron emission experiments. The exact calculation of the local work function is a complex theoretical problem that must take into account long-range many-body effects such as the image force. As yet, theoretical investigations of real metal surfaces accounting for the image potential have only focused on infinitely-extended planes [9]. To our knowledge, the influence of the crystal morphology on the local work function outside finite crystals has not been studied extensively.

Indeed, most theoretical investigations of work functions have treated surfaces of infinite lateral extent. While such an approximation is presumably valid in the centre of a real crystal facet, effects resulting from the finite dimensions of the facets should be apparent close to facet edges and have only been discussed using jellium surfaces [10]. The coexistence of different work functions around adjacent non-equivalent facets of a monocrystal has not been addressed satisfactorily on a microscopic scale up to now.

At the surface, due to the absence of half the ionic neighbours, the interatomic forces are modified and the equilibrium positions of the surface ions change in consequence. Metal surfaces generally exhibit a modification of the inter-layer spacing at the surface, known as the surface relaxation, or sometimes, as on low-index gold surfaces, show a top ionic layer of different symmetry from the underlying bulk arrangement, a process known as a surface reconstruction. Surface relaxations, and to a greater extent, surface reconstructions, modify the ionic and electronic charge densities in the surface region. These rearrangements are expected to change the work function, but have not often been taken into account in previous studies.

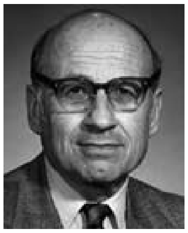

W. Kohn
Nobel 1998

The development of density functional theory (DFT) and of the local density approximation (LDA), both introduced by Kohn in the 1960s [11, 12], have provided a framework for the calculation of the electronic properties of atoms, molecules and solids. With present-day numerical means, the determination *ab initio* of the self-consistent microscopic arrangement of charge at a crystalline metallic surface is a realistic proposition. DFT calculations can provide, in principle exactly, the ground-state self-consistent charge density at a metal surface. The work function can be determined from the electronic charge density, provided the Fermi energy of the system is also known. If the calculations are performed with sufficient care, we can take advantage of the short screening lengths in metals and calculate accurate work functions using only a limited number of atomic planes. In this thesis, we perform first principles calculations of a number of metal surfaces in different geometries. By focusing on model systems such as extended clean surfaces, *ab initio* calculations can provide new approaches to some of the open issues presented above and bring insights into the salient features necessary to interpret more realistic complex surfaces.

This work is organised as follows: in Chapter 2 we present a phenomenological introduction to metal surfaces and present in detail the trends and models identified previously. We review the experimental work functions that are available at the present time, as well as the experimental techniques employed. In Chapter 3, we detail the theoretical procedure employed here, based on DFT-LDA, and cover the approach for dealing with extended systems and many-electron atoms. The application of these theories to metal surfaces, by means of the thin-slab technique, is presented in Chapter 4, where we compare various calculational approaches for determining work functions. In Chapter 5, we perform work function calculations for the principle surface orientations of a number of typical metals and discuss the origins of the different work function anisotropies. We consider finite nanocrystals in Chapter 6, where we have performed first-principles calculations to study the local potential outside sharp facet edges. Finally, our conclusions are detailed in Chapter 7.

‘‘It’s here, right under your nose!’’
‘‘Just arrange the whole thing in rows.’’
    ‘‘Put hydrogen here,’’
    Dmitri would cheer,
‘‘And tungsten down by your toes.’’

Devlin Gualtieri

Indeterminism

Is nature so fickle, my friend,
an indefinite future t’portend?
    ‘‘Well they say it is so
    ’cause experiments show
Probability reigns in the end.’’

William Rolnick

Chapter 2

Metal surface phenomenology

In this chapter, we introduce some general aspects of the phenomenology of clean metal surfaces. We present the basic electronic quantities characterising metal surfaces—among which the work function is the most fundamental—and discuss some of the trends identified by previous authors. In particular, we consider properties such as the local work function and the work-function anisotropy, and we discuss qualitatively the effect of work function anisotropies on the potential outside finite monocrystals. Theoretical models of work function anisotropies are discussed in light of Smoluchowski's smoothing principle and the linear theory of Lang and Kohn. Finally, we turn to a brief review of experiments and techniques that have allowed work functions to be measured.

2.1 Work function definition and trends

J. Bardeen
1908–1991

The work function W of a metal may be defined as the difference in energy between a neutral crystal and the same crystal with one electron removed. This definition calls for zero temperature and a perfect vacuum, since it is assumed that the metal is in its ground state, both before and after the electron removal. The work function was first defined in this way by Wigner and Bardeen in 1935 [13].

The work function corresponds to the minimum energy necessary to extract an electron from the metal [14]. For a crystal with N electrons, if E_N is the initial energy of the metal and E_{N-1} that of the metal with one electron removed to a region of electrostatic potential V_e, we define:[1]

$$W = (E_{N-1} + V_e) - E_N. \tag{2.1}$$

---

[1] When studying work functions, it is convenient to give the potentials directly as a potential energy for electrons. This leads to an opposite sign convention for the potential than in classical electrodynamics.

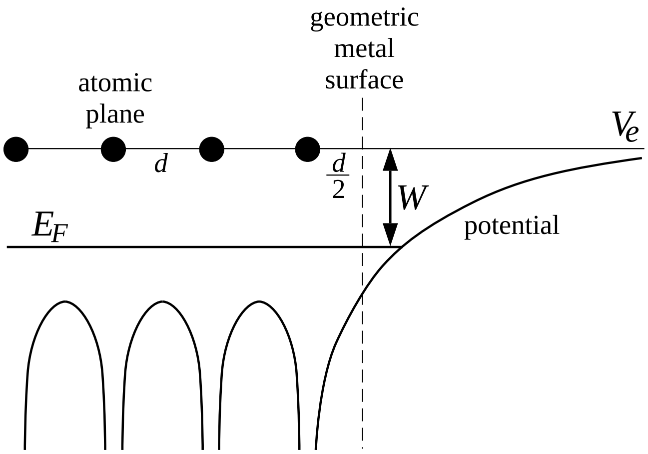

Figure 2.1: The work function W is given by the difference between the Fermi energy E_F and the external potential at infinity V_e. The potential (solid curve) diverges at the atomic centres (black circles). The metallic surface is often defined half an interplanar distance d beyond the last atomic plane (dashed line).

The removed electron is assumed to be at rest, and therefore possesses only potential energy. At zero temperature, the chemical potential μ is by definition $\mu = E_N - E_{N-1}$. In the limit of large systems, all polarisation effects can be neglected after removing the electron. The chemical potential is then shown to coincide with the Fermi energy E_F [15], which is defined as the maximum energy of the electrons in the metal. Using these identities, the following exact expression for the work function W of a metal is obtained:[2]

$$\boxed{W = V_e - E_F} \tag{2.2}$$

The work function is equal to the potential difference between the Fermi energy and the electrostatic potential outside the metal (at an infinite distance), as shown in Figure 2.1 for an infinitely-extended crystalline surface. Such a clean surface can be imagined to result from the cleavage of a perfectly-pure single crystal into two parts. In the absence of spontaneous surface reconstruction, the resulting rigorously-flat crystalline surface constitutes the ideal condition usually taken for the definition of the work function. For finite surfaces, the work function must be measured far enough from the surface to avoid image effects (see Section 2.2) but at a distance significantly smaller than the typical dimensions of the sample (see Section 2.3).

The absolute values of the two terms on the right-hand side of Equation 2.2 depend on the reference energy (often chosen as the average electrostatic potential in the metal $<V>$). The position of the Fermi energy E_F with respect to the average electrostatic potential $<V>$, which we write $\varepsilon_F = E_F - <V>$, is a term controlled by the bulk properties of the metal. At the surface, the spreading of

---

[2] For macroscopic metallic crystals, the work function is also equal to the crystalline electron affinity, which describes the energy gained on binding a supplementary electron.

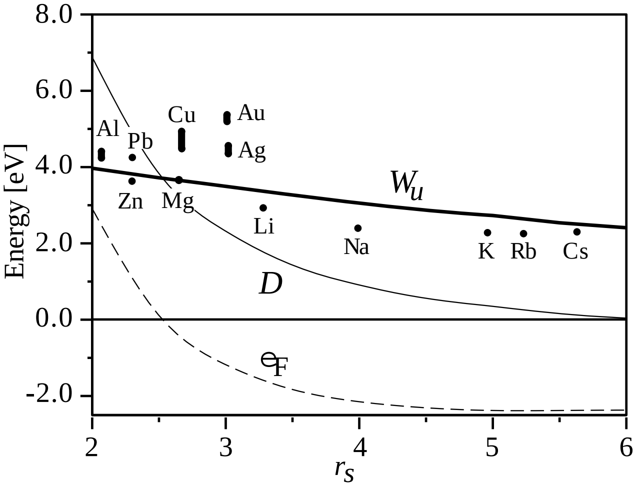

Figure 2.2: Jellium work function (W_u) as a function of the electronic density parameter r_s. The work function is equal to the difference between the surface dipole (D) and the Fermi energy (ε_F), both referred to the average electrostatic potential in the jellium. Experimental work functions of selected simple and noble metals are indicated by circles and vertical bars (which show the range in orientation-dependent work functions). This figure is based on theoretical data from Reference [4].

the electronic charge into the vacuum is equivalent to the presence of a double layer of charge, which induces a potential step $D = V_e - <V>$ that the electrons must overcome to leave the metal [16].

Lang and Kohn calculated the work functions of jellium surfaces using this separation into two components [4]. In Figure 2.2, we display the Fermi energy ε_F and the surface dipole D, referenced to the average electrostatic potential in the jellium, as well as the work function $W_u = D - \varepsilon_F$, as a function of the parameter r_s, which is related to the electron density n through $\frac{4\pi}{3}(r_s a_0)^3 = n^{-1}$, where a_0 is the Bohr radius. As the electronic density is increased, the work function remains between 3 and 4 eV, even though D and ε_F vary strongly. A comparison of the jellium results with the experimental work functions of some simple metals shows a similar increasing trend with the electronic density. For noble metals, the work functions computed with this model are too low by at least 1.5 eV.

Trends in the work functions of elemental metals have been noticed to follow similar periodicities to the electronic structure of atoms [1]. A number of empirical studies have exhibited correlations between work functions and the power of atoms to attract electrons to themselves. In quantitative terms, the electronegativity χ, defined from atomic spectra as the average of the ionisation energy and the electron affinity, provides a suitable measure of electron attraction in free atoms [3]. Michaelson corrected the electronegativity by an empirical periodicity parameter P, specific to each subgroup of elements in a column of the periodic

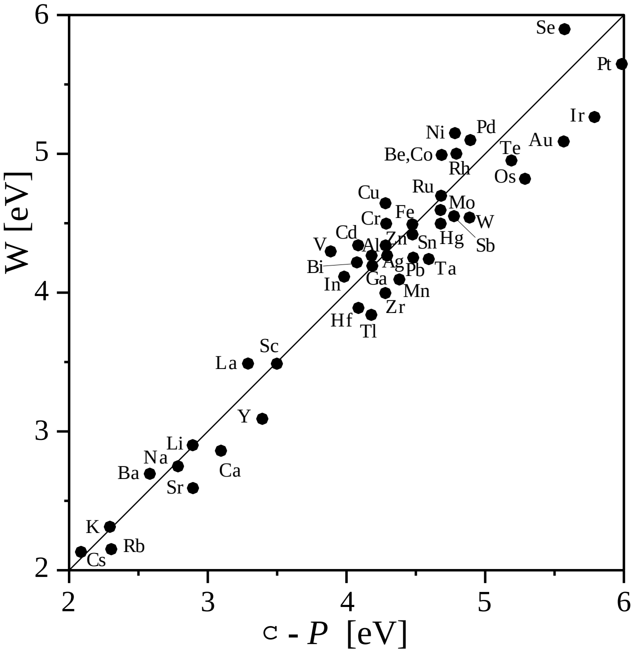

Figure 2.3: Correlation between the electronegativity χ, corrected by a periodicity parameter P specific to each column of the periodic table, and the work function W, for a large number of elemental metals. This figure is based on data from Reference [3].

table, and found a high correlation with the work function for a large number of elements (see Figure 2.3).

2.2 Local work function and image potential

Real metal surfaces often contain lateral inhomogeneities formed by chemical or structural defects, steps, and adsorbed atoms. At the surface of an alloy, a segregation of one element may also be observed. Since crystal surfaces are always of limited size, edge effects should be apparent near facet boundaries. These deviations from clean, homogeneous and infinitely-extended metal surfaces suggest introducing the concept of *local work function*, loosely defined as the energy required to take an electron from the Fermi level to a region just outside a locally homogeneous patch, or, more generally, to any specified point in the vacuum [17].

In this light, we seek to determine not only the electrostatic potential created far outside an infinitely-extended metal surface, but also to understand the potential experienced by an electron as it is gradually removed from the metal. Classical electrostatics provides some clues to the solution of this problem. An electron at a distance r outside a metallic surface classically generates a polarisation charge on the metal surface. The attractive potential created by this charge distribution can be represented by the effect of a mirror image, of charge $+e$, inside the metal, at a distance r from the surface (see Figure 2.4). By integrating the opposite of the force $-e^2/(2r)^2$ induced by the image on the external electron, when moving

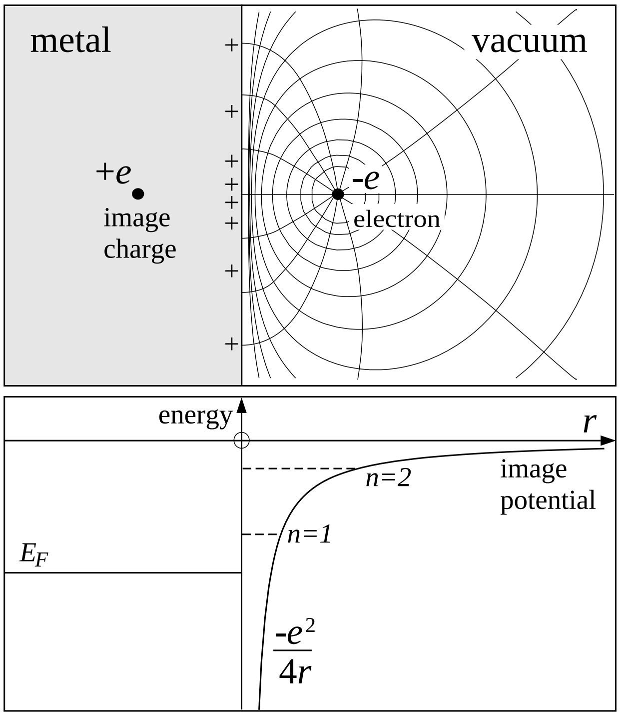

Figure 2.4: Classical image potential outside an ideal metal surface. Upper panel: potential contour lines and force gradients of the total potential created by the source electron and its image. The polarisation charge of the metal surface (+ symbols) is equivalent to the presence of a fictitious image of charge $+e$ inside the metal. Lower panel: Classical induced image potential felt by the external electron (solid line) and schematic quantum image states outside the metal surface (dashed lines).

the electron from infinity, and taking into account the simultaneous displacement of the two charges, the external electron is seen to experience an image potential V_{im} equal to:

$$V_{im}(r) = \int_{\infty}^{r} \frac{e^2}{(2r')^2} dr' = -\frac{e^2}{4r}. \tag{2.3}$$

Nonlocal quantum mechanic studies [9, 18] have shown that the long-range behaviour of the potential felt by an electron outside a metal surface is universally given by a shifted image potential $V_{im} = -e^2/4(r - r_o)$. Contrary to the classical case, the potential is referenced to an effective mirror plane r_o that is situated outside the geometric surface shown in Figure 2.1 and in general depends on the metal and the surface orientation [19]. The image potential describes the long-range behaviour of the so-called exchange-correlation potential in the vacuum (see Sections 3.2 and 3.3). The lateral shift of the image potential is induced by a significant exchange contribution close to the metal surface [18]. When the external probe electron is near the surface, the image concept breaks down and the exchange-correlation potential reaches a finite value in the metal, avoiding the unrealistic divergence of the classical image potential at the "surface plane".

The local work function of an electron in the vacuum is thus determined not only by the local electrostatic potential but also by the long-range image contribution, which vanishes only at infinity. As a consequence, in order to measure the real work function, it is necessary to extract the electron to a region where the image potential is negligible. In practice, beyond 100 nm, a large distance compared with the crystal unit cell dimension, the potential does not change significantly [20].

Conversely, local work functions, or variations of the local work function, near the surface can be measured by several local-probe techniques. For instance, changes in the local work function can be probed by photoemission spectroscopy of adsorbed xenon atoms (PAX). The PAX spectrum reflects the binding energies of the Xe orbitals. Because of the large size of the Xe atoms and their weak bonding to the metal, the energies of these levels depend on the local surface potential of the adsorption site. This technique has highlighted local work function variations near steps on Pt surfaces [17]. Alternatively, two-photon photoemission spectroscopy can identify the energies of the Rydberg series of image states trapped in the image potential above the Fermi level (see lower panel of Figure 2.4). In this technique, a photon first excites an electron from near the Fermi level into an image state just outside the metal surface. After absorbing a second photon and leaving the metal surface, the kinetic energy of the electron is measured. Combining the electron kinetic energy with the two photon energies enables the Fermi energy to be determined. If the image states are laterally confined to islands of adsorbed atoms, the local work function of the patch can be determined as a function of coverage [2]. Finally, as a further experimental alternative, scanning tunnelling microscopy can provide continuous maps of local work functions (see Section 2.4.7).

2.3 Anisotropy of the work function

Experimental measurements for a large number of metals have shown that the work function depends on the crystallographic orientation of the surface, a phenomenon known as the anisotropy of the work function. Although perhaps unexpected at first sight, the work function anisotropy can be understood as a surface effect. The work necessary to take an electron from inside the metal to a region outside it can depend on the surface orientation, since the potential difference between the metal and the vacuum is sensitively controlled by the spreading of the electronic charge into the vacuum. This spreading is in turn dependent on the crystallographic arrangement in the surface plane, *i.e.* on the surface orientation. However, sufficiently far from any finite neutral crystal, the electrostatic potential is constant and isotropic.

The presence of a work function anisotropy induces small electric fields in the vacuum around finite *neutral* crystals. These fields extend over distances

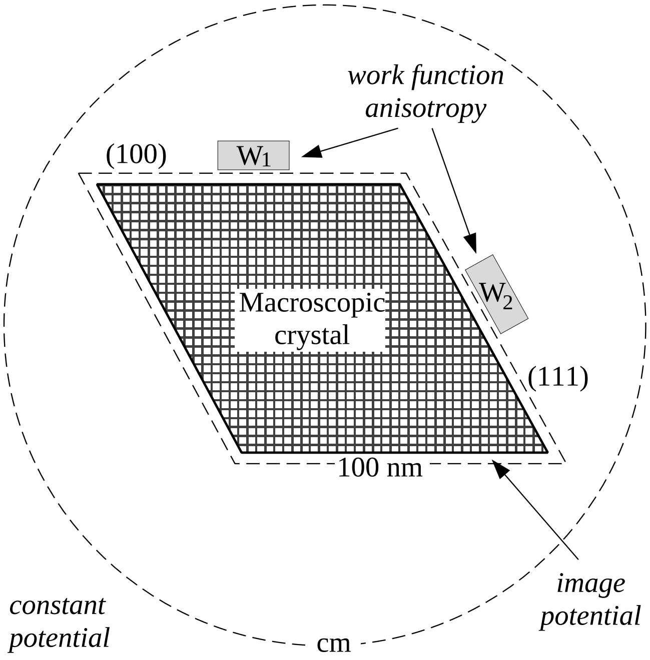

Figure 2.5: Schematic representation of a finite crystal with anisotropic facets in a perfect vacuum. The dominant contribution to the potential in the vacuum depends on the distance to the crystal and is shown in italics. Conceptually different regions (not to scale) are separated by dashed lines. The approximate regions where face-dependent work functions can be measured are shown as grey rectangles.

comparable to the dimensions of the crystal, as we now demonstrate. The Fermi energy E_F is constant inside the metal at thermodynamic equilibrium, and can be taken as a convenient reference. The potential in the neighbourhood of the crystal outside a facet of work function W_1 is then $V_1 = E_F + W_1$; while for a different facet of work function W_2, the potential is similarly given by $V_2 = E_F + W_2$. Therefore the potential difference ΔV between regions of the vacuum outside the two facets can be expressed as:

$$\Delta V = V_1 - V_2 = W_1 - W_2. \tag{2.4}$$

By conservation of energy, the work required to take an electron to any specified point in the vacuum must be independent of the surface from which it was extracted. This observation does not prevent a variation of the potential between different regions of the vacuum. The difference in potential between the two facet neighbourhoods is compensated by small electric fields in the vacuum, that ensure the continuity of the potential around the finite crystal. The fields outside the metal are induced by very small charge distributions on the crystalline facets [21]. These surface charges depend on the geometry of the metallic crystal, and, since the crystal is globally uncharged, sum to zero over the total surface. Since the vacuum does not reside at a constant potential in the neighbourhood of the crystal, a difficulty arises in defining precisely the extraction region for measuring the work function of a specific crystal facet.

Let us consider a neutral monocrystal with inequivalent facets exposed to a vacuum, in the absence of any external electric fields. In order to define the face-dependent work function precisely, the position of the electron, once removed from the metal, must be specified. For realistic crystals of finite dimensions, the local potential observed in the vacuum depends on the distance to the crystal and on the crystal shape. Several conceptually different regions can be distinguished around the monocrystal. Close to the metal surface, the local potential varies strongly due to the spilling of the electrons into the vacuum and the strong decrease of the image potential (see Figure 2.5). The characteristic extension of this region from the surface is 100 nm. Beyond this boundary layer, the local potential is essentially fixed by the work function anisotropy. Potential anisotropies are apparent provided the distance to the surface is comparable to the macroscopic crystal dimensions. The greyed areas W_1 and W_2 in Figure 2.5 show roughly adequate regions for measuring a work function anisotropy in a finite crystal.[3] The potential variation due to the work function anisotropy decreases as a multipole $[V(r) \sim (L/r)^n]$ as the distance r to the crystal increases above the typical crystal size L. The exact power exponent n depends on the macroscopic crystal geometry. Beyond a distance on the order of the crystal dimensions—say a centimeter—the local potential becomes isotropic and its variation is undetectably small.

Experimentally, work function anisotropies are often measured with detectors placed at distances from the surface that are well beyond the sample dimensions, contradicting at first sight the analysis presented above. Far from a small crystal, the work function anisotropy can nevertheless be observed by the application of an electric field collecting at the detector the electrons emitted from the metal. If each electron reaching the detector can be associated with a particular emitting facet, by observing the electron's trajectory, the work function of each facet can be inferred from its associated current. The current emitted from each facet is determined by the potential shape, and particularly by the maximum potential that the electrons must overcome. Even for small electric fields, this maximum is located close to the crystal surface and thus depends on the work function of the facet [14]. In this way, work function anisotropies have been identified experimentally (see Section 2.4). Furthermore, electric fields induced by work function anisotropies outside polycrystalline surfaces, and which are characterised by a range comparable to the dimensions of the crystallites, have been detected experimentally close to the samples. These fields have been identified as influencing the force-profile measured in some atomic force microscopy experiments as the tip-substrate distance exceeds 10 nm [22].

For a number of elements, the work function has only been measured in poly-

---

[3] Although we are interested here in a single monocrystal with inequivalent facets, an analogous potential distribution would be observed in the vacuum outside two metallic crystals in intimate contact. If the two metals had strongly different work functions, the effective work function anisotropy would be of several eV.

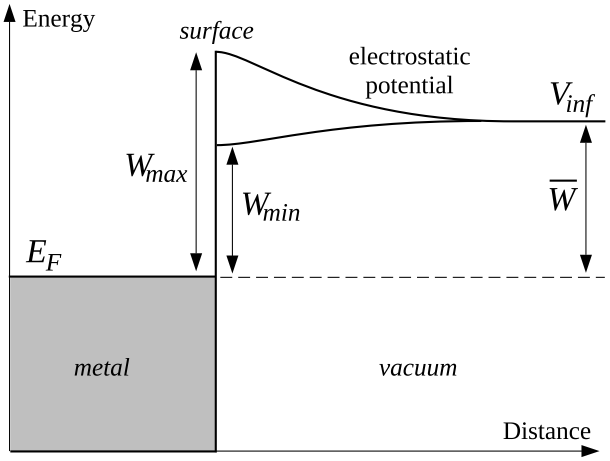

Figure 2.6: Radial dependence of the electrostatic potential in the vacuum outside a crystal with anisotropic facets or outside a polycrystalline sample. The potential is shown outside a facet with large work function (W_{max}) and small work function (W_{min}). The apparent work function in a perfect vacuum ($\overline{W}$) is the difference between the potential at infinity (V_{inf}) and the Fermi energy (E_F).

crystalline samples. These crystals generally consist of a large number of disordered crystallites with random orientations. The theoretical analysis of electron emission from polycrystals is difficult and depends on the particular emission process [23]. One usually tries to relate the *apparent work function* $\overline{W}$—equal to the difference between the Fermi energy and the potential at infinity—with the work functions of the individual crystallites, known as "patches", observed at the crystal surface. In Figure 2.6, the electrostatic potential is plotted as a function of the distance to the crystal surface outside regions of high and low work function. Far from the sample, the anisotropy is lost, and, in the absence of external electric fields, the electrostatic potential reaches a constant value. This apparent work function is intermediate between the maximum and minimum work functions of the polycrystalline surface. In this respect, the situation is the same as for a single crystal with anisotropic facets exposed to the vacuum.

The apparent work function $\overline{W}$ can usually only be determined from the detailed arrangement of all the crystallites. However, some general results are known in appropriate geometries. In the case of planar, cylindrical, or spherical polycrystalline surfaces, the apparent work function $\overline{W}$ is known to be equal to the surface-area weighted average of the individual work functions W_j [23]. If f_j is the fractional surface area associated with work function W_j, then:

$$\overline{W} = \sum_j f_j \, W_j. \tag{2.5}$$

A more accurate definition of the weights f_j has been given by Sahni and coworkers for arbitrary patch distributions in the special case of uniform surface charge densities, by accounting for the long-range electrostatic interactions between the

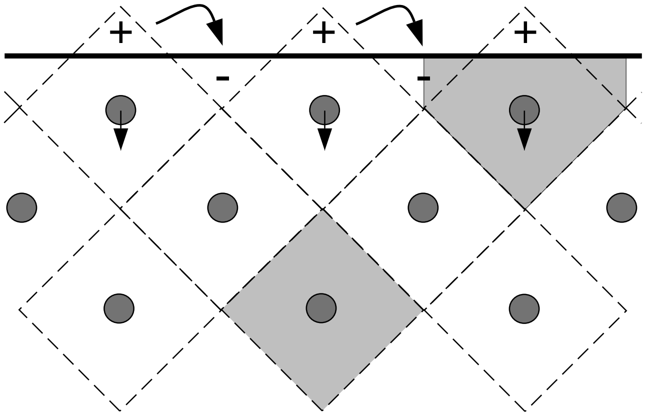

Figure 2.7: The principle of Smoluchowski smoothing, illustrated for a two-dimensional simple cubic lattice. At the metallic surface, the electronic density is rearranged from a superposition of Wigner-Seitz units cells (dashed lines) into a smoother distribution (thick solid line). The charge redistribution (greyed areas) sets up an orientation-dependent surface dipole, and leads to inward relaxation of the surface ions (arrows).

patches [24]. At a polycrystalline surface, the exposed facets usually consist of low-index orientations, which have a lower surface energy than high-index planes. The patch work functions W_j contributing dominantly to the apparent work function should accordingly correspond to the most densely-packed orientations.

2.3.1 Smoluchowski smoothing

E. Wigner
1902–1995

In 1941, Smoluchowski proposed a theoretical model [5] that describes qualitatively the observed work function anisotropy in a number of elemental metals, such as Ni, Cu, Ag and W. There are however some exceptions, notably Al, for which this model fails to predict the observed anisotropy. In the Smoluchowski model, the real metal surface is imagined to be formed in two steps.

The metallic surface is assumed to be created first by superposing Wigner-Seitz unit cells containing the bulk electronic density. This initial electronic surface distribution does not lead to any work function anisotropy since the crystal is formed by repeating a neutral charge-density building block with no dipole or quadrupole [25]. To recover the real surface, one must in general rearrange the electron density so as to minimise the total energy. This redistribution is decomposed into two orthogonal displacements.

At the surface, in the absence of the next ionic layer, the electrons are less bound to the metal. The charge density spreads into the vacuum in a direction perpendicular to the surface, inducing a large surface dipole. The spreading of the electronic charge into the vacuum is related to the radial charge distribution in an isolated atom, and is thus assumed to produce an orientation-independent work function enhancement. As well as a rearrangement normal to the surface, the electronic fluid undergoes a lateral redistribution within each surface unit cell. The electrons tend to move from the edges of the Wigner-Seitz unit cells into the valleys, leading to a smoother electronic distribution and a lower total kinetic energy. The reduction in kinetic energy can be simply understood in the case of non-interacting electrons [26]. The local kinetic energy per particle $t_s(r)$ in a non-uniform gas of local density $n(r)$ is given to second order in the density variations by:

$$t_s(n(r)) = \frac{\hbar^2}{2m}\left[\frac{3}{5}(3\pi^2 n)^{2/3} + \frac{1}{36}\frac{|\nabla n|^2}{n^2}\right]. \tag{2.6}$$

$\hbar$ is the Planck constant and m is the electron mass. The first term is the kinetic energy per particle of a uniform electron gas (jellium). The second term is the leading correction to account for the gas inhomogeneity [27] and is minimised by smoothing the electronic fluid to reduce its gradient.[4] The final amount of smoothing results from the interplay of these kinetic effects with the potential contributions to the total energy.

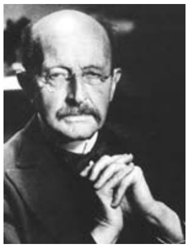

M. Planck
1858–1947

The smoothing procedure is illustrated in Figure 2.7 for a two-dimensional simple cubic lattice. At the surface, if we temporarily neglect the perpendicular spreading, the electronic distribution is more closely described by the thick solid line, corresponding to perfect smoothing, than by the dashed lines that follow the Wigner-Seitz unit cells. The lateral rearrangement of the electrons creates a second supplementary dipole (shown by +/- symbols), oppositely-oriented to the one created by the spreading and thus reducing the work function. For a uniform electronic density and assuming perfect smoothing, this reverse dipole depends on the surface orientation by way of the packing density. Surface orientations of high density experience small smoothing, inducing a small reverse dipole, and thus a high work function. In the Smoluchowski model, the work function is expected to rise with increasing atomic packing in the surface plane. In Figure 2.8, to illustrate the differences in surface atomic arrangement, Wigner-Seitz units cells are superposed to form the three most dense surface orientations of a face-centered cubic metal. The (111) surface is the most dense, followed by the (100) and the (110).

---

[4] In his original article, to account for the gas inhomogeneity, Smoluchowski used the von Weizsäcker correction [28], which gives a correction of the same form as that of Equation 2.6 but is too large by a factor of 9. It was derived by assuming an electronic density produced by a single wave function: $n = |\Psi|^2$. The quantum kinetic energy per particle is $t_s \sim \int dr\ |\nabla\Psi|^2/n$. Since $|\Psi| = \sqrt{n}$, we have $t_s \sim \int dr\ 1/4\ |\nabla n|^2/n^2$.

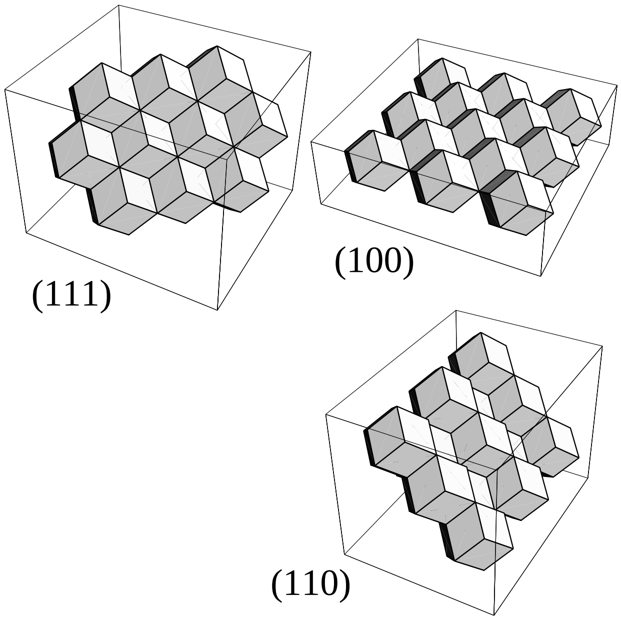

Figure 2.8: The three most dense surface orientations of a face-centered cubic metal: superposition of Wigner-Seitz unit cells. The atomic packing in the surface plane decreases from (111) to (100) and to (110).

Table 2.1: A list of the atomic planes of highest density (hkl), ordered by decreasing density, in face-centered cubic (FCC), body-centered cubic (BCC) and simple cubic (SC) crystals. The spacing d_{hkl} between the atomic planes is shown in multiples of the lattice constant.

FCC		BCC		SC	
(hkl)	d_{hkl}	(hkl)	d_{hkl}	(hkl)	d_{hkl}
(111)	0.577	(110)	0.707	(100)	1.000
(100)	0.500	(100)	0.500	(110)	0.707
(110)	0.354	(211)	0.408	(111)	0.577
(311)	0.301	(310)	0.316	(210)	0.447
(331)	0.229	(111)	0.288	(211)	0.408
(210)	0.224	(321)	0.267	(221)	0.333

A. Bravais
1811–1863

The packing density argument used in Smoluchowski smoothing applies best to the low-index surface orientations. These are detailed in Table 2.1, for the Bravais lattices of cubic symmetry. The largest interplane spacings d_{hkl} correspond to the most densely-packed surfaces. The work functions of cubic metals are thus expected to decrease in the order indicated in this table.

Surface orientations with higher indexes are better described as regularly-stepped low-index planes of similar orientation. On high-index surfaces, the work function is often seen to decrease with increasing step density. This can be understood by an extension of Smoluchowski's smoothing argument to the case of an abrupt step edge. The self-consistent electronic density tends to smooth the abrupt step into a more gentle oscillation. The electronic rearrangement from the top of the step to the lower

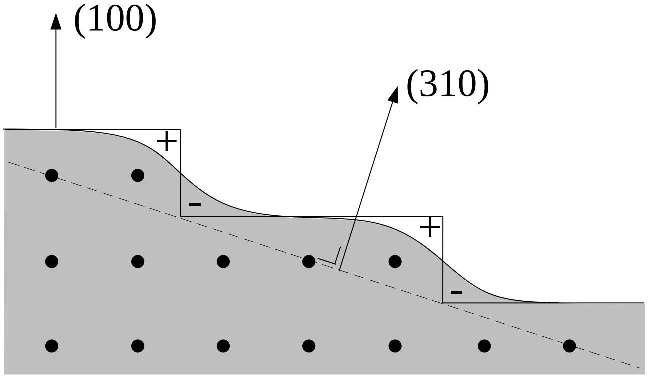

Figure 2.9: Smoluchowski smoothing on a high-index stepped surface: the (310) surface can be seen as a (100) surface with regularly spaced steps. By way of the smoothed electronic surface (shaded area), the steps create additional reverse dipoles (+/-) that may lower the work function.

corner forms a supplementary reverse dipole that decreases the work function, as shown in Figure 2.9 for a simple cubic lattice. This charge redistribution at the surface leads to a dipole associated with each step. If the steps do not interact significantly, the work function should decrease linearly as the step density rises, as has been observed both experimentally, for noble and transition metals [29, 30], and theoretically for jellium surfaces [31]. However, some exceptions have been noticed in first-principles calculations of steps on Al(111) [32].

It was later pointed out by Finnis and Heine that in simple *sp*-metals Smoluchowski smoothing leads to an inward relaxation of the surface layer of ions [33]. Returning to Figure 2.7, we notice that after full smoothing the electronic density associated with a surface ion is contracted towards the metal with respect to that of a bulk ion (greyed areas). By evaluating the electrostatic equilibrium point inside a uniformly charged cell, which approximately describes the location of the relaxed ion, Finnis and Heine showed that the top layers of metal surfaces should relax inwards. Furthermore, the relaxation depends on the surface orientation, with low-density surfaces relaxing inwards more strongly. For face-centered cubic metals, in the (111), (100) and (110) orientations, and assuming perfect smoothing, the expected contractions are respectively -1.6%, -4.6% and -16% of the corresponding bulk interplanar spacings. This argument however neglects the orientation-independent free-atom-like electron spilling into the vacuum.

2.3.2 Perturbational treatments

In order to account for the work-function anisotropies, Lang and Kohn proposed a linear perturbational treatment describing the corrections due to a weak ion lattice potential to their calculation of jellium surfaces [4]. In this model, a uniform-background calculation is first performed at the electronic density of the metal of interest, which yields a work function W_u. The discrete-lattice potential is then

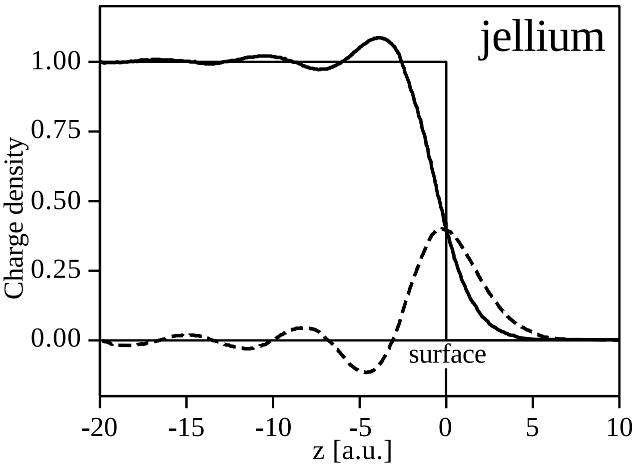

Figure 2.10: Electronic charge density $n(z)$ at a jellium surface, in multiples of the bulk density (solid line), and surface charge $n_\sigma(z)$ induced by a weak external electric field normal to the surface, in arbitrary units (dashed line), as calculated by Lang and Kohn [4]. The bulk density corresponds to $r_s = 4$. The positive background is shown as a step function.

included as a weak one-dimensional perturbation $\delta v(z)$ to the jellium surface. The perturbation $\delta v(z)$ is taken as a planar average of the potential generated by replacing the positive-background model by a sum of local pseudopotentials. The work function W of the metal surface is shown to be exactly written to first order in the perturbation as:

$$W = W_u + \delta W \tag{2.7}$$

$$\delta W = \int \delta v(z)\, n_\sigma(z)\, dz \tag{2.8}$$

The charge density $n_\sigma(z)$ is the change in electronic density at the surface of the jellium following the removal of an electron. Since only linear corrections are included, it may be calculated from the normalised surface charge induced by an arbitrary weak electric field applied normally to the jellium surface (see Figure 2.10). The centre of mass of $n_\sigma(z)$ is then also shown to yield the location of the effective image plane for the jellium surface [34].

The resulting theoretical work-function anisotropy is typically on the order of 10% of the total work function and is expected to describe simple metals effectively. Within this approach, the work function anisotropy normally increases with the atomic packing in the surface plane, in accordance with the Smoluchowski rule. Further extensions accounting for higher-order effects [35, 36] generally confirm this theoretical surface ordering.

2.4 Experimental data and techniques

Ultrahigh vacuum (UHV) and epitaxial growth techniques, such as molecular beam epitaxy, have recently allowed unprecedented control of the quality of crystal surfaces, so that it is now possible to determine the dependence of the work

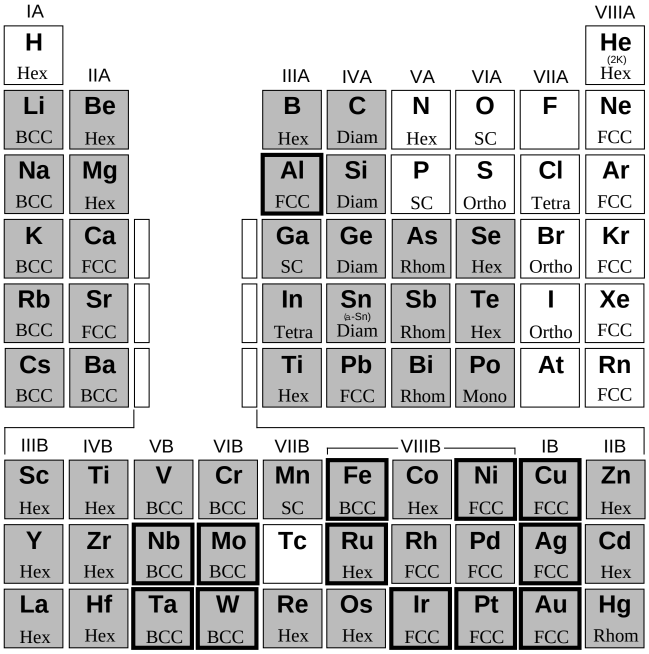

Figure 2.11: Periodic table of the elements. The greyed squares indicate elements with measured work functions. The bold borders show where the work function anisotropy has been determined experimentally. The low temperature crystalline systems are abbreviated according to: FCC: face-centered cubic, BCC: body-centered cubic, SC: simple cubic, Diam: diamond structure, Hex: hexagonal, Tetra: tetragonal, Ortho: orthorhombic, Rhom: rhombohedral, Mono: monoclinic.

function on the surface crystallographic orientation with a high degree of accuracy. Work functions are very sensitive to the cleanliness of the crystal surface, so avoiding adsorbed atoms and molecules remains essential for obtaining reproducible work functions [14]. Technical improvements now allow atomically-clean surfaces to be produced and preserved from contamination. Metal surfaces may be cleaned by repeated cycles of inert-gas ion bombardment, followed by thermal annealing to repair the surface damage. Auger Electron Spectroscopy is often used to monitor the surface cleanliness and chemically identify the possible adsorbed atoms [20]. UHV conditions in the 10^{-10}–10^{-11} Torr range are required to prevent gas molecules from sticking to the sample surface in large numbers. If we assume all the incident gas atoms attach to the surface, these pressure conditions limit the contamination to a fraction of a monolayer on the experimental time-scale of one hour [20].

The techniques for determining work functions can be broadly classified into two groups. The first family of experiments aims at measuring the work function on an absolute scale and is based on electron emission processes. By stimulating a metallic surface in various ways, a current of electrons is produced, from which the work function is determined. The stimulus can consist of photons (as in the photoelectric effect and in ultraviolet photoelectron spectroscopy), be of a thermal nature (thermionic emission), consist of an applied electric field (field emission), or be a combination of these methods.

The second class of techniques concentrates on obtaining work function dif-

Table 2.2: Experimental work functions, in eV, of selected clean metallic surfaces, for various surface orientations (from Reference [39]). The second column gives the atomic structure. The last column indicates the experimental technique: A: angle-resolved photoelectron spectroscopy, P: photoelectric, F: field emission, D: diode method.

Metal	Struc.	W (111)	 (100)	 (110)	Exp. Tech.
Al	FCC	4.24	4.42	4.28	P
Ag	FCC	4.56	4.42	4.35	A
Au	FCC	5.26	5.22	5.20	A
Cu	FCC	4.94	4.59	4.48	P
Ir	FCC	5.76	5.67	5.42	F
Ni	FCC	5.25	4.95	4.55	A/D
W	BCC	4.47	4.63	5.25	F
Cs	BCC	2.3 (polycrystal)			A
Na	BCC	2.4 (polycrystal)			P

ferences, either between various metals or during surface modifications such as adsorption processes. Contact potential differences, diode methods and scanning tunnelling microscopy fall into this category.

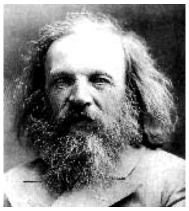

D. Mendeleev
1834–1907

The work functions of clean surfaces have now been measured for most metallic elements, as illustrated in the Mendeleev periodic table of Figure 2.11. The work function anisotropy is known only for some of the more common cubic elements. Work function compilations for a large number of metals and orientations have been published in [1, 2, 37–39]. Some selected tabulated values are shown in Table 2.2. The work function anisotropies of all the elements shown here, aluminium excepted, follow the Smoluchowski rule.

In the following paragraphs, we briefly present the various approaches for measuring work functions with their respective strengths, accuracies, and applications. In each case, developed theoretical models of the dynamics of electron emission are necessary to insure that the measured parameters reflect the sought-after values. We detail some of the models used for interpreting work function measurements.

2.4.1 Photoelectric effect

If a metallic surface is illuminated with sufficiently energetic photons, the electrons near the Fermi energy may acquire enough energy to overcome the surface barrier and leave the metal, a process known as the photoelectric effect. A number of theoretical models have been proposed to calculate the resulting current [40]. Assuming a free electron band structure and electrons emitted close to the surface, Fowler calculated the current using a simple one-dimensional model [41]. He used

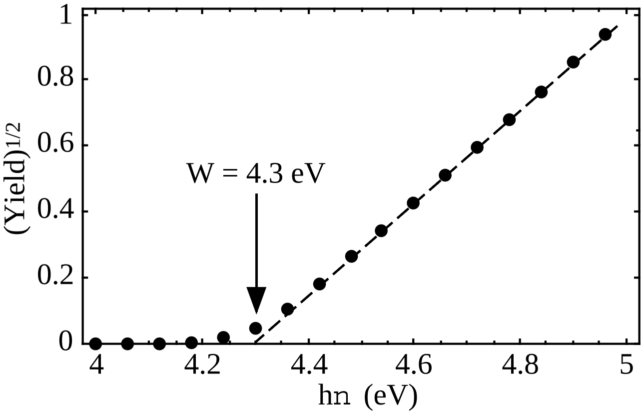

Figure 2.12: Simulation of a photoelectric current measurement using the Fowler relation (see Eq. 2.10): the square root of the yield (in arbitrary units) is plotted (circles) as a function of the energy of the incident photons. Linear extrapolation to zero (dashed line) gives the work function W. This simulated graph was drawn for room temperature conditions with $W = 4.3$ eV.

Einstein's condition for the photoelectric process:

$$E_{out}^{kin} = E_{in}^{kin} + h\nu - \Delta V, \tag{2.9}$$

where $E_{in/out}^{kin}$ is the kinetic energy of the electron inside/outside the metal, $h\nu$ is the energy of the absorbed photon, and ΔV is the total potential step at the surface. To derive the photoelectron energy spectrum, he assumed that the only electrons emitted possessed originally, in the metal, a kinetic energy normal to the surface $E_{\perp}^{kin}$, augmented by the photon energy $h\nu$, sufficient to overcome the surface barrier. For photons of fixed frequency $h\nu$, at a sample temperature T, the saturation current J is then given by:

$$J(h\nu) = B(k_BT)^2 f((h\nu - W)/k_BT). \tag{2.10}$$

A. Einstein
1879–1955

B is a material-dependent value related to the probability of absorbing a photon, which is assumed constant near the emission threshold. $f(x)$ is a universal function given by:

$$\begin{aligned} f(x) &= \frac{\pi^2}{6} + \frac{x^2}{2} + \sum_{n=1}^{\infty} (-1)^n \frac{e^{-nx}}{n^2} \quad \text{if } x \geq 0 && (2.11) \\ &= -\sum_{n=1}^{\infty} (-1)^n \frac{e^{nx}}{n^2} \quad \text{if } x < 0. && (2.12) \end{aligned}$$

Experimentally, the metallic surface is illuminated with a monochromatic wave of adjustable frequency. For large values of $x = (h\nu - W)/k_BT$, $f(x)$ is quadratic in x. If the square root of the current is reported as a function of $h\nu$, the linear

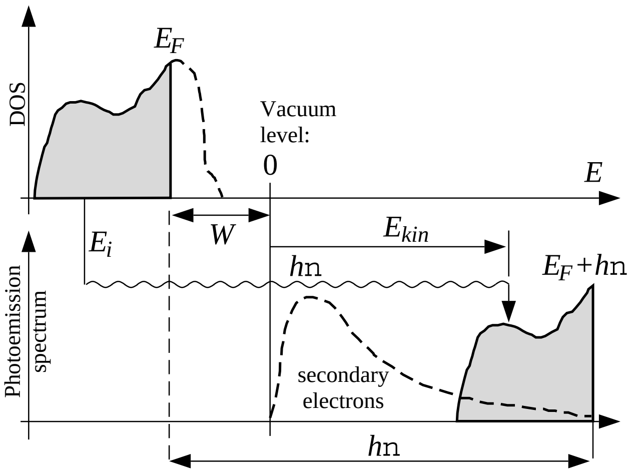

Figure 2.13: Schematic description of the photoemission process. An incident photon with energy $h\nu$ excites a valence electron of energy E_i into the vacuum. Inelastic effects give rise to the emission of secondary electrons. The full width of the spectrum is $h\nu - W$, enabling the work function to be determined.

relation can be extrapolated to zero to determine the work function W, as shown in Figure 2.12. This zero-temperature approximation is the procedure commonly adopted to interpret experimental data [42]. Corrections may be included to account for the collecting electric field, which lowers the surface barrier slightly [43]. The resulting accuracy on the work function is ±30 meV, which has proved sufficient to highlight a work function anisotropy in Al [42], Ag, Cu, and Mo [39].

2.4.2 ARUPS

In Angle-Resolved Ultraviolet Photoelectron Spectroscopy (ARUPS), monochromatic ultraviolet light of known frequency ν excites electrons in the valence band, of energy E_i (with respect to the vacuum), into excited states above the vacuum energy. The electrons are then emitted from the crystal into the vacuum [44]. In this modern variation of the photoelectric effect, the electrons are detected as a function of their angle of emission, and their kinetic energy is analysed. The spectrum recorded consists of primary electrons (the shaded area in Figure 2.13) with kinetic energy $E_{kin} = E_i + h\nu$, as well as secondary electrons of lower kinetic energy. The secondary electrons result from inelastic scattering of the primary electrons during the emission process, and have kinetic energies down to zero. The total width of the spectrum of the emitted electrons is seen to be equal to $h\nu - W$, thus providing a measure of the work function W. The angle-resolved mode insures that the spectrum thresholds are clearly defined so that the spectrum width can be evaluated accurately [39]. A small bias voltage collects the electrons emitted, but leaves the spectrum width unchanged, providing an accuracy of ±10 meV on W. The work function anisotropies of Ag, Au, Cu, and Ni [2, 39] have been measured in this way.

2.4.3 Thermionic emission

On heating a metallic surface to a high temperature T, in the 1000–1500 K range, a fraction of the electrons acquire sufficient energy to leave the metal. Using thermodynamic theory, one can show that the saturation current density J can be approximated by the Richardson-Dushman formula [23]:

$$J(T) = A(1-r)T^2 \exp(-W/k_B T), \tag{2.13}$$

where $A = emk_B^2/2\pi^2\hbar^3$ is a universal constant and r is the mean reflection probability for electrons incident on the metal surface in the equilibrium state. The determination of W from measurements of the current J, as a function of the temperature T, is complicated by various factors. A collecting field E is applied to measure J, which lowers the work function slightly and induces a supplementary parameter, which needs to be extrapolated to zero. The variation of W (and of r) with T must be taken into account, leading to an accuracy of 0.1 eV on the measured work function. The temperature dependence of work functions is usually around $\pm 10^{-3}$–10^{-4} eV/K [14].

In the case of a patchy polycrystalline surface, if the collecting field E is sufficiently small, the apparent work function is thought to be slightly above the average value of the individual local work functions, weighted by their respective patch areas. If the collecting field is much larger than the patch field, the apparent work function is biased towards the lowest work functions [37].

Modern developments include projecting the electrons emitted from a metallic microtip onto a phosphor screen, so creating a thermionic projection microscope, which has allowed several single-plane work functions of Nb [45], W [46], and LaB_6 [47] to be imaged, and sometimes measured, simultaneously. In view of the stability of these last two materials at high temperatures, they are commonly used as thermionic filaments in electron microscope sources.

2.4.4 Field emission

In a field emission experiment, a sharp metallic tip is subject to a large electric field (on the order of one V/nm) that lowers the electrostatic surface barrier. This reduction is known as the Schottky effect. The electrons in the metal can then tunnel out into the vacuum, giving rise to a current density that depends on the work function W and on the electric field E. Assuming a triangular surface barrier in the presence of a uniform electric field, the current J is described in free electron theory, at zero temperature, by the Fowler-Nordheim equation:

$$J(E) = \frac{e^3E^2}{8\pi hWt(y)^2} \exp\left(\frac{-4(2m)^{1/2}W^{3/2}\delta(y)}{3eE}\right), \tag{2.14}$$

$t(y)$ and $\delta(y)$ are slowly-varying functions of $y = \sqrt{e^3 E}/W$, on the order of unity. They account for the deformation of the barrier induced by the image force [14]. Broadly speaking, the work function is determined experimentally by measuring the slope of $\ln(J/U^2)$ versus $1/U$, where U is the accelerating potential, assumed proportional to E.

The emitted electrons follow the electric field lines that diverge from the metallic tip, forming an increasingly magnified view of the tip. Since the crystal tip is composed of many different facets, the individual work functions of the various surface orientations can be imaged by using a probe hole to select electrons emitted from a particular area [48]. The resolution of 20–30 Å is limited mainly by the transverse momentum of the electrons and by diffraction effects [39]. This technique has been applied to Rh multi-faceted tips of 1500 Å radius [49], as well as to Pt and W [39] single surfaces, with an accuracy of ±60 meV on the work function.

On the basis of similar experiments, W(111) and W(130) were chosen as the emitting facets for the sources of several electron optics instruments. Practical applications of coupled thermionic and field emission are found in the electron sources of oscilloscopes, televisions and terminal displays. The electrodes often consist of a high melting-point metal coated with a thin low-work-function material to increase the source brightness. Fluorescent tubes and high-intensity arc-discharge lamp bulbs, used for projection displays and floodlighting, contain similar electrodes [50].

2.4.5 Contact potential difference

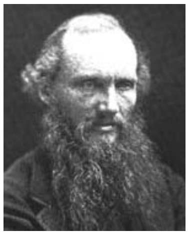

Lord Kelvin
1824–1907

The Contact Potential Difference (CPD) method provides a measure of the work function of a sample relative to that of a reference metal [44]. It was first proposed by Lord Kelvin in 1898, and is also known as the Kelvin probe technique. The set-up consists of a capacitor formed by two parallel plates of different metals, one of which is the sample of interest. The plates are separated by a vacuum layer of width d and are connected via an external ammeter I (see Figure 2.14). If no external tension is imposed, and in view of the different work functions W_1 and W_2 of the two metals, a current flows until the two Fermi levels E_{F_1} and E_{F_2} coincide, thus creating in the condenser a surface charge Q and a contact potential difference $\Delta V = W_2 - W_1$. If the probe is vibrated back and forth, the condenser capacitance changes. Since the potential difference ΔV is constant, an oscillatory current flows through the circuit, and is detected by the ammeter I. Experimentally, a supplementary external potential V_{ext} is often imposed in the circuit in order to compensate for ΔV. When the

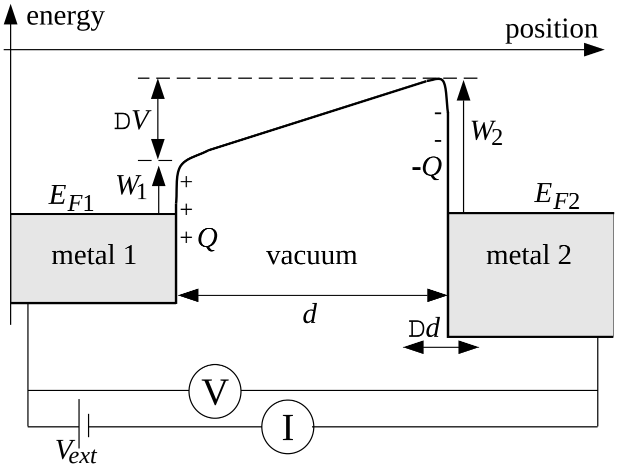

Figure 2.14: Measurement of the relative work function of two metals by the contact potential difference technique. The two plates of a capacitor consist of different metals and are connected by an external circuit through an ammeter I. The two plates are separated by a vacuum region of width d, the probe metal vibrating back and forth by Δd, so generating a varying current in the circuit.

current vanishes, $V_{ext} = -\Delta V = W_1 - W_2$, allowing the work function difference to be read on a voltmeter V. For patchy surfaces, CPD techniques measure the potential difference between the patch-averaged values of the work functions of the two electrodes [37].

This technique is well adapted for measuring work function changes, and can, in principle, attain an accuracy on the order of 1 meV. It has been widely employed to study alkali and oxygen adsorption on various metals [14]. Maps of work function differences, with a lateral resolution below 50 nm, have also been obtained using a scanning CPD apparatus [51].

2.4.6 Diode methods

An alternative method for measuring work function differences and variations was suggested by Anderson [52]. Here, a slow beam of electrons is thermally emitted from a cathode source and is accelerated by an electric field onto the sample of interest that constitutes the anode. The beam size is chosen large on the atomic scale but small compared with the crystal surface. The resulting current I is measured as a function of the applied potential difference V. If the work function of the sample changes, the I-V characteristic of the diode shifts horizontally accordingly. Usually, a feed-back mechanism fixes the current, which allows the work function change to be directly read out from the difference in applied potential. An accuracy of 5 meV can be obtained in this way. If the beam is produced by an electron gun and retarded near the sample, the beam can be scanned across the substrate, allowing work function maps to be produced [53].

This technique has been widely applied for in-situ studies of gas adsorption on metallic substrates. Recently, it has been used to track quantum size effects on

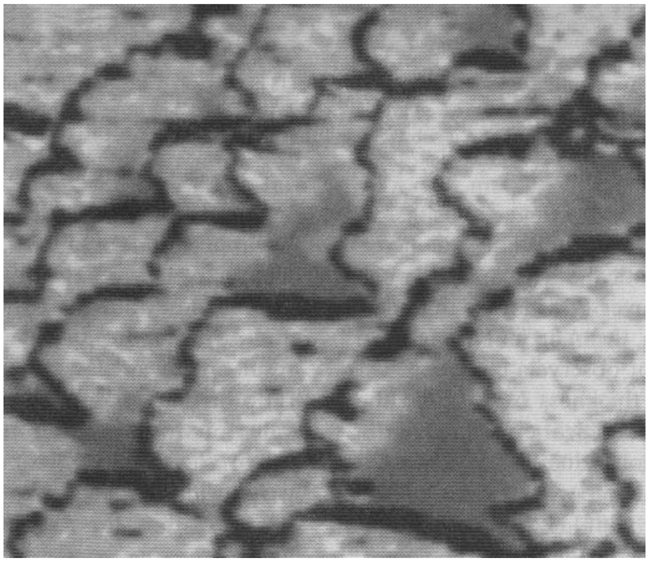

Figure 2.15: Work function image of a Cu(111) surface with a 0.9-monolayer Au coverage, acquired by scanning tunnelling microscopy [55]. The width of the photo is approximately 50 nm. The Au is deposited at the lower side of the step edges, forming (111)-oriented planes. Bright areas correspond to higher work functions, showing a larger work function for Au and a reduced work function near the step edges.

the work functions of indium films deposited on gold substrates [54]. The work function change can be directly measured during the adsorption process, allowing the work function to be obtained as a function of the film thickness.

2.4.7 Scanning tunnelling microscopy

A novel technique for obtaining microscopic images of local work functions is based on scanning tunnelling microscopy. When a sharp tip is brought sufficiently close to a metallic surface, the electron wave functions of the tip and those of sample overlap, and electronic transport is permitted via quantum tunnelling. A measurable current flows through the tip when a bias voltage is applied, from which variations of the tip-sample distance as small as a hundredth of an Ångström can be inferred.

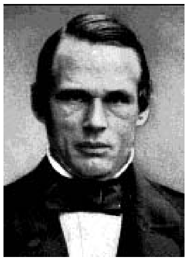

A. J. Ångström
1814–1874

As the tip scans the surface, in conjunction with a topographic picture, a work function image can be obtained by measuring the response in the tunnelling current as the tip-substrate distance is oscillated lightly [56, 55]. An example of such an image is shown in Figure 2.15, for Au deposited on a Cu substrate. Although chemical contrasts between different elements are readily achieved, the interpretation of the images in terms of a real work function is difficult [57]. Since the separation of the tip and sample is only a few Ångströms, and in view of the bias voltage of several Volts, the work function does not appear as an isolated quantity in the signal received. Models and simulations are required in order to account for the influence of the probe itself on the local surface potential and to interpret the tunnelling current in terms of work functions or work function differences [58–60]. The contrast observed is therefore usually described in terms of an "apparent barrier height" rather than a local work function [21]. In a one-dimensional tunnelling model, the apparent barrier height ϕ_{ap} is given by:

$$\phi_{ap} = \left[\frac{\hbar}{2\sqrt{2m}} \frac{d(\ln G)}{dz} \right]^2 , \tag{2.15}$$

where G is the conductance and z the tip-sample distance [58]. The real work function is then estimated from the average apparent barrier height of a large number of measurements—to account for shape effects in the tip—by empirically correcting for the bias voltage. This leads at best to an accuracy of 300 meV on the work function.

There once was a keen Aberdonian
Who burnt himself frying an onion,
His mom said ‘‘Oh, my,
I don’t wish to pry,
But I think you’ve the wrong Hamiltonian’’

Victor Lesk

Chapter 3

Methodology

3.1 Ab initio calculations

THE objective of *ab initio* calculations is to predict the physical properties of material systems using no empirical or experimental input. On the basis of the sole knowledge of the constituent atoms, by way of their atomic numbers only, all physical characteristics should be determined quantum-mechanically without uncontrolled simplifications or approximations. In particular, the atomic structure must first be obtained, from which all electronic, vibrational, magnetic, and optical properties should be extracted.

Density functional theory provides the theoretical background for such ambitious studies by demonstrating formally how all features of many-electron systems encountered in atoms, molecules, and solids, can be deduced from the ground-state electronic density only [26]. Even in the simplest cases, to obtain the electronic density from first-principles Hamiltonians is a formidable task that cannot be accomplished analytically and necessitates large-scale calculations on dedicated computers.

Nowadays, with the continuous increase in available computational power and refined theoretical techniques, *ab initio* solid state computations have progressed beyond structural studies of bulk materials to include surface phenomena, defects, clusters, disordered systems, as well as to study adsorption, catalysis, chemical reactions and molecular dynamics [61], in a wide range of materials. These studies are performed as a complement to experimental findings and have often helped our physical understanding of new materials and lead to further insights and predictions.

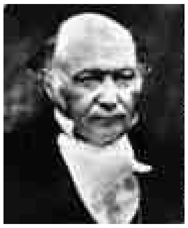
W. R. Hamilton
1805–1865

First-principles studies of metal surfaces, based on density-functional theory, represent to date the most accurate method of calculating work functions. Some authors recently contended that *ab initio* work functions are at least as accurate as present-day experimental values [62]. *Ab initio* computations give access to the full three-dimensional charge density at the metal surface and allow all the electronic states to be calculated self-consistently. Surface ionic relaxations and reconstructions can also be incorporated into this framework.

In the following sections, we present some general physical ingredients necessary for density functional *ab initio* calculations. We present a brief introduction to the local density approximation used for modelling electron-electron interactions, and to pseudopotentials for describing the electron-ion interactions. Methods for dealing with extended periodic systems, containing an infinite number of particles in a repeated geometry, are also described, as well as the specificities necessary for metallic crystals.

3.2 Density functional theory

The objective of Density Functional Theory (DFT) is to determine exactly the ground-state properties of an interacting many-electron system in an external potential using the electronic density $n(\mathbf{r})$ as the basic variable. There are a number of good reviews and books on Density Functional Theory (see for example [63–66]). We give here only a very short presentation, introducing the basic concepts that will be of interest later on.

The starting point in this approach of condensed matter theory is the stationary Schrödinger equation for a N-electron system in a given external potential $v_{ext}(\mathbf{r})$, which we seek to solve in all generality:

$$\left[-\frac{\hbar^2}{2m}\sum_{i=1}^{N}\nabla_i^2+\sum_{i=1}^{N}v_{ext}(\mathbf{r}_i)+\frac{1}{2}\sum_{i\neq j}\frac{e^2}{|\mathbf{r}_i-\mathbf{r}_j|}\right]\Psi(\mathbf{r}_1,...,\mathbf{r}_N)=E\Psi(\mathbf{r}_1,...,\mathbf{r}_N). \tag{3.1}$$

$\Psi(\mathbf{r}_1,...,\mathbf{r}_N)$ is the many-body wave function, E the total energy, and the other symbols have their usual meanings. The first term in Equation 3.1 gives the electronic kinetic energy, the second the effect of the external potential and the third the electron-electron interaction. We neglect spin effects [67] in our calculations as we are dealing with non-magnetic metals. In condensed matter systems, the huge number of particles, on the order of the Avogadro number, obviously renders the direct resolution of Equation 3.1 impossible. However, from an experimental point of view, we are not interested in the full many-body wave function, but only in contracted quantities such as the electronic density.

A rigorous theorem by Hohenberg and Kohn [11], which is at the basis of DFT, shows that the knowledge of the ground-state electronic density $n(\mathbf{r})$ is sufficient to determine all the physical properties of the system. In particular, the ground-state electronic density is proven to determine the external potential $v_{ext}(\mathbf{r})$, to within an additive constant, as well as the total number of particles N. The full Hamiltonian and all properties derived from it are thus uniquely determined by $n(\mathbf{r})$. Furthermore, a variational principle shows that there exists an energy functional of the charge density $E[\hat{n}] = \int v_{ext}(\mathbf{r})\hat{n}(\mathbf{r})\mathbf{dr} + F[\hat{n}]$, which attains its minimum if and only if the charge density $\hat{n}(\mathbf{r})$ is the exact ground-state density $n(\mathbf{r})$. $F[\hat{n}]$ is a universal functional, independent of the external potential. In principle, therefore, all the interesting properties of the system can be obtained by minimising this functional.

There are unfortunately no general guidelines for determining the functional $F[n]$. Kohn and Sham [12] proposed decomposing the functional according to:

$$F[n] = T_s[n(\mathbf{r})] + \frac{e^2}{2}\int \mathbf{dr}\,\mathbf{dr}'\,\frac{n(\mathbf{r})n(\mathbf{r}')}{|\mathbf{r}-\mathbf{r}'|} + E_{xc}[n(\mathbf{r})], \tag{3.2}$$

where $T_s[n(\mathbf{r})]$ is the kinetic energy of non-interacting electrons that possess the same density as the real interacting system. The existence of such a non-interacting system is assumed and still remains an open question in general. The second term in Equation 3.2 is the Coulomb electronic repulsion. $E_{xc}[n(\mathbf{r})]$ is the remaining correction, and is known as the exchange-correlation energy. The minimisation of this functional under the constraint of a given number of particles leads to the formally exact system of single-particle Kohn-Sham equations:

D. Hartree
1897–1958

$$\left[-\frac{\hbar^2}{2m}\nabla^2 + V_{eff}(\mathbf{r})\right]\Phi_i(\mathbf{r}) = \epsilon_i\Phi_i(\mathbf{r}), \tag{3.3}$$

$$\text{where} \qquad V_{eff}(\mathbf{r}) = v_{ext}(\mathbf{r}) + e^2\int \mathbf{dr}'\frac{n(\mathbf{r}')}{|\mathbf{r}-\mathbf{r}'|} + \frac{\delta E_{xc}[n]}{\delta n(\mathbf{r})}, \tag{3.4}$$

$$\text{and} \qquad n(\mathbf{r}) = \sum_{i=1}^{N}|\Phi_i(\mathbf{r})|^2. \tag{3.5}$$

These equations describe a system of non-interacting particles in an effective potential $V_{eff}(\mathbf{r})$ at zero temperature. The effective potential consists of the external imposed potential $v_{ext}(\mathbf{r})$, the electrostatic Hartree interaction between the electrons, and the exchange and correlation potential. The system must be solved self-consistently, since the effective potential $V_{eff}(\mathbf{r})$ depends on the charge density $n(\mathbf{r})$, which is in turn determined by the sum over the N wave functions of lowest energy. In practice, a guess for the charge density is taken as a starting point,[1] from which a set of wave functions are determined by solving the one-particle Schrödinger Equation 3.3. A new charge density is thus obtained and

---

[1] For our solid-state calculations, we use a superposition of atomic charges as an initial guess.

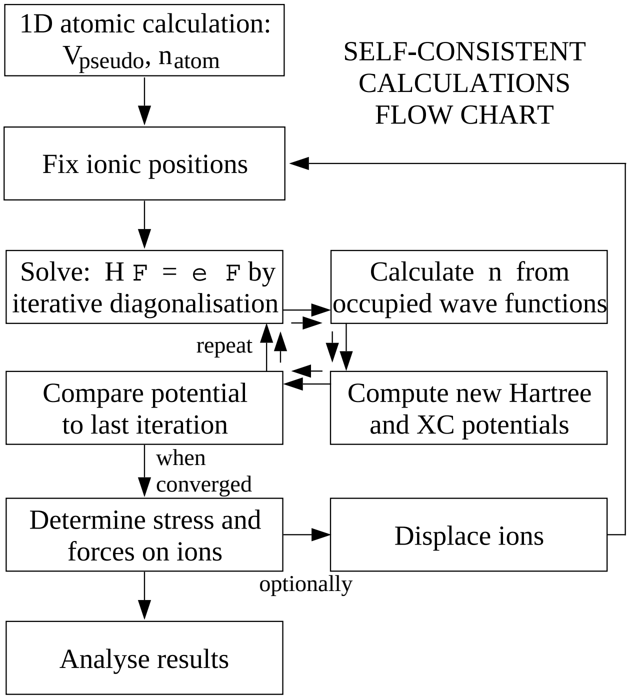

Figure 3.1: Self-consistent calculations flow-chart showing the hierarchical iterative structure of our computations. A pseudopotential calculation is first performed for an isolated atom (see Section 3.5), which gives the atomic charge density. Then, for solid-state systems, the potential of the crystal, including the exchange-correlation term (see Section 3.3), is iterated to self-consistency. Finally, the forces on the ions are determined, the ions are optionally relaxed and the process is repeated.

the process repeated until convergence is reached, as shown in diagrammatic form in Figure 3.1. When the self-consistent charge density is known, the ions can be optionally relaxed to their equilibrium positions. The Hellmann-Feynman theorem [68] allows the forces exerted on the ions to be calculated and the relaxations determined.

In principle, the eigenvalues ϵ_i of the Kohn-Sham equations do not have a physical signification, since they enter the formalism as Lagrange parameters to ensure orthogonality between the wave functions Φ_i. However, for lack of a simple alternative and with empirical justification, it has become standard practice [65] to interpret the ϵ_i as estimates of the excitation energies and compare them in solids with experimental band structures.

There is an important exception that concerns the energy ϵ_N of the highest occupied state in any infinite system. For an extended highest-occupied wave function and neglecting the polarisation effects after removing an electron, the chemical potential μ can be shown to be exactly given by ϵ_N [26].[2] The correction to the chemical potential due to electronic relaxation vanishes as the volume of the metal tends to infinity [35]. For macroscopic metallic systems, we can therefore identify the Kohn-Sham eigenvalue of the highest-occupied state with E_F and compute the work function from Equation 2.2. This approach accounts for all

---

[2] This DFT theorem is the analogue of Koopman's theorem for Hartree-Fock theory.

many-body effects when the electron is extracted, such as the work performed against the image force [15].

3.3 Local density approximation

The exchange-correlation potential still needs to be defined in order to specify the problem completely. This can only be done approximately since the energy functional $F[n]$ is not generally known. The approximation most generally used is the Local Density Approximation (LDA), which exploits the knowledge of the exchange and correlation energy $\varepsilon_{xc}(n)$ of a homogeneous electron gas of density n that has been obtained from alternative theoretical methods. In LDA, the total exchange-correlation energy $E_{xc}[n]$ is given by locally applying the exchange-correlation energy calculated for a uniform gas:

$$E_{xc}[n] = \int \mathbf{dr}\; n(\mathbf{r})\; \varepsilon_{xc}(n(\mathbf{r})). \tag{3.6}$$

This form leads to an effective potential with a local exchange-correlation contribution:

$$V_{eff}(\mathbf{r}) = v_{ext}(\mathbf{r}) + e^2 \int \mathbf{dr}' \frac{n(\mathbf{r}')}{|\mathbf{r}-\mathbf{r}'|} + \varepsilon_{xc}(n(\mathbf{r})). \tag{3.7}$$

If the electronic density $n(\mathbf{r})$ is constant, this procedure is exact, while if $n(\mathbf{r})$ varies slowly on the scale of the Fermi wavelength, it provides a good approximation. At crystalline surfaces the electronic density falls rapidly to zero and the justification for this approximation may seem questionable. Experience has shown nevertheless that for a large class of problems, including atoms, molecules and bulk solids, LDA provides an adequate description that is simple to implement [65].

In this work, we use the parametrisation of $\varepsilon_{xc}(n)$ provided by Perdew and Zunger [69], based on the work of Ceperley and Alder [70], who performed quantum Monte-Carlo simulations of a uniform electron gas over a wide range of densities. The exchange and correlation potential used in this work is shown in Figure 3.2. In the low-density limit, the exchange-correlation potential is inversely proportional to r_s:

$$\varepsilon_{xc}(n) \sim -\frac{1}{r_s} \sim -n^{1/3}. \tag{3.8}$$

Improvements to LDA require using non-local exchange-correlation functionals. The semi-local generalised gradient approximation (GGA) is a first step in this direction. This correction to LDA parametrises the functionals using not only the charge density n, but also its gradient ∇n. However, using this extension, work functions have been shown to change only slightly (less than 0.1 eV) compared with LDA [71].

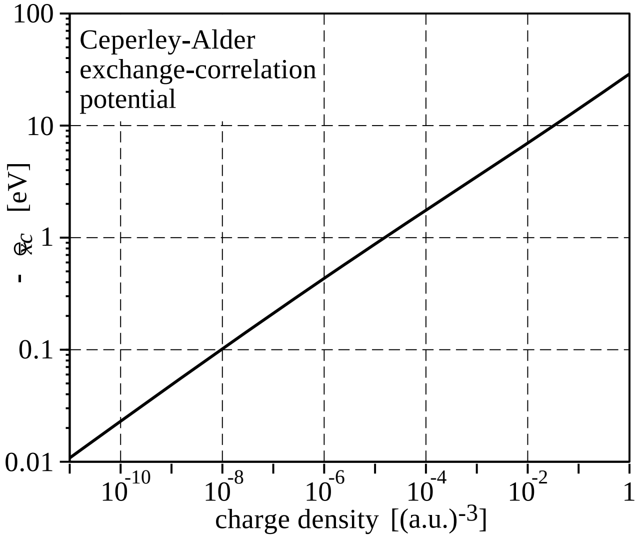

Figure 3.2: Ceperley-Alder local density approximation of the exchange and correlation potential (in eV), as a function of the charge density (in a.u.$^{-3}$). Logarithmic scales are used on both axes.

For metallic surfaces, of particular interest in this work, the LDA approximation has one major disadvantage, namely that it leads to a qualitatively incorrect asymptotic form of the exchange-correlation potential in the vacuum. The correct behaviour of this potential far outside a metal should follow the image charge law and decay as $-e^2/4(z-z_0)$, where $z-z_0$ represents the distance to the effective metal surface. The long-range image potential is a many-body effect and results from the polarisation charge induced at the metal surface when an electron leaves the crystal. Within LDA and in view of Equation 3.8, the exchange-correlation potential decays exponentially with the charge density in the vacuum. This shortcoming does not influence significantly the value of the work function [19], but it crucially affects the shape of the surface barrier and our ability to predict the existence and energies of image-potential surface states. A number of non-local procedures have been proposed recently to correct this flaw, notably for jellium [72, 73] and aluminium [9] surfaces.

3.4 Crystalline periodicity and Brillouin-zone integrations

In solid state studies, it is customary to consider periodic systems, which provide a useful idealisation and for which a large amount of theory has been developed. At first sight, this might seem a limitation for crystalline surfaces, where the three-dimensional bulk symmetry is broken in one spatial direction. However, by means of the supercell technique, which we will detail in Chapter 4, the periodicity perpendicular to the surface is recovered, allowing surfaces to be explored as conveniently as bulk crystals, using exactly the same formalism.

Following the Bloch theorem, the eigenfunctions $\Phi_{\mathbf{k}}^{n}(\mathbf{r})$ of the Kohn-Sham equations can be indexed by a vector $\mathbf{k}$ in the first Brillouin zone and a band number n, and be associated with an energy $\epsilon_{\mathbf{k}}^{n}$. The periodicity of the crystalline structure allows us to expand the wave functions $\Phi_{\mathbf{k}}^{n}(\mathbf{r})$ on a natural plane-wave basis:

F. Bloch
1905–1983

$$\Phi_{\mathbf{k}}^{n}(\mathbf{r}) = \left(\sum_{\mathbf{G}} \Phi_{\mathbf{k}}^{n}(\mathbf{G})\, e^{i\mathbf{G}\mathbf{r}} \right) e^{i\mathbf{k}\mathbf{r}} \tag{3.9}$$

where $\mathbf{G}$ covers all the reciprocal lattice vectors and $\Phi_{\mathbf{k}}^{n}(\mathbf{G})$ are the wave function components in reciprocal space. For computational purposes this sum is restricted to a finite number of terms by retaining only the plane waves with a kinetic energy below a certain cutoff E_{cut}:

$$\frac{\hbar^2}{2m}|\mathbf{k}+\mathbf{G}|^2 \leq E_{cut} \tag{3.10}$$

The cutoff energy controls in a systematic way the precision of the calculation, and is typically on the order of 16 to 36 Ry. It depends sensitively on the elements under consideration, by way of the pseudopotential smoothness (see Section 3.5).

In our implementation for determining the self-consistent electronic density, most of the calculations are performed in reciprocal space. The variational freedom of the wave functions is explicitly stored in the plane-wave coefficients $\Phi_{\mathbf{k}}^{n}(\mathbf{G})$, which are obtained by diagonalising the Hamiltonian matrix in the plane-wave basis using an iterative algorithm. The potentials and the total energy of the solid, as well as the forces and stresses, can be derived directly from the coefficients $\Phi_{\mathbf{k}}^{n}(\mathbf{G})$ [74, 68]. In reciprocal space, the Poisson equation is conveniently solved to determine the Hartree potential, and when needed, Fast Fourier Transforms (FFT) enable efficient transitions between real and reciprocal space.

J. Fourier
1768–1830

To determine the electronic charge density in a periodic system from Equation 3.5, an integration over the entire Brillouin zone (BZ) is generally required. This task depends in principle upon a calculation of the wave functions and corresponding energies at a large number of points inside the first Brillouin zone. In order to minimise the computational effort, it is possible to consider the symmetries of the crystal and use only a small number of well-chosen special points to obtain a good approximation of the full quadrature.

We use a uniform grid of points proposed by Monkhorst and Pack [75], who generalised the unique mean-value point first proposed by Baldereschi [76]. By optimising the choice of the integration points, these techniques seek to integrate exactly the first few terms in the Fourier expansion of all functions with the given

Figure 3.3: Brillouin zone for a face-centered cubic crystal with its points of high symmetry. The shaded wedge represents the irreducible portion of the Brillouin zone where the reduced k-points are located.

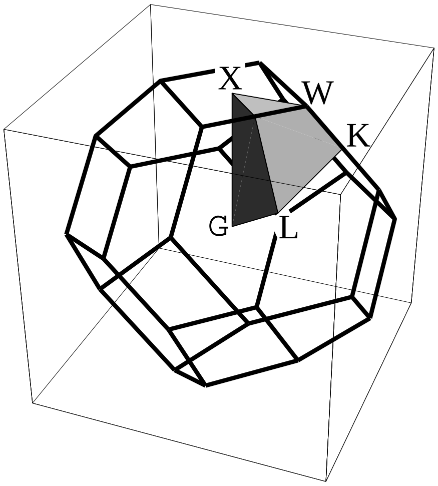

crystalline periodicity. In real space, this procedure corresponds to a periodic interpolation, of correct crystalline symmetry, to the function of interest between selected points in the BZ.

The procedure for finding the special k-points is sketched below. First, we generate a uniform grid $\mathbf{k}_{\{q_i\}}$ in reciprocal space, along the reciprocal unit vectors $\mathbf{b}_i$:

$$\mathbf{k}_{\{q_i\}} = \mathbf{k}_0 + \sum_{i=1}^{3} q_i \mathbf{b}_i, \tag{3.11}$$

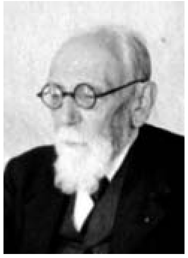

M. Brillouin
1854–1948

where the q_i index a collection of uniformly spaced points between $-1/2$ and $1/2$. The number of points N_i along each axis ultimately influences the precision of the calculation and must be chosen with care. Using the symmetries of the crystal, the grid can be reduced to a smaller one without changing the result of the integration. By identifying points related by a point-group symmetry element of the crystal, adding inversion if missing, equivalent points can be removed as long as the weight w_m associated with the remaining point $\mathbf{k}_m$ is increased correspondingly. The full grid is then reduced to a small grid of points that can be positioned in a fraction of the first Brillouin zone. The resulting irreducible Brillouin zone is shown for a face-centered cubic crystal in Figure 3.3. The shift of origin $\mathbf{k}_0$ does not affect the quadrature precision [77] and is chosen to minimise the final number of reduced points $\mathbf{k}_m$. In the Monkhorst-Pack scheme, this leads to $\mathbf{k}_0 = 1/2 \sum_i \mathbf{b}_i/N_i$. With a normalisation to $1/\Omega$ of the weights w_m (Ω is the real-space unit cell volume), the quadrature of the charge density $n(\mathbf{r})$ is then given approximately by a sum over the occupied states:

$$n(\mathbf{r}) = \sum_n \frac{1}{(2\pi)^3} \int_{BZ} \mathbf{dk}\, |\Phi^n_{\mathbf{k}}(\mathbf{r})|^2 \simeq \sum_{n,m} w_m |\Phi^n_{\mathbf{k}_m}(\mathbf{r})|^2. \tag{3.12}$$

There is an additional difficulty associated with metals, which possess partially filled bands near the Fermi level. The Fermi surface often has a complicated shape, leading to a slow convergence with the number of k-points used. To position the Fermi level accurately, we employ a Gaussian smearing of the electronic levels [78]. By replacing each calculated electronic level $\epsilon^n_{\mathbf{k}_m}$ by a Gaussian distribution centered at that energy, we obtain a continuous density of states (DOS) $\mathcal{N}(E)$:

$$\mathcal{N}(E) = \sum_{n,m} w_m \delta(E - \epsilon^n_{\mathbf{k}_m}) \Rightarrow \sum_{n,m} \frac{w_m}{\sqrt{2\pi}\sigma} \exp\left(-\frac{(E - \epsilon^n_{\mathbf{k}_m})^2}{2\sigma^2}\right). \tag{3.13}$$

The Fermi level is then fixed by imposing the correct total charge density below the Fermi level. This procedure leads to fractional occupation numbers in the neighbourhood of the Fermi level. In the limit of very small broadenings, the computed ground state electronic density minimises the total energy.[3] In this work, we have always used a broadening of $\sigma = 0.01$ Ry for each k-point.

3.5 Pseudopotentials

In our adiabatic model of the crystals, the electrons move in a periodic external potential created by the nuclei. For a crystal with atoms of atomic number Z_j located at $\mathbf{R} + \mathbf{t}_j$, where $\mathbf{R}$ is a Bravais lattice vector and $\mathbf{t}_j$ gives the position of the atom within the unit cell, the all-electron external potential is:

$$v_{ext}(\mathbf{r}) = -\sum_{\mathbf{R},j} \frac{Z_j e^2}{|\mathbf{r} - \mathbf{R} - \mathbf{t}_j|}. \tag{3.14}$$

The direct resolution of the Hamiltonian describing $\sum_j Z_j$ valence and core electrons per unit cell moving in this external potential is a challenging task. In view of the divergence of the Coulomb potential, not only are the electronic energies spread over a very wide range, but the characteristic length scales of the various wave functions are also broadly distributed.

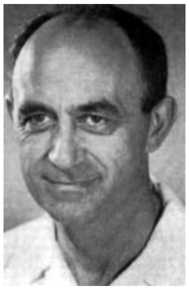

E. Fermi
1901–1954

However, the deep core-electron wave functions are tightly bound to the nuclei and their spatial distribution remains essentially unchanged from one chemical environment to another.[4] On the contrary, the valence electrons are higher in energy and are strongly influenced by the neighbouring atoms. This insight has lead

---

[3] In a free electron gas, the convergence to the exact total energy depends quadratically on the broadening. Finite broadenings may lead to errors on the computed Hellman-Feynman forces which could affect the ionic relaxations. For Al(111) surfaces, tests have shown that even with typically large broadenings, the error on the equilibrium position of the surface layer is only 10^{-3} nm [79].

[4] The core states of atoms at surfaces are often slightly shifted in energy compared with those in the bulk. These surface core-level shifts have been measured by observing the corresponding

to the development of pseudopotentials, which replace the influence of frozen core states on the valence electrons by an effective external potential. The crystalline Hamiltonian then describes only the valence electrons in an effective potential, a substantial computational saving for complex systems.

There are a number of different schemes for constructing pseudopotentials from first principles (for a review, see [81]). One popular family consists of the so-called *norm-conserving* pseudopotentials. These potentials are generated from one-dimensional radial atomic calculations in the spherical screening approximation and are chosen to meet a number of criteria:

1. The pseudo wave functions generated from the pseudopotential should contain no nodes.
2. Beyond a certain cutoff radius, the pseudo and all-electron wave functions should be equal.
3. The charge enclosed inside the cutoff radius must be equal for the two wave functions. Taken in conjunction with the second condition, this implies that the valence all-electron and pseudo eigenvalues are identical.

The cutoff radius determines the transferability of the pseudopotential between different chemical environments and is often adjusted manually. A low cutoff radius corresponds to a small region where the pseudo wave functions are not meaningful and a high transferability. However, the cutoff radius cannot be reduced below below the outer-most node of the all-electron wave functions without contradicting the first design criterion. Furthermore, small cores induce strongly-varying effective potentials that are undesirable for further calculations since they necessitate a large number of plane waves as basis functions.

There is still a considerable amount of freedom available in the exact choice of potential. In this work, we have used potentials generated with the method of Troullier and Martins [82]. This scheme provides smooth pseudopotentials for most elements of the periodic table, and is well adapted to a plane-wave basis for describing the wave functions. The smoothness ensures that only a small number of plane waves are required as basis functions. The Troullier-Martins pseudopotentials V_{TM} are semi-local, *i.e.* local in the radial component and non-local in the angular component. They can be decomposed into a long-range fully-local radial part $V_L(r)$ and a set of short-range semi-local projection operators $\Delta V_l(r) = V_l(r) - V_L(r)$ that depend on the orbital momentum l of the pseudo

---

peaks in X-ray photoemission spectroscopy [20], and have been interpreted in terms of the change in electrostatic potential in the top ionic layer [80]. Such core effects are not readily obtainable with our pseudopotential technique, since the core states are not explicitly recalculated for each physical environment.

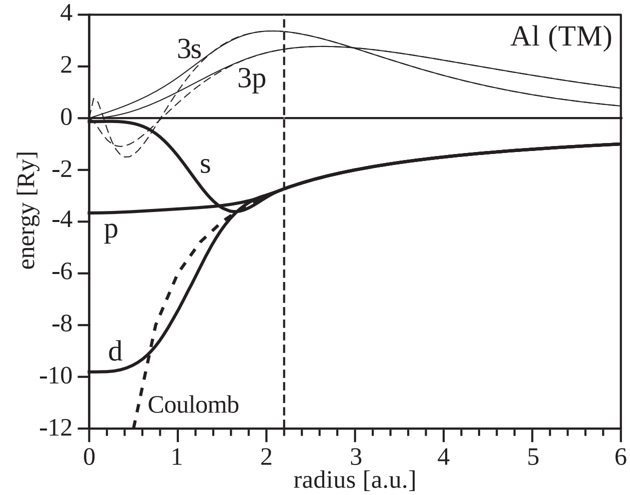

Figure 3.4: Al Troullier-Martins pseudopotential. Thick lines: the various orbital components of the pseudopotential (solid lines) and the Coulomb tail (dashed line). Superimposed in thin lines are the pseudo wave functions (solid lines) and corresponding all-electron wave functions (dashed lines). The vertical dashed line shows the cutoff radius, fixed here at 2.20 a.u.

wave functions. The Troullier-Martins pseudopotentials are thus written (with the spherical harmonics $|Y_{lm}\!>$):

$$\begin{aligned} V_{TM}(r) &= \sum_{l,m} |Y_{lm}\!>V_l(r)<\!Y_{lm}| && (3.15)\\ &= V_L(r) + \sum_{l,m} |Y_{lm}\!>\Delta V_l(r)<\!Y_{lm}|. && (3.16)\end{aligned}$$

In Figure 3.4, we display the components $V_l(r)$ of our Troullier-Martins pseudopotential for aluminium, one of which can be chosen as the local potential $V_L(r)$, as well as the long-range Coulomb tail corresponding to the three valence electrons. For aluminium, we choose the p pseudopotential component as the local one. Also shown are the pseudo wave functions and corresponding all-electron wave functions.

C. de Coulomb
1736–1806

Our pseudopotentials are then treated in the Kleinman-Bylander (KB) approximation [83]. These authors realised that by replacing the semi-local components of the pseudopotential by fully non-local components, a substantial amount of computing time and resources could be saved when calculating matrix elements between wave functions and pseudopotentials. This leads to a pseudopotential $V_L(r)+V_{NL}$, with V_{NL} given by:

$$V_{NL} = \sum_{l,m} \frac{|\Delta V_l\,\Phi^o_{lm}\!><\!\Phi^o_{lm}\,\Delta V_l|}{<\!\Phi^o_{lm}|\Delta V_l|\Phi^o_{lm}\!>}, \qquad (3.17)$$

where the $\Phi^o_{lm}(r)$ are the pseudo wave functions of the pseudopotential $V_{TM}(r)$. The matrix elements of V_{NL} between two sums of plane waves allow a convenient factorisation, leading to higher speed and lower memory requirements in the computations. The KB approximation has thus allowed systems with a greater number of atoms per unit cell to be investigated.

Fussy Electrons

An electron is sure hard to please.
When spread out, it sometimes will freeze.
    Though agoraphobic,
    It’s still claustrophobic,
And runs off when put in a squeeze.

David Morin, Eric Zaslow, E’beth Haley, John Golden, and Nathan Salwen

Chapter 4

Work functions from thin slabs

4.1 Introduction

IONISATION potentials of solids, and in particular work functions of metals, are nowadays best calculated by *ab initio* methods [62, 84], in the framework of density functional theory (see Section 3.2). These calculations present a theoretical challenge, since the work function depends sensitively on the surface ionic and electronic charge distributions, and may be influenced by any surface atomic relaxation or reconstruction. The most efficient first-principles methods generally make use of slab configurations to calculate surface properties. In view of the heavy numerical operations involved, such calculations are usually performed by restricting the study to slabs containing only a small number of atomic planes. If adsorbed atoms or molecules are included in the analysis, the substrate is often reduced to a few atomic layers [85, 86]. However, the electronic properties of nanometer-sized thin metallic films are different from those of a bulk metal due to the lowering of the dimensionality of the crystal [19]. The variations of the physical properties with the thickness of the film, known as Quantum Size Effects (QSE), have been shown to influence significantly the surface energies and work functions of thin metallic slabs [87–90]. In particular, persistent quantum-size oscillations of 0.1 eV have been exhibited recently in the work functions of Al(111) slabs up to twelve atoms thick [91]. These oscillations and the resulting slow convergence of the work functions with slab thickness hinder a precise determination of the work functions of semi-infinite crystals.

In this chapter, we first describe the slab and supercell techniques generally employed in surface calculations and discuss the approach commonly used to derive work functions from thin-film computations. In particular, we consider the QSE consequences on the electronic structure and work function of using thin slabs. We then present a method based on macroscopic averages of the total charge density that can be used to reduce the QSE and determine precisely the work

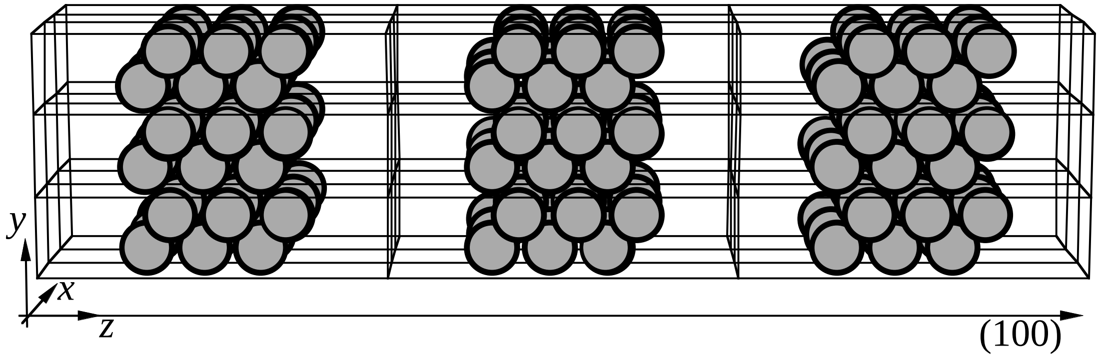

Figure 4.1: Supercell slab geometry: three-dimensional view of a periodically-repeated supercell describing the (100) surface of a face-centered cubic metal. Each supercell contains 6 atoms, arranged in consecutive atomic planes to form a thin (100) slab, surrounded by 6 equivalent vacuum layers. The artificial repetition of parallel slabs is illustrated.

functions of semi-infinite metallic crystals from *ab initio* thin-film calculations [92]. The technique is applied to a series of Al(100) slabs.

4.2 Slabs and supercells

The electronic structure of a crystalline thin film can be calculated from first principles using a variety of different approaches. For example, self consistent calculations of a single isolated slab using a set of localised basis functions can be performed to obtain the slab wave functions [93, 94]. However, the quality of the basis is often difficult to test in this case, and large numbers of multi-centre integrals generally need to be evaluated. Alternatively, one can consider repeated thin slabs, a technique first applied by Chelikowsky *et al.* [95], so retaining a three-dimensional periodicity throughout space. A discrete set of plane waves then provides an orthogonal basis with a number of advantages. The accuracy of the plane-wave basis is controlled in a systematic way by the kinetic cutoff energy E_{cut} (see Section 3.4), which is kept to a minimum by employing optimised pseudopotentials (see Section 3.5). In addition, a particularly simple formulation of the Kohn-Sham equations (Equation 3.5) is obtained in reciprocal space, and can be used for both bulk and surface studies. This combined plane-wave and supercell approach is the technique we have adopted in this thesis.

To perform a supercell calculation, one defines a unit cell oriented with one axis perpendicular (and two parallel) to the surface of interest, containing the inequivalent atoms of a crystalline thin film and some vacuum layers. In Figure 4.1, we display a typical supercell—periodically repeated—adapted for a fcc (100) surface.

Here, six atomic layers of metal and six equivalent vacuum layers form each supercell. The periodic arrangement of the supercells along the z direction, perpendicular to the crystal surface, gives rise to an artificial metal/vacuum superlattice configuration. Ideally, the thicknesses of the vacuum layer and of the slab must be sufficient for two successive metal surfaces not to interact significantly. The required thicknesses depend on the physical quantities under consideration—such as the work function, the surface atomic relaxation or the spatial distributions of the surface electronic states—as well as on the calculational procedures to obtain them. The sensitivity of the results on the film thickness is best established from repeated calculations, by varying the number of atomic planes in the supercell.

4.3 Quantum size effects

In this section, we examine the impact of QSE on the electronic structure of thin metallic slabs. As a prototypical system, we focus on the aluminium (100) surface. The calculations presented in this section as well as in the remaining part of this chapter are performed using the *ab initio* methodology described in Chapter 3. We consider unrelaxed slabs sandwiched between 6 equivalent vacuum layers, in a supercell geometry. We use a Troullier-Martins pseudopotential, with a plane-wave kinetic energy cutoff of 16 Ry and 45 reduced k-points, to determine the self-consistent charge density.[1]

The influence of QSE on the electronic properties of thin films can be seen by comparing the local density of states (LDOS) $\mathcal{N}(E,\mathbf{r})$, which gives a combined energy E and spatial probability distribution of the slab electronic states ($\Phi^n_{\mathbf{k}}$, $\epsilon^n_{\mathbf{k}}$), with the corresponding density of states (DOS) in a bulk crystal. The LDOS is defined as:

$$\mathcal{N}(E,\mathbf{r}) = \sum_n \frac{1}{(2\pi)^3} \int_{BZ} |\Phi^n_{\mathbf{k}}(\mathbf{r})|^2 \, \delta(E-\epsilon^n_{\mathbf{k}}), \tag{4.1}$$

where the integral is taken over the Brillouin Zone (BZ) and the sum over all the bands n. We have calculated averages of the local density of states over the various atomic layers in the slab. The local density of states $\mathcal{N}_j(E)$ for plane j, located at an abscissa z_j, is then equal to:

$$\mathcal{N}_j(E) = \frac{1}{d} \int_{z_j-d/2}^{z_j+d/2} dz \, \overline{\mathcal{N}}(E,z), \tag{4.2}$$

where d is the interplanar spacing of the slab and $\overline{\mathcal{N}}(E,z)$ represents the average of $\mathcal{N}(E,\mathbf{r})$ in a plane parallel to the film surface. For calculational purposes, the

---

[1] The first step in these calculations is to determine the theoretical lattice constant of the element under investigation, using the procedure detailed in Appendix A.1. This preliminary stage allows us to model crystals in the absence of any external pressure. For Al, we obtain a lattice constant $a_0 = 7.51$ a.u.

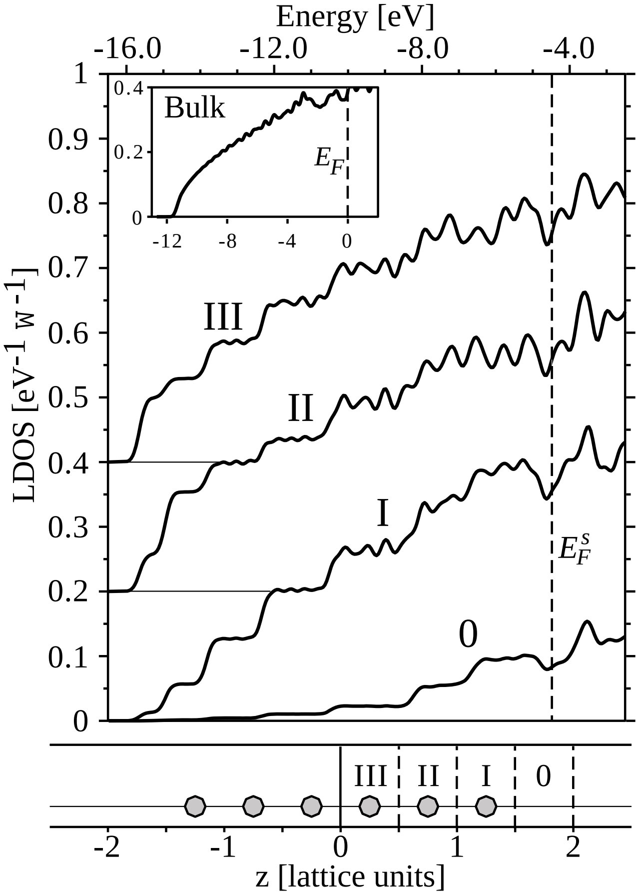

Figure 4.2: Local density of states in an Al(100) 6-layer thin slab, per eV and per unit cell Ω. Curves 0 to III have been calculated in the corresponding regions indicated at the bottom of the figure and exhibit the LDOS of layers increasingly deep in the slab. Curves II and III have been shifted vertically to enhance the readability. The energy zero is set at the vacuum level and the Fermi energy of the slab E_F^s is indicated by the vertical dashed line at −4.41 eV. The inset shows the density of states in a bulk Al crystal, referenced to the bulk Fermi energy E_F.

integral over the Brillouin zone in Equation 4.1 is approximated by a weighted sum over a large number of Monkhorst-Pack k-points [75], and the Dirac function is broadened into a Gaussian.

In Figure 4.2, we show the LDOS of a 6-layer-thick Al(100) slab. Given the smallness of the interslab tunnelling across the vacuum region, the electronic wave functions of the system are practically confined in the well formed by the thin metallic slab and are quantised in the transverse direction by virtue of its extreme thinness. The transverse squeeze induces a subband spacing on the order of 1 eV, much larger than the meV separations generally seen in semiconductor quantum wells (which are typically 100 nm thick) [96]. The subbands are clearly reflected in the LDOS of Figure 4.2, where a series of steps that are reminiscent of two-dimensional systems are seen. Even at the centre of the film, the LDOS does not recover the parabolic shape of the Al bulk density of states, emphasizing the importance of QSE. The individual electronic wave functions and energies of the metal slab in a vacuum thus differ strongly from those of the bulk metal, and are not representative either of a semi-infinite crystal.

In Figure 4.3, we compare the total density of states computed for the 6-

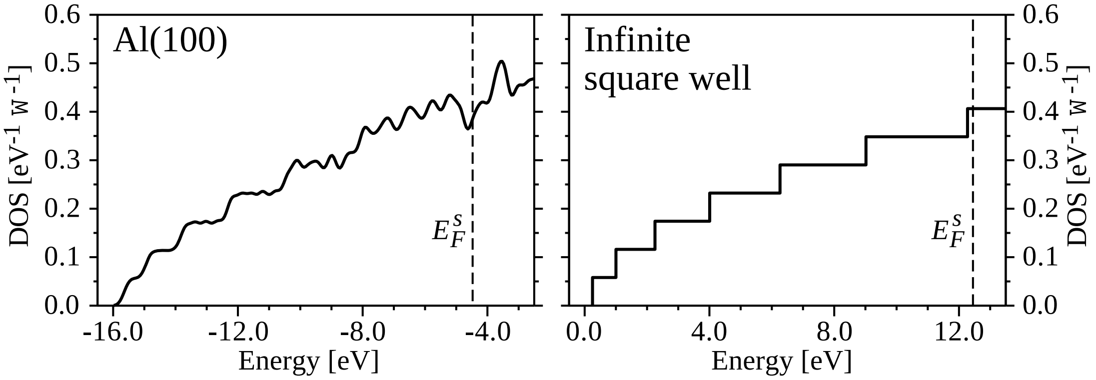

Figure 4.3: Left panel: Density of states in an Al(100) 6-layer thin slab, per eV and per unit cell Ω. Right panel: Density of states in an infinitely-deep rectangular well of thickness equal to the Al(100) 6-layer slab and of electronic density equal to that of Al. The Fermi energies E_F^s are indicated in both cases.

layer-thick Al(100) slab with the density of states obtained from an analytical description of the electronic states in a square-well potential. In this model, we consider free electrons in an infinitely-deep thin film of thickness w. The subbands E_n and DOS $\mathcal{N}(E)$, per unit area, are then given by:

$$E_n = \frac{\pi^2\hbar^2 n^2}{2m^* w^2}, \quad n \geq 1, \tag{4.3}$$

$$\mathcal{N}(E) = \frac{m^*}{\pi\hbar^2 w}\sum_{n\geq 1}\theta(E - E_n), \tag{4.4}$$

where m^* is the electronic effective mass, fixed here equal to the effective mass at the conduction band minimum of real Al ($m^* = 1.06m$), and $\theta(x)$ is the unit step function. By setting the electronic density in the well equal that of real Al, the Fermi energy E_F^s can be determined in the model. Figure 4.3 shows that this simple model provides a satisfactory general description of the DOS of the self-consistent calculations when the thickness w is chosen equal to the 1.2-nm thickness of the Al(100) 6-layer slab. We may thus use this model to extrapolate the impact of QSE on the density of states of thicker Al films. Based on this approach, one finds that slabs as thick as 6 nm (or 30 layers) are needed to reduce the subband spacings by a factor of 25 and render the influence of QSE on the DOS reasonably small (compare Figure 4.4 and the inset in Figure 4.2).

We would like to note that the results above do not necessarily mean that all electronic properties converge as slowly as the DOS with the slab thickness. However, great caution is needed when deriving surface properties from computations performed for thin films in a vacuum. In this respect, the situation is quite different from that observed in supercell calculations of interface proper-

Figure 4.4: Density of states in an infinitely-deep rectangular well of thickness $w = 6$ nm, *i.e.* equal to the thickness of an Al(100) 30-layer slab, per eV and per Al unit cell Ω. The Fermi energy E_F^s is indicated for an electronic density equal to that of Al.

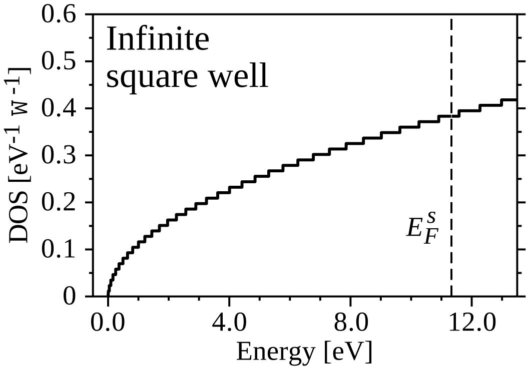

ties in metal/semiconductor structures, such as Al/GaAs(100) heterostructures [97], where QSE are much smaller. It is interesting to note that QSE have also been observed experimentally in metallic films of thicknesses comparable to those discussed here. In particular, photoemission spectroscopy of 1–3-layer-thick Na films on Si has revealed discrete electronic levels confined to the alkali overlayer [98]. Resistivity measurements of 1–10 nm NiAl layers grown by molecular-beam epitaxy between AlAs barriers have also shown discrete electronic states in the resulting metallic quantum well [99].

4.4 Methods for calculating work functions

As a consequence of the arbitrariness in defining a reference potential, the work function of a metal W can be obtained from *ab initio* calculations in a number of distinctive ways. Using the mean electrostatic potential energy in the metal interior as the reference energy, Equation 2.2 can be written:

$$W = \Delta V_{el} - E_F, \tag{4.5}$$

where ΔV_{el} is the rise in the mean electrostatic potential energy across the metal surface, and E_F is the Fermi energy relative to the mean electrostatic potential energy in the metal interior. Alternatively, if the energies are referred to the potential in the vacuum far from the surface, the work function is directly given by the negative of the Fermi energy (which we now write E_F^s) [87, 15]:

$$W = -E_F^s. \tag{4.6}$$

Work functions are commonly evaluated using this expression, by measuring the Fermi energy E_F^s of thin slabs with respect to the potential in the vacuum region [87–90, 100–103].

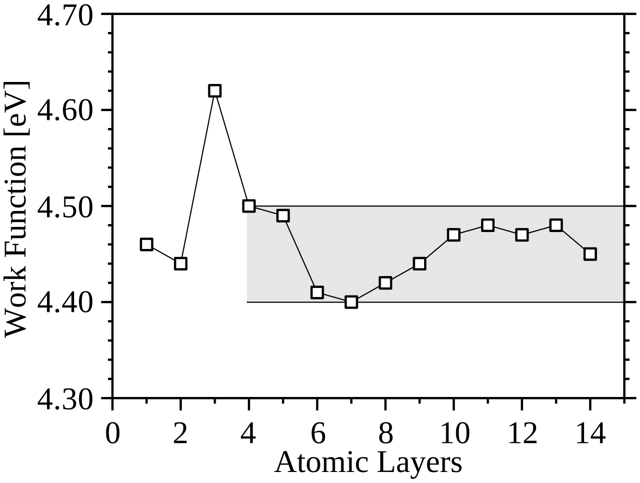

Figure 4.5: Work functions W of Al(100) thin films (in eV), as a function of the slab thickness, computed using the position of the slab Fermi level: $W = -E_F^s$. The shaded area indicates the uncertainty range for slabs thicker than 3 atomic layers.

4.4.1 Work functions using the slab Fermi energy

In Figure 4.5, we present the work functions of a series of thin slabs of Al(100) with an increasing number of atomic planes (1 to 14), calculated using Equation 4.6.[2] Large oscillations in the work function appear across the full range of slabs investigated. We emphasize that in our supercell computations, the slab Fermi energy entering Equation 4.6 is calculated with respect to the electrostatic potential in the middle of the supercell vacuum region. As we will see in Section 4.5, the electrostatic potential is well converged in the vacuum part of the supercell. The oscillations observed in Figure 4.5 therefore fully reflect the changes with film thickness in the Fermi energy E_F^s of isolated slabs.

We have seen in Section 4.3 that the energies of the electronic states of the slab strongly differ from those of the bulk because of QSE. The approach based on Equation 4.6 for determining the work function therefore suffers from large quantum-size oscillations, as it depends explicitly on the energies of the slab electronic states.

4.4.2 Work functions using macroscopic averages

In view of estimating precisely the work function of a semi-infinite crystal from thin-film calculations, one should avoid the use of Equation 4.6 and calculate the work function using slab quantities which are less sensitive to size effects than the Fermi energy. The total (electronic and ionic) charge density of the slab and the corresponding electrostatic potential are such quantities, especially if the macroscopic-average concept is also introduced. The macroscopic-average

---

[2] With the parameters used for the plane wave kinetic energy cutoff (16 Ry), for the k-space integration (45 reduced k-points) and for the Gaussian broadening (0.01 Ry), we estimate that for a given thickness the numerical uncertainty on the Fermi energy is ~0.03 eV.

technique has previously been employed successfully in the study of semiconductor heterojunction band-offsets [25] and Schottky barriers [97]. The electronic density $n(\mathbf{r})$ is the basic variable calculated by all standard *ab initio* codes based on density-functional theory. We first introduce the plane-averaged electronic density $\overline{n}(z) = S^{-1} \int_S n(\mathbf{r})\, dx\, dy$, where the z axis is chosen perpendicular to the slab surface S. The macroscopic-average electronic density $\overline{\overline{n}}(z)$ is then defined from the plane-averaged density by an integration over the interplanar distance d of the slab:

$$\overline{\overline{n}}(z) = \frac{1}{d} \int_{-d/2}^{d/2} \overline{n}(z + z')dz' \tag{4.7}$$

(see Appendix A.2 for further details about this procedure). The electrostatic potential $V_{el}(\mathbf{r})$ is related to the total charge density, including the ionic charge contribution, via the Poisson equation. Since these operations are linear, the plane-averaged potential $\overline{V}_{el}(z)$ is related to its macroscopic average $\overline{\overline{V}}_{el}(z)$ by a relation similar to Equation 4.7: $\overline{\overline{V}}_{el}(z) = d^{-1} \int_{-d/2}^{d/2} \overline{V}_{el}(z + z')\, dz'$. By averaging over the interplanar distance, one evacuates all atomic-scale oscillations and expects stable values to be recovered not too far from the surface. This procedure is best applied to unrelaxed surfaces, where the interplanar distance d is constant. However, it can also be used for relaxed slabs, as long as a minimum number of planes in the centre of the film are kept fixed at their unrelaxed locations, so defining the bulk interplane spacing d to be used for the macroscopic averaging.

In Figure 4.6 we display the planar and macroscopic averages of the electronic charge density and the total electrostatic potential V_{el} for the Al(100) slab with 6 atomic layers previously studied in Figure 4.2. The potential V_{el} includes the electron Hartree potential and the point-charge potential of the Al^{3+} ions.[3] While the planar averages show oscillations in the metal with the periodicity of the atomic planes, the macroscopic averages exhibit very stable values both in the vacuum and in the metal not far from the slab surfaces. In this way, the potential difference ΔV_{el} between the metal and the vacuum can be precisely measured even in very thin films.

To determine more accurately the work function of a semi-infinite crystal, we return to Equation 4.5, exploiting the separation of the work function into a surface-dependent and a bulk contribution. The surface-dependent component ΔV_{el} is evaluated from the thin slab by means of the macroscopic average of the total electrostatic potential (see Figure 4.6). The position of the Fermi level E_F with respect to the average electrostatic potential in the metal is evaluated by a *separate* calculation for bulk Al. This calculation involves a small unit cell, can be performed very precisely with a high cutoff and a large density of k-points

---

[3] Details about the evaluation of the one-dimensional electrostatic potential and of the rise in potential energy across the surface ΔV_{el} can be found in Appendix A.3.

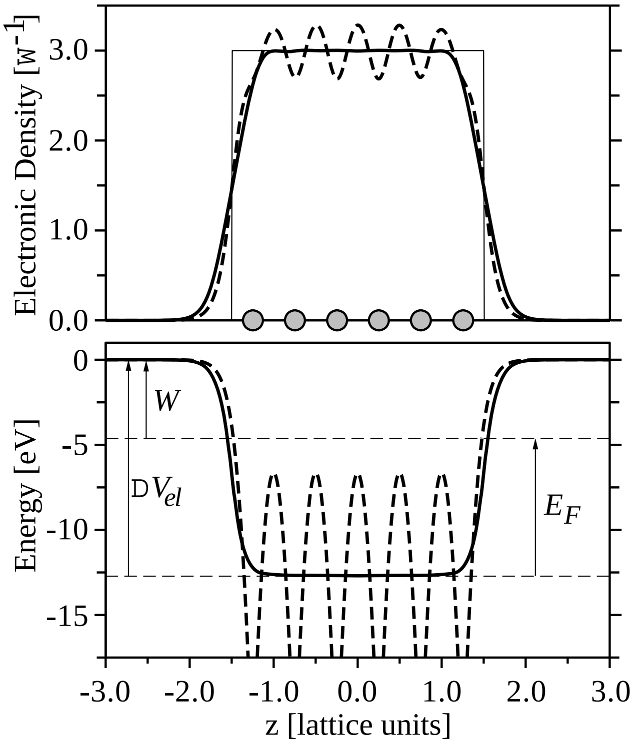

Figure 4.6: Upper panel: Plane-averaged electronic charge density $\overline{n}(z)$ (dashed line) and corresponding macroscopic average $\overline{\overline{n}}(z)$ (solid line), in electrons per unit cell Ω, for an unrelaxed Al(100) 6-layer thin film. The double-step function indicates the macroscopic average of the Al^{3+} point-ion charge density and the grey circles denote the atomic planes. Lower panel: Plane-averaged total electrostatic potential $\overline{V}_{el}(z)$ (dashed line) and corresponding macroscopic average $\overline{\overline{V}}_{el}(z)$ (solid line) for the same film. The bulk Fermi level E_F, the surface electrostatic potential step ΔV_{el}, and the work function W are indicated.

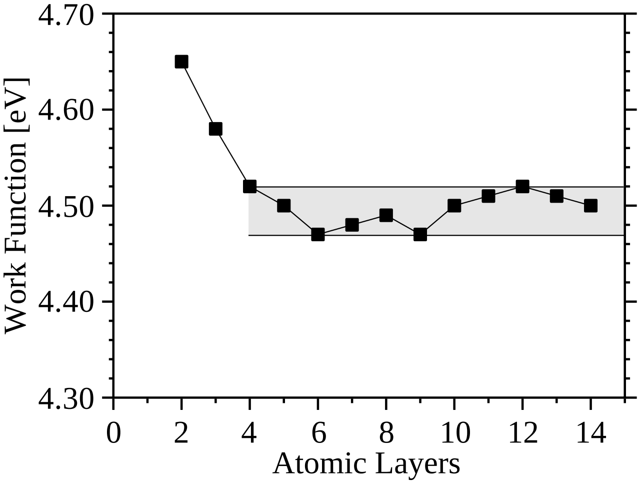

Figure 4.7: Work functions W of Al(100) thin films (in eV), as a function of the slab thickness, calculated by combining the surface potential step of the slab and the bulk Fermi level. The shaded area indicates the uncertainty region above 3 atomic layers.

Figure 4.8: Plane average (left panel) and macroscopic average (right panel) of the electrostatic potential V_{el} (thick solid lines), total local potential V_{loc} (dashed lines), and LDA exchange-correlation potential V_{xc} (thin solid lines) for unrelaxed Al(100) 6-layer thin slabs separated by 6 equivalent vacuum layers. The grey circles correspond to the atomic planes.

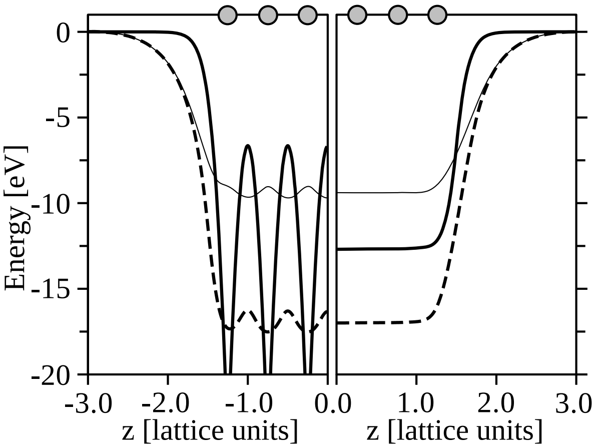

(we use 36 Ry and 570 reduced k-points), and eliminates QSE altogether for this contribution. The precision of the work function W is thus limited essentially by the surface-dependent term ΔV_{el}, whose numerical accuracy we estimate to be comparable to that of the Fermi energy (∼0.03 eV). Although this technique is equivalent to the use of Equation 4.6 for sufficiently thick slabs, we expect Equation 4.5 to be less sensitive to QSE and to converge faster to the work function of the semi-infinite crystal as a function of the slab thickness. Equation 4.5 is less affected by QSE since it relies on the total electron charge density in the slab and not on the individual electronic states. This procedure is thus less sensitive to the details of the thin-film band structure, such as the position of the slab Fermi level that is employed in Equation 4.6.

In Figure 4.7, we present the values of the work functions for the same series of thin slabs as in Figure 4.5, but here computed using the macroscopic-average technique by combining the surface electrostatic potential step with the Fermi energy derived from a bulk calculation. Compared with the results of the standard technique shown previously in Figure 4.5, QSE have been noticeably reduced, the oscillations of the work function above 4 atomic layers having been roughly halved, and convergence within 0.03 eV is achieved with a smaller number of atomic planes.

4.5 Reference potentials

The procedure we propose for accurately calculating the work function exploits a separation of the work function into a bulk contribution and a surface-dependent term. Such a separation is not uniquely defined since the values of the two in-

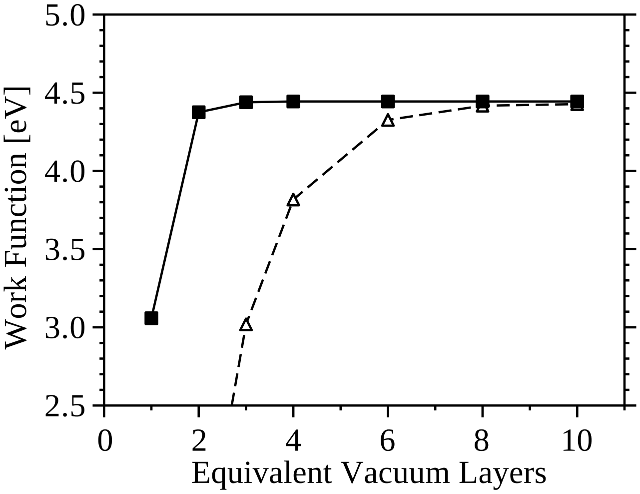

Figure 4.9: Work function of a 6-layer Al(100) slab, as a function of the number of equivalent vacuum layers in the supercell, calculated by combining the bulk Fermi level with the electrostatic potential step ΔV_{el} (solid line) and with the total local potential step ΔV_{loc} (dashed line). The local potential step ΔV_{loc} was calculated with a cutoff of 36 Ry.

dividual terms depend on the possibility of including a number of short-range local components of the crystal potential in either one or the other of the two contributions.[4] We stress that it is only the sum of the two terms, *i.e.* the difference between the Fermi level and the vacuum potential, that is physically meaningful. We have found that the fastest convergence of work function values with slab thickness and plane-wave cutoff is obtained when the exchange-correlation and the so-called alpha terms [74] of the average local crystal potential are included in the bulk contribution. Within LDA, the exchange-correlation term of the crystal potential is a local short-range potential and its average value in the crystal can therefore be included in the bulk Fermi-energy contribution. Similarly, for the surface potential step, it is convenient to use an ionic Coulomb potential generated by point ions, rather than the local part of the ionic pseudopotential. The alpha term, resulting from this difference, can then be included with the bulk contribution.

In Figure 4.8 we compare the electrostatic potential V_{el}, consisting of the electronic Hartree and Coulombic point-ion potentials, with the total local potential V_{loc}, given by the sum of the electronic Hartree potential, the local part of the ionic pseudopotential and the LDA exchange-correlation potential. We also show the exchange-correlation potential V_{xc} only. The macroscopic-average potentials are also represented and have been calculated directly from the corresponding plane-averaged potentials. The electrostatic potential decay in the vacuum is controlled by the extent of the electronic density $\overline{n}(z)$. Far from macroscopic metal surfaces, $\overline{n}(z)$ is known to decrease exactly as $z^{-1}e^{-2kz}$, where k is related to the work func-

---

[4] If pseudopotentials are used, an additional arbitrariness on the bulk and on the surface-dependent contributions to the work function results from the choice of pseudopotential. The work function, however, is again unaffected by this selection.

tion W by $k = \sqrt{2mW}/\hbar$ [104]. The dominant term in the electrostatic potential far from the surface can be extracted by double integration of this charge density, and falls off as $\overline{n}(z)/W$. The convergence of the electrostatic potential V_{el} in the vacuum is thus extremely fast, and 6 equivalent vacuum layers are enough for separating the repeated slabs in Figure 4.8. We note that if metals with smaller work functions than Al are considered, the number of equivalent vacuum planes in the supercell will have to be increased further to account for the increased spreading of the electronic charge into the vacuum.

In Figure 4.8, we observe that V_{xc} accounts for a large proportion of the total potential V_{loc}, and is seen to decrease more slowly in the vacuum than the electrostatic term. The number of equivalent vacuum layers used here proves insufficient for V_{loc} to converge adequately in the vacuum region of the supercell. Therefore, if the total local potential V_{loc} is used to evaluate the surface potential step ΔV_{loc}, a larger number of equivalent vacuum planes (at least 8) are needed in the supercell for the Al work function to converge within 0.03 eV, as observed in Figure 4.9. Furthermore, we find that the cutoff for the slab calculation must be increased (up to 36 Ry for full convergence) when the exchange-correlation and alpha terms are included in the surface-dependent contribution ΔV_{loc}. Both these observations result mainly from the very slow convergence to zero of the LDA potential $V_{xc}(\mathbf{r})$ in the vacuum region, where the charge density $n(\mathbf{r})$ tends to zero and the LDA exchange-correlation potential behaves as $n(\mathbf{r})^{1/3}$ (see Figure 3.2). For example, charge densities below 10^{-10} a.u. (respectively 10^{-4} a.u.) are needed in the vacuum for the rise in the exchange-correlation (respectively electrostatic) potential across the surface to be converged within 0.01 eV.

4.6 Conclusions

We have studied the use of a macroscopic-average method for the calculation of work functions. This technique allows accurate work functions to be determined from thin-slab calculations. We recover very stable charge densities and potentials inside the slab by filtering the atomic oscillations in the electronic density. By relying only on the film charge density to determine the work function, and not on the position of the slab Fermi level, we have shown how quantum-size effects resulting from the confinement of the electronic wave functions in thin slabs can be reduced. The work functions of semi-infinite crystals can then be obtained by studying slabs with a small number of atomic layers.

‘‘Electrons all jumbled like rice?’’
Quoth Einstein, ‘‘That’s too high a price.’’
    In reply, answered God
    ‘‘Well I don’t find it odd.
So shut-up and let me play dice.’’

Bruce Baskir

Chapter 5

Work function anisotropies

IN this chapter, we explore *ab initio* the work function anisotropies of a selection of elemental metals. We study some prototype systems and establish the trends that can be expected in observed anisotropies of clean surfaces. By focusing on the different roles of s, p and d electrons, we bring some insights into the mechanisms controlling the ordering of the work functions of the main surface crystallographic orientations. We successively examine increasingly complex materials, first sodium, a simple metal with a single s valence electron, and then aluminium, where the p-atomic-like character of the density of states at the Fermi energy is shown to play a crucial role in determining the observed anomalous trend of the work functions [105]. Finally, a comparison between copper and gold serves to highlight the effect of the localised d-states on the work function anisotropy.

5.1 Simple s-metals

Alkaline and alkaline-earth metals possess an elementary electronic valence structure with respectively one or two s valence electrons. Their bulk properties are thought to be well understood on the basis of nearly free electron bands [16]. However, for an accurate description of various surface features, such as the work function anisotropy or the surface lattice relaxation, it is necessary to go beyond simple models to fully three-dimensional *ab initio* calculations. We focus here on a prototypical element, sodium, whose electronic structure is $1s^2\ 2s^2\ 2p^6\ 3s$, with one valence electron. Sodium is a body-centered cubic metal and its equilibrium valence bulk band structure and Brillouin zone are shown in Figure 5.1. The unique valence electron half fills the first free-electron-like band, leading to a nearly spherical Fermi surface.

Based on fully relaxed pseudopotential calculations,[1] we have studied the work

---

[1] We employed a Troullier-Martins pseudopotential in the Kleinman-Bylander form. The

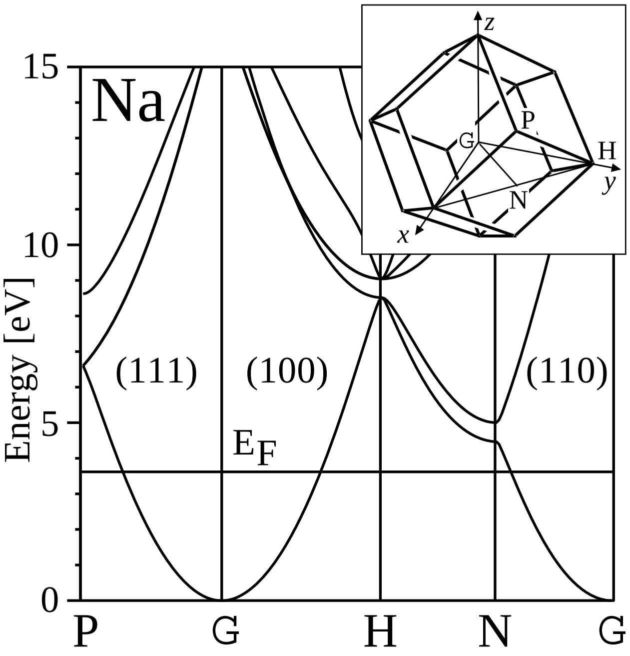

Figure 5.1: Band structure of sodium: a simple body-centered cubic metal with one valence s electron. The energy zero is set at the bottom of the first band. The Fermi energy E_F is shown as a horizontal solid line at 3.65 eV. The inset shows the full Brillouin zone and the points of high symmetry. The parameters used for the bulk calculations are given in the text.

functions of Na for a number of different surface orientations. Previous first-principles studies of Na have focused only on one or two orientations, or have not included the ionic surface relaxation [62, 106, 107]. We have calculated the work functions of Na(110), Na(100) and Na(111), using in each case a suitably oriented supercell and the accurate macroscopic average procedure detailed in Chapter 4 to evaluate the surface-dependent term ΔV. For the Na(110) surface, we used an 8+8 supercell (8 layers of Na, and 8 equivalent layers of vacuum) with 60 reduced k-points. The corresponding values for the Na(100) and Na(111) surfaces were respectively a 8+8 cell with 90 k-points and a 12+12 cell with 105 k-points. The supercell calculations were carried out with a plane-wave cutoff of 16 Ry, and the relaxation was determined by allowing the top three layers of each surface to relax. The bulk calculation for E_F was performed using a cutoff of 36 Ry and 455 reduced k-points.

The theoretical work functions are shown in Table 5.1, for both relaxed and unrelaxed surfaces. The numerical uncertainty on the values of the work functions is estimated to be ~0.03 eV. The (110) surface shows the largest work function (2.98 eV). The other two orientations have similar work functions, nearly 0.2 eV below Na(110). The only available experimental face-dependent work function is for the Na(110) direction (2.9 eV, in reference [39]), and compares favourably with our calculation. A slightly older polycrystalline value sets the work function at 2.4 eV [39].

---

corresponding bulk equilibrium lattice parameter is 7.52 a.u.

Table 5.1: Theoretical values of the sodium work functions calculated with (W^{calc}_{relax}) and without (W^{calc}_{unrel}) surface relaxation, compared with Na(110) and polycrystalline experimental values (W^{exp}), all in eV. Below, the calculated top three interplane surface relaxations (Δd^{calc}) are shown in percent of their respective interplane spacings.

SODIUM

	(110)	(100)	(111)
W^{calc}_{relax}	2.98	2.80	2.79
W^{calc}_{unrel}	2.99	2.80	2.77
W^{exp}	2.9	2.4 (polycrystal)	
Δd^{calc}_{12}	-0.04%	+0.05%	+1.2%
Δd^{calc}_{23}	+0.02%	-0.03%	-20.3%
Δd^{calc}_{34}			+11.8%

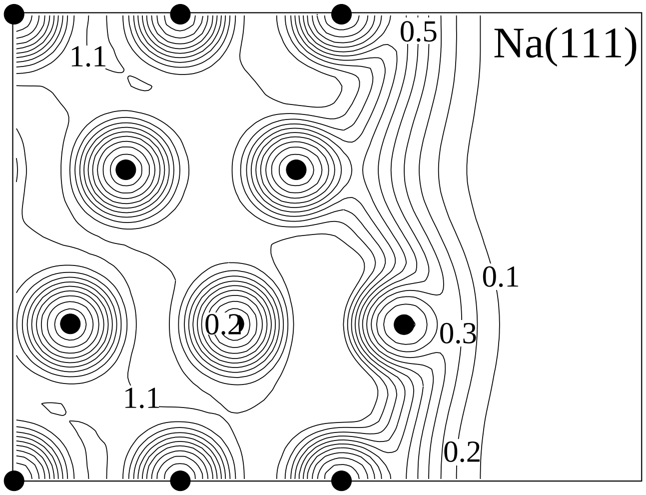

Figure 5.2: Contour plot of the charge density at a relaxed Na(111) surface. The plane shown is a ($\bar{1}10$) plane containing the ions (black disks). The contours are regularly spaced by 0.1 (electrons/unit cell).

Sodium exhibits a standard anisotropy of the work function, which increases with the surface packing density, from the (111) to the (100) and to the (110) orientation, and is consistent with the Smoluchowski rule. An example of surface electronic smoothing is shown in Figure 5.2, where the electronic density in a section of the relaxed Na(111) surface is drawn.[2] The electronic density differs from the bulk within the first few atomic layers, where the charge density contours tend to follow lines parallel to the surface. This results from a redistribution of electronic charge from the top ion to the region within the surface layer, which reduces the work function in accordance with the Smoluchowski smoothing principle.

The calculated surface relaxations (see Table 5.1) are small for the two orientations of highest density, and the work functions are correspondingly unaffected by the relaxations. Despite the lack of recent experimental data for Na surfaces,

---

[2] Since we calculate only the pseudo-charge density, a noticeable non-physical reduction of the density is apparent in the core region of the Na ions.

previous model calculations [108] for Na(100) and Na(110) have predicted negligible ionic relaxations for these orientations (although another study has predicted a slight expansion for Na(110) [106]). The open Na(111) surface shows an extended multilayer relaxation, with an oscillatory relaxation of varying sign. A compilation of experimental data [109] shows that such complex relaxations are often observed on low-density metallic surfaces. Despite the strong relaxation of the Na(111) surface, the work function is practically unchanged by the large displacements of the surface ions. We will discuss this property in more detail in the next section, in connection with the results for Al.

5.2 Anomaly in aluminium

Experimentally, the work function of Al increases in going from the (111) to the (110) and to the (100) surface orientation. This is in contrast with the behaviour observed in other fcc metals such as Ni, Cu or Ag (see Chapter 2) and inconsistent with Smoluchowski's rule. Furthermore, while the atomic surfaces of elemental metals generally show inward relaxation, as predicted by the electrostatic model of Finnis and Heine based on Smoluchowski smoothing, the Al(100) and (111) surfaces relax outwards.

In this section, we explain these anomalous trends, based on our *ab initio* calculations. The electronic structure of aluminium is $1s^2\ 2s^2\ 2p^6\ 3s^2\ 3p$, containing two extra electrons compared with sodium, and leading to a partially filled p-orbital shell. We will show that a microscopic mechanism specific to open p-shell metals can reverse the work-function trend expected from Smoluchowski's rule, and can also explain the anomalous outward surface relaxation.

The calculational procedure for determining the work function anisotropy of aluminium is the same as for Na: we use supercells oriented according to the three surface orientations of highest density, in this case adapted for a fcc metal. The parameters used for Al(111) are an 9+6 supercell (9 layers of Al, and 6 equivalent layers of vacuum) with 36 reduced k-points. The corresponding values for Al(100) and Al(110) are respectively a 8+6 cell with 45 k-points and a 8+8 cell with 48 k-points. We use a Troullier-Martins pseudopotential with a plane-wave cutoff fixed at 16 Ry. The relaxation was studied by allowing the top three layers of each surface to relax. The Fermi energy is obtained by a separate bulk calculation with a cutoff of 36 Ry and 570 reduced k-points.[3]

In Table 5.2, our results for the work functions of the relaxed and unrelaxed surfaces are compared with photoelectric experimental values [42]. The theoretical values agree to within 0.04 eV with experiment and successfully reproduce the

---

[3] With these parameters, the work functions are estimated to be accurate within ~0.03 eV.

Table 5.2: Theoretical values of the aluminium work function, in eV, for the three principal surface orientations, as obtained with (W^{calc}_{relax}) and without (W^{calc}_{unrel}) surface relaxation. The theoretical values are compared with the experimental data (W^{exp}) of Ref. [42]. Below, the top three interplane surface relaxations (Δd^{calc}), in percent, are compared with the experimental data (Δd^{exp}) of Ref. [110–112] for the (111), (100), and (110) surfaces respectively.

ALUMINIUM

	(111)	(100)	(110)
W^{calc}_{relax}	4.25	4.38	4.30
W^{calc}_{unrel}	4.23	4.42	4.29
W^{exp}	4.24 ±0.03	4.41 ±0.02	4.28 ±0.02
Δd^{calc}_{12}	+0.8	+0.9	-8.5
Δd^{calc}_{23}	+0.5	+0.4	+4.8
Δd^{calc}_{34}			-2.0
Δd^{exp}_{12}	+1.7 ±0.3	+1.8	-8.6 ±0.8
Δd^{exp}_{23}	+0.5 ±0.7		+5.0 ±1.1
Δd^{exp}_{34}			-1.6 ±1.2

anomalous (111)→(110)→(100) surface ordering. Once again, the effect of the surface multilayer relaxations on the work functions is shown to be negligible for all orientations, when compared with the numerical accuracy.

For the relaxed surfaces, the variations of the top interplane distances are displayed in Table 5.2 and are compared with experimental Low-Energy Electron Diffraction (LEED) data [110–112]. The small outward relaxations of the Al(111) and Al(100) surfaces are well reproduced, as well as the damped oscillatory behaviour of the Al(110) multilayer relaxations. Finnis and Heine's electrostatic model [33] predicts inward relaxations of the top layers which increase when the atomic packing of the surface decreases (see Section 2.3.1). Although outward relaxations are found for the Al(100) and Al(111) surfaces, the strong contraction of the (110) surface layer is in qualitative agreement with this model (which predicts a contraction of -16% for the (110) top interlayer distance).

The large ionic relaxation for Al(110) leads to severe modifications of the electrostatic potential within the first few atomic layers. Figure 5.3 shows the relaxed and unrelaxed macroscopic charge densities and potentials. Since we have allowed the top three planes to relax to their equilibrium positions, the macroscopic ionic charge can be locally above or below its bulk value of 3 electrons per ion. This leads to a variation in the bulk ionic macroscopic charge, and a significant change in the macroscopic potential near the surface, as shown in the lower panel of Figure 5.3.

The effect of the surface multilayer relaxations on the work function of Al

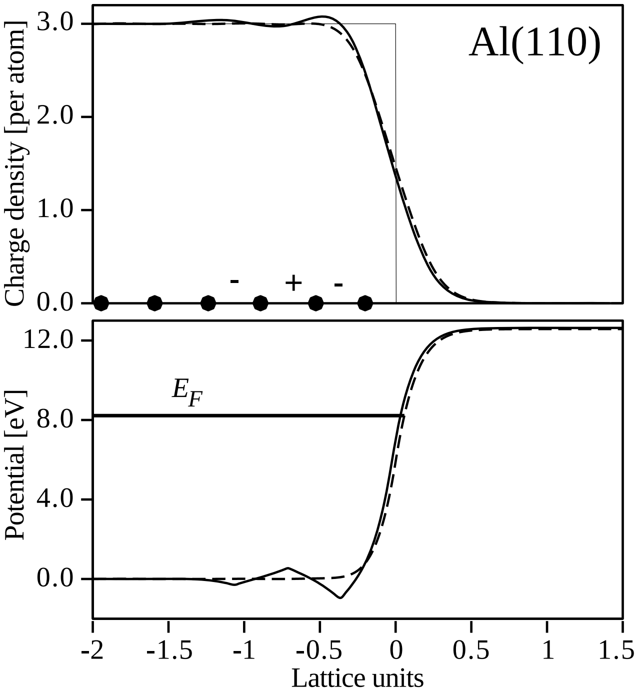

Figure 5.3: Al(110) surface. Upper panel: Macroscopic electronic charge density for an unrelaxed (dashed line) and a relaxed surface (solid line), together with the unrelaxed ionic charge density (thin solid line). The relaxed ionic planes are also shown (black disks), with the variations in the interplane spacings represented as +/- symbols. Lower panel: Corresponding total macroscopic electrostatic potential for the unrelaxed (dashed line) and relaxed (solid line) surfaces. The electrostatic potentials have been aligned at the centre of the metal slab, and E_F shows the corresponding bulk Fermi energy.

is however shown to be negligible, when compared with the numerical accuracy. The variation in work function induced by the ionic relaxation is controlled by the surface dynamical effective charges, which measure the electrostatic dipole induced by a unit displacement of the ions. Our calculations for Al and Na suggest that the effective charges of the ions in the surface layers are nearly zero, *i.e.* similar to the value in the bulk metal, where the perfect electronic screening leads to vanishing effective charges. This observation is consistent with the sum rule recently derived for effective charges at crystal surfaces [113].

5.2.1 Models of surface charge

Having shown that surface relaxations produce negligible modifications of the work functions, our discussion and interpretations of the work function trend of Al are focused on unrelaxed surfaces. In order to model the surface electronic charge density, the crystal surface may be approximated, as a first step, by a superposition of atomic charge densities or of bulk Wigner-Seitz unit cells. In both these cases, the charge density $n(\mathbf{r})$ of the crystal may be written as a sum of globally-neutral density distributions $\rho(\mathbf{r} - \mathbf{R})$, associated with each lattice

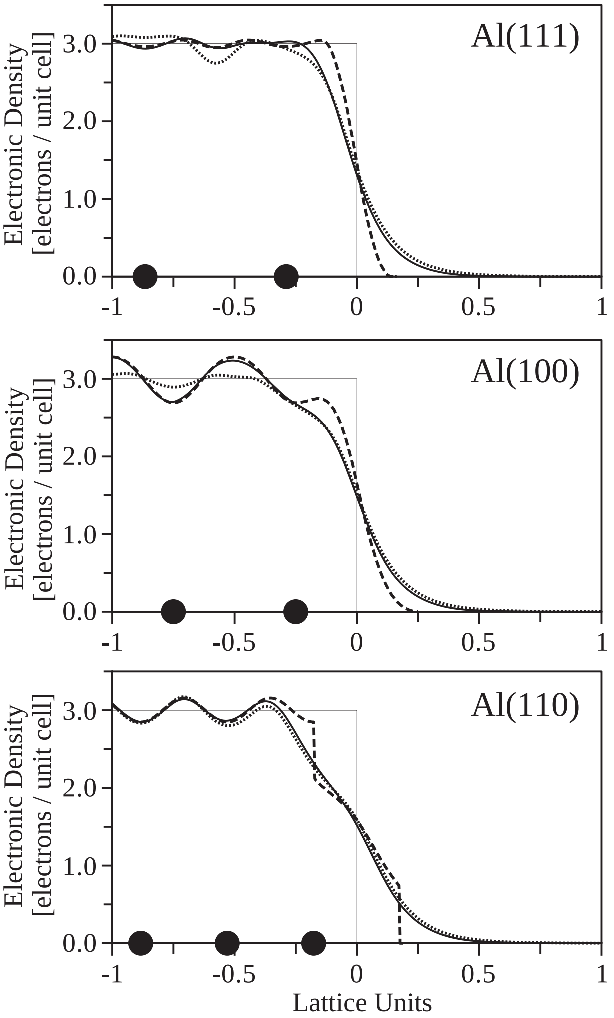

Figure 5.4: Planar average of the electronic charge density for unrelaxed Al(111), Al(100) and Al(110), as a function of the distance to the surface. Solid line: self-consistent charge density, dashed line: surface formed by repeating the charge density of bulk Wigner-Seitz unit cells, dotted line: superposition of atomic charge densities. The rectangle gives the macroscopic average of the ionic charge density. The black disks indicate the positions of the atomic planes.

vector $\mathbf{R}$, and carrying by symmetry no dipole or quadrupole moment [25]:

$$n(\mathbf{r}) = \sum_{\mathbf{R}} \rho(\mathbf{r} - \mathbf{R}). \tag{5.1}$$

The electrostatic potential $V(\mathbf{r})$ is then similarly written as a sum of contributions from each lattice node:

$$V(\mathbf{r}) = \sum_{\mathbf{R}} v(\mathbf{r} - \mathbf{R}), \tag{5.2}$$

where $v(\mathbf{r})$ is the potential created by $\rho(\mathbf{r})$, with a reference energy chosen so that $v(r \to \infty) \to 0$. The potential in the vacuum is then zero far from the metal surface, while inside the metal, the average potential $\overline{V}$ over a unit cell Ω is given by:

$$\overline{V} = \frac{1}{\Omega} \int_{\mathbf{r}\in\Omega} \mathbf{dr} \sum_{\mathbf{R}} v(\mathbf{r} - \mathbf{R}) = \frac{1}{\Omega} \sum_{\mathbf{R}} \int_{\mathbf{r}'+\mathbf{R}\in\Omega} \mathbf{dr}'\, v(\mathbf{r}') = \frac{1}{\Omega} \int \mathbf{dr}\, v(\mathbf{r}). \tag{5.3}$$

Clearly, $\overline{V}$ is independent of the surface orientation, since it is a bulk quantity. The superpositions of atomic charges or of bulk Wigner-Seitz unit cells do not induce any orientation dependence in the work function. They could therefore be taken as convenient reference electron surface distributions.

However, for Al these models lead to unrealistic values of the work function. In Figure 5.4, we have plotted the self-consistent electronic charge density of the Al(111), (100) and (110) surfaces and compared them with the superposition of atomic charges as well as with the surfaces built from bulk Wigner-Seitz unit cells. As for most metals, the atomic charges model heavily overestimates the work functions [114], yielding W_{at}=7.59 eV, to be compared with the self-consistent results W_{111}=4.23 eV, W_{100}=4.42 eV, and W_{110}=4.29 eV, whereas the Wigner-Seitz model strongly underestimates them with a value of W_{WS}=0.33 eV. The self-consistent charge is seen to follow closely the Wigner-Seitz density inside the crystal, but to approach the atomic distribution in the vacuum region. Around the surface ions, the contracted wave functions of the bulk crystal tend to relax back to their atomic dimension in the direction perpendicular to the surface, and the related charge transfer increases the surface dipole. In the surface plane, we note that the self-consistent charge density is larger than the bulk density for Al(111), comparable to the bulk density for Al(100) and clearly below the bulk value for Al(110).

5.2.2 Importance of p-states

In the case of an open p-shell metal such as Al, the existence of an important asymmetry between the directional p-orbitals of the surface ions must be accounted for. The $p_{\parallel}$-states, parallel to the surface, can be expected to be occupied

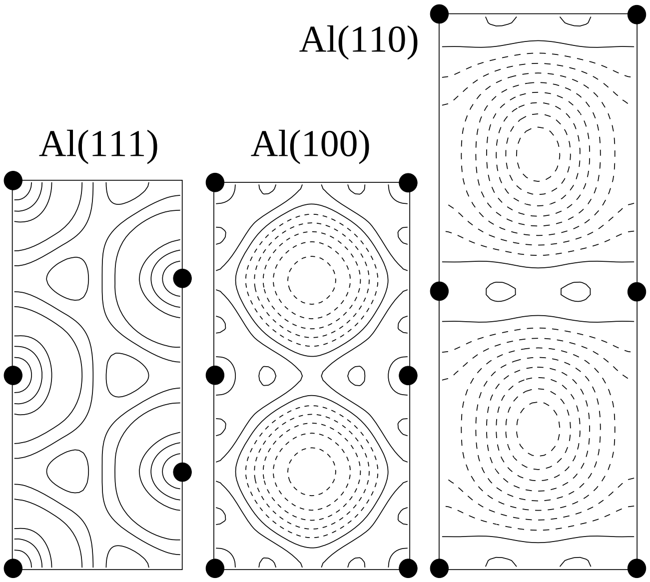

Figure 5.5: Contour plots of the electronic charge density difference between the exact self-consistent charge in the aluminium surface plane and the corresponding plane in a bulk Al crystal. The contours are equally spaced (by 0.02, 0.05 and 0.2 [e$^-$/unit cell] for the (111), (100) and (110) orientations respectively). Dashed lines correspond to negative values and black disks to the positions of the ions.

differently from the $p_\perp$-states, perpendicular to it. The $p_\parallel$-states are energetically favourable, when compared to the $p_\perp$-orbital that extends into the vacuum and regions of higher potential. In Figure 5.5, we have plotted the difference between the electronic density in the surface plane of Al and the density in a corresponding bulk plane. Despite the supplementary freedom allowed by the possible spreading of the valence electrons into the vacuum, the surface plane in the Al(111) direction shows an all-over increase in density with respect to the bulk situation. In the Al(100) and Al(110) directions, the density is similarly increased along the bonds between nearest-neighbours. Compared with the bulk situation, this extra density in the $p_\parallel$-states, which increases with higher atomic packing of the surface, results in a lower occupation of the $p_\perp$-orbitals and tends to decrease the work function.

This view is supported by the following numerical experiment, in which we have sought to modify the number of valence electrons associated with each Al ion. We have defined a series of virtual atoms Al_Z, with varying valence Z, by using pseudopotentials linearly scaled from that of aluminium. Since Al has three valence electrons, to retain charge neutrality Al_Z is associated with $Z = 3\lambda$ electrons, where λ is the pseudopotential scaling factor. We then computed self-consistently the work functions of the corresponding Al_Z crystals, *i.e.* a series of crystals composed of Al_Z pseudo-atoms on an Al fcc lattice.[4] The results for the three principal directions are plotted in Figure 5.6 as a function of the number of electrons per ion (and of λ). It is seen that for low values of the density, the ordering of the work functions follows the Smoluchowski prediction and increases

---

[4] The virtual crystal calculations are performed at the theoretical lattice constant of aluminium: $a = 7.51$ a.u. The cutoff is increased to 25 Ry for $\lambda > 1.5$.

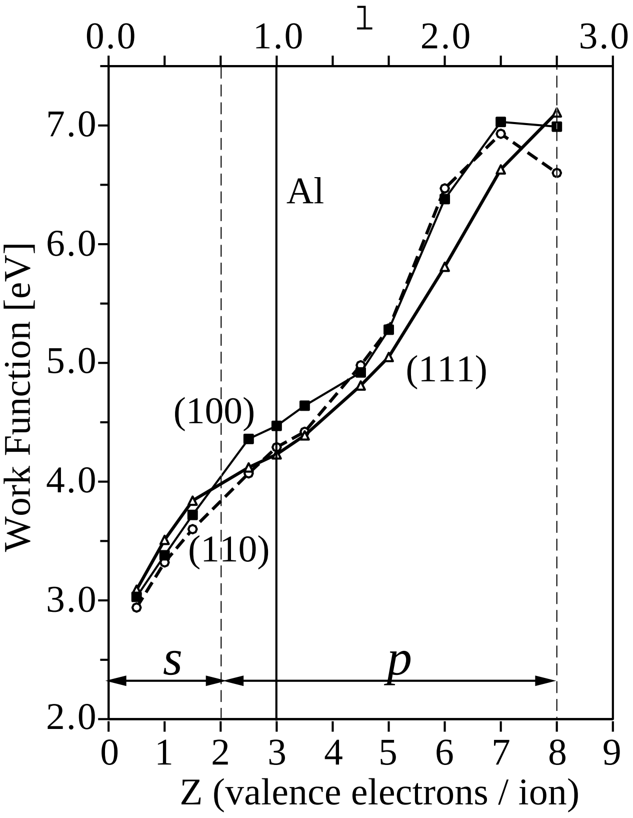

Figure 5.6: Work functions of the virtual Al_Z crystals for the three principal surface orientations, as a function of the valence charge Z (lower axis) and the Al pseudopotential scaling factor λ (upper axis), as detailed in the text: (111): triangles, (100): squares, (110): circles. The solid vertical line shows the position of the real Al crystal. Vertical dashed lines delimit the filling of different orbital states.

from (110) to (100) and to (111). However, as the number of valence electrons per ion is increased above two, the trend of the (111) surface changes and it crosses below the other directions. As the density rises further, a number of other crossings are observed.

As shown in Figure 5.6, the Smoluchowski rule correctly describes the Al work function anisotropy when the only occupied levels around each ion are *s*-states. Figure 5.7 shows the bulk band structures of Al and $\mathrm{Al}_{1.5}$ along the three directions of interest. We observe that below the Fermi level of Al the band structure depends weakly on the value of the electronic density. As λ changes, only the position of the Fermi level is modified significantly to accommodate the different number of electrons in the crystal. For low values of the electronic density, in the Smoluchowski regime of the work function, the Fermi level is positioned on the nearly parabolic isotropic *s*-band. The first sign of a change in the trend of the work function occurs for the Al(111) face when the states at the bottom of the *p*-band begin to be filled, near the Bragg plane at the edge of the Brillouin zone in the (111) direction. The electronic wave functions of the surface are indeed expected to derive from Al bulk states with similar energies in the semi-infinite system. As the electronic density increases the anisotropic *p*-bands are increasingly filled and the work function becomes highly anisotropic.

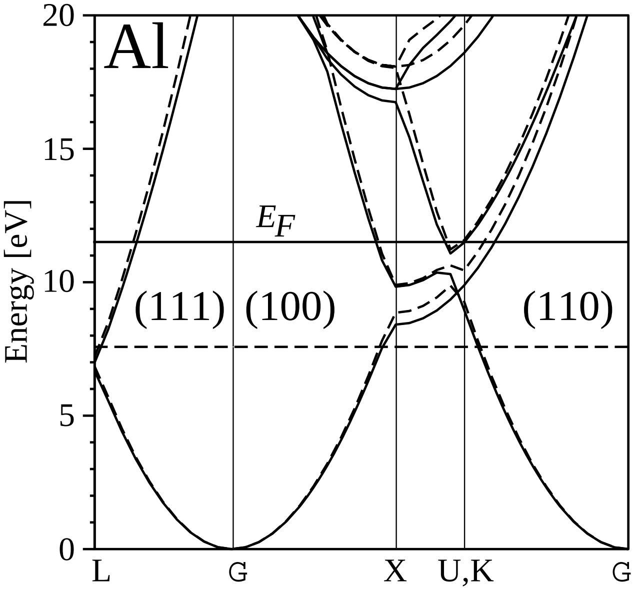

Figure 5.7: The band structure of Al (continuous lines) and of $Al_{1.5}$ (dashed lines), along selected directions in the Brillouin zone. The energy zero is set at the band minimum in both cases. The Fermi level E_F is situated at 11.43 eV in Al (horizontal solid line) and at 7.47 eV in $Al_{1.5}$ (horizontal dashed line).

We thus suggest that it is the face-dependent filling of the p-states at the surface that is responsible for the work function anisotropy in Al. The occupation of the $p_{\|}$-states is affected by the position of the ionic neighbours, and hence by the surface orientation. A modification of the number of valence electrons in $p_{\|}$-states induces a change in the filling of the $p_{\perp}$-states and therefore of the surface dipole. The (111) surface has the highest number of nearest-neighbours in the surface plane and the $p_{\|}$-states are highly favoured. This results in fewer electrons in the $p_{\perp}$-orbitals and leads to a lower surface dipole compared to other orientations. The Al(111) work function therefore dips below the other two orientations at an early stage when the electronic density is artificially raised. The second most dense surface is (100) and, as seen in Figure 5.6, it is the second direction to dip below the (110) direction when the p-states are filled. The (110) direction then exhibits the largest work function. At this point Smoluchowski's ordering has been reversed. When the p-states are nearly completely occupied, the work functions show further crossings, in reverse order to which they first appeared. For 8 electrons per ion, the p-states are fully occupied and the contribution of the p-orbital filling to the anisotropy disappears. The work functions are then seen to be ordered similarly to the low-density situation.

The anomalous outward relaxation of the Al(111) and Al(100) top layers can be similarly understood in terms of the weakening/strengthening of the $p_{\perp}/p_{\|}$ surface orbitals resulting from their different occupation with respect to the bulk situation. We have examined the surface relaxation of an $Al_{1.5}$ crystal, which contains no filled p-bands, and the anomalous outward relaxations are found to disappear in this case. Moreover, for Al_8, in which the p-bands are completely

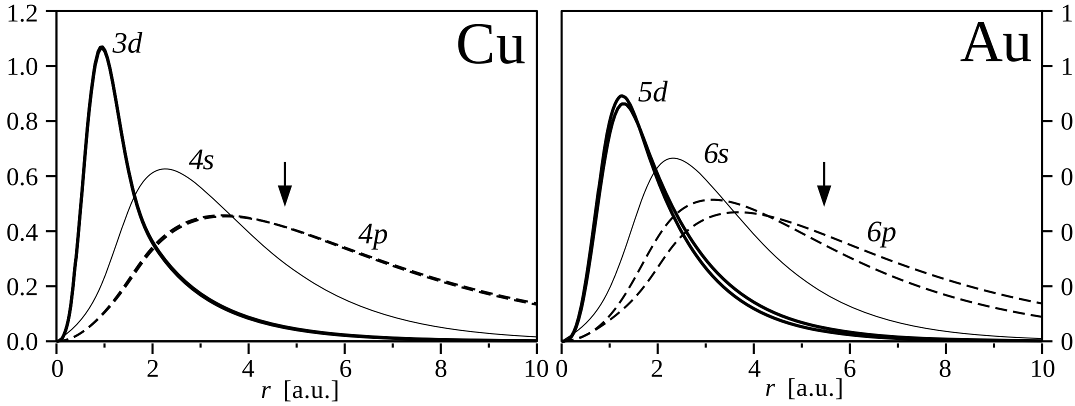

Figure 5.8: Atomic pseudo-wave functions in copper and gold, multiplied by the radial distance r, calculated with Troullier-Martins pseudopotentials. The localised fully-occupied d-orbitals (thick solid lines), partially occupied valence s-orbitals (thin solid lines), and unoccupied p-orbitals (dashed lines) are apparent. The theoretical bulk nearest-neighbour distances of 4.74 and 5.46 a.u., in Cu and Au respectively, are indicated by vertical arrows.

filled, the (100) and (111) surfaces show standard inward relaxation.[5]

In this light, the ordering of the work functions and the surface relaxations in Al are seen to arise from the interplay of two trends. At low electron densities, Smoluchowski smoothing is seen to describe correctly the surface trends. When p-bands are filled, the trends change and depend on the exact number of valence electrons per ion. The exceptional nature of Al among fcc metals thus results from its Fermi level positioned among p-bands.

5.3 Contributions from d-states in noble metals

5.3.1 Unreconstructed surfaces

Isolated atoms of noble metals, such as copper, silver, and gold, contain a spatially-localised filled shell of d-orbitals that are close in energy to a singly-occupied s-orbital. Early studies noticed that both these orbital states participate in bonding mechanisms [115] and should be included in the valence states. In this section, we examine the contributions of the d-states to the work function anisotropies of copper and gold, by means of *ab-initio* calculations of relaxed and unrelaxed low-index surfaces. We present increasingly accurate theoretical descriptions of Cu and Au crystals, progressively accounting for the full contribution of the d-states.

---

[5] The relaxations at the surfaces of the virtual crystals are determined at their respective theoretical lattice constants.

The electronic structures of noble metals in the atomic state contain d-orbitals that are entirely filled with 10 electrons, leading for example to: Cu: [Ar] $3d^{10}$ $4s^1$ and Au: [Xe] $5d^{10}$ $6s^1$. The atomic valence orbitals for these two elements are shown in Figure 5.8. The d-orbitals are seen to be mostly localised within 2 a.u. of the ion centres, well below the bulk theoretical nearest-neighbour distances. As a first approximation, we neglect the effect of the semi-core d electrons and treat the d-orbitals as core states in our pseudopotential calculations for the copper and gold surfaces. We thus iterate a metallic slab to self-consistency with a single electron per atom to obtain the electrostatic potential step at the surface.[6] The resulting work-function anisotropies of Cu and Au with only one valence electron (W^s) (calculated from Equation 4.5) are shown in Table 5.3 for unrelaxed surfaces. In this approximation, the ordering of the surfaces for both metals follows the Smoluchowski rule of increasing work function with the surface packing density, from (110) to (100) and to (111).

The effect of the d-electrons in Cu and Au can be partially accounted for, in the crystalline state, by including the frozen atomic charge of the d-orbitals in the evaluation of the crystalline exchange-correlation potential. This so-called non-local core correction (CC) [119] provides an improved description of the metal, while retaining the simplicity of a single valence electron per atom. The calculated work function anisotropies W^s_{CC} are shown in Table 5.3, with the differences $W^s_{CC} - W^s$ indicated in italics.

The core correction is seen to reduce the work functions of all Cu and Au surfaces. The global reduction in work function can be understood in terms of a bulk effect resulting from an enhanced electron-ion bonding. The on-site s-d overlap creates a supplementary exchange-correlation potential that bonds the electrons more strongly to the ions. We attribute the orientation-dependence of the work function change to the varying interaction between the s-orbitals of the surface atoms and the d-orbitals of neighbouring atoms. Orientations where the surface atoms possess a larger number of nearest neighbours are then expected to show increased bonding of the valence electron and a corresponding greater reduction in the surface dipole. Indeed, the work function is most strongly reduced by the core correction on the close-packed Cu(111) and Au(111) surfaces. This trend is opposite to the Smoluchowski ordering but its effect is not large enough to clearly reverse the W^s_{CC} work function anisotropy. In Au, where the d-orbitals are more extended, the core-corrected work functions W^s_{CC} of Au(100) and Au(110)

---

[6] The successive approximations to Cu and Au are performed at the theoretical lattice constants of copper and gold (respectively 6.68 and 7.72 a.u.). We use Troullier-Martins pseudopotentials and a plane-wave kinetic energy cutoff of 36 Ry for Cu with one valence electron (25 Ry for Au). We use similar supercells and sets of k-points as for the Al surfaces studied in Section 5.2.

Table 5.3: Theoretical values of the copper and gold work functions of unreconstructed relaxed (W^{calc}_{relax}) and unrelaxed (W^{calc}_{unrel}) surfaces, compared with the unrelaxed s-electron contribution with (W$^{s}_{CC}$) and without (W^{s}) the non-local core correction. Differences between consecutive lines are offset in italics. For copper, two experimental measurements obtained by photoemission [116] (W^{exp}_{PE}) and ARUPS [2] (W^{exp}_{ARUPS}) are included. For gold, three experimental measurements on reconstructed surfaces, obtained by PE/CPD [117] (W^{exp}_{PE}) and ARUPS [2, 118] (W^{exp}_{ARUPS}) are shown. All values in eV.

COPPER

	(111)	(100)	(110)
W^{calc}_{relax}	5.31	5.02	4.81
W^{calc}_{unrel}	5.32	5.05	4.83
	-0.16	*-0.18*	*-0.26*
W^{s}_{CC}	5.49	5.23	5.09
	-1.72	*-1.52*	*-1.37*
W^{s}	7.21	6.75	6.46
W^{exp}_{PE}	4.94±0.03	4.59±0.03	4.48±0.03
W^{exp}_{ARUPS}	4.93±0.03	4.63±0.03	

GOLD

	(111)	(100)	(110)
W^{calc}_{unrel}	5.63	5.53	5.41
	-1.07	*-0.75*	*-0.88*
W^{s}_{CC}	6.70	6.28	6.29
	-2.01	*-1.87*	*-1.66*
W^{s}	8.71	8.15	7.95
W^{exp}_{PE}	5.30±0.05		5.12±0.07
W^{exp}_{ARUPS}	5.26±0.04	5.22±0.04	5.20±0.04
W^{exp}_{ARUPS}	5.55±0.03		

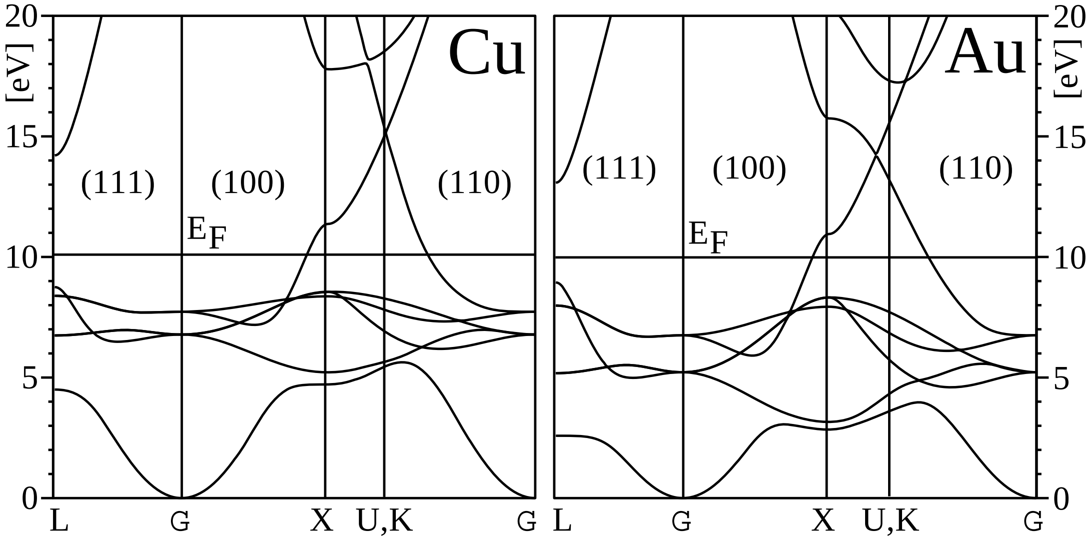

Figure 5.9: Bulk band structures of copper and gold, two noble face-centered cubic metals. The energy zero is positioned at the bottom of the first valence band. The Fermi energy E_F is shown in each case as a horizontal solid line: at 10.10 eV in Cu, and at 9.99 eV in Au.

are much closer than if the core-correction is omitted (W^s).

In order to account fully for the effect of the d electrons, they must be treated as valence orbitals, *i.e.* 11 valence electrons per ion must be included in the pseudopotentials of Cu and Au.[7] In the solid state, this leads to a hybridisation between s- and d-states, as seen in the bulk band structures of Figure 5.9. The d-states form a band localised in energy, slightly below the Fermi level, and mixed with the s-states. At noble metal surfaces, the d-band is narrower than in the bulk and its centre of gravity is slightly shifted to higher energies. In a tight-binding picture, the narrowing results from a reduced number of nearest neighbours for atoms at the surface. The shift in energy of the d-band follows the increase in potential near the metal surface. In the LDOS of a Cu(110) surface, shown in Figure 5.10, the d-band in the top layer is seen to peak at higher energies than deep inside the metal slab. It has been recognised that, as a consequence of the s-d mixing, the occupation number of the d band, in Cu and Au bulk crystals [8, 120], is below the 10 electrons characteristic of the atomic state. Approximately 1.5 non-d electronic states per atom are filled in the solid state, which proves crucial, as we will see, to understanding the work function anisotropy trends.

The work functions W^{calc}_{unrel} of unrelaxed surfaces, obtained by treating the d-states as valence orbitals, and the corresponding differences $W^{calc}_{unrel} - W^s_{CC}$, are

---

[7] The cutoff is increased to 70 Ry for Cu (40 Ry for Au) to describe the localised d-electrons in the full calculation.

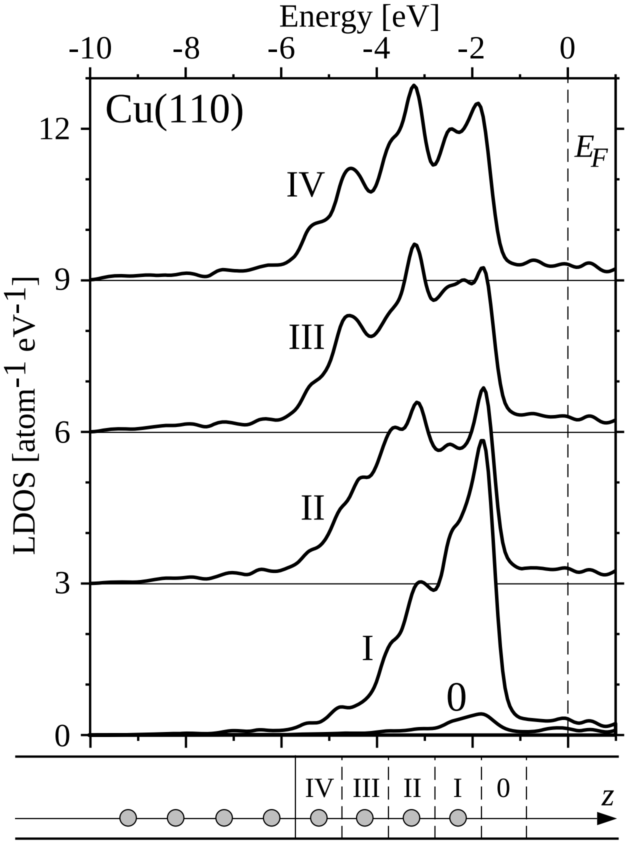

Figure 5.10: Local density of states in a Cu(110) slab, per eV and per atom. Curves 0 to IV exhibit the LDOS of layers increasingly deep in the metal and have been calculated in the corresponding regions 0 to IV shown in the inset at the bottom, where grey circles indicate the atomic planes. Curves II to IV have been shifted vertically for clarity. The energy zero is set at the Fermi energy E_F.

also shown in Table 5.3. The $W^{calc}_{unrel} - W^{s}_{CC}$ differences result from a combination of two effects—attributed respectively to the s- and d-states—that act oppositely on the work function anisotropy. Firstly, as a consequence of the hybridisation, a supplementary $\sim$0.5 s-electron per atom is present in the exact calculation. This extra electron contributes to an increased Smoluchowski smoothing that tends to decrease the work function. The electronic smoothing forms a reverse dipole that is most intense on the loosely-packed orientations. Indeed, in Cu, we see that the difference $W^{calc}_{unrel} - W^{s}_{CC}$ is always negative and increases in magnitude from the (111) to the (100) and to the (110) surface, following the Smoluchowski ordering. Secondly, since the d-states are not completely filled, they may contribute to the work function anisotropy in a manner similar to the partially-occupied p-states in Al. By analogy with our observations in Al, the redistribution of the electrons among the d-states of the surface atoms should favour states within the surface layer and reduce the filling of those pointing to regions of higher potential outside the metal. This effect is expected to reduce the work function most strongly on the surfaces of highest density. Furthermore, this contribution is expected to increase with the spatial extent of the atomic-like d-orbitals, since they will then sample the potential over a wider area. In Au, where the d-orbitals are

Table 5.4: Surface relaxations of copper surfaces: the variations in the top two interplane distances (Δd^{calc}), in percent, are compared with experimental data (Δd^{exp}) of Ref. [121–123] for the (111), (100), and (110) surfaces respectively.

COPPER

	(111)	(100)	(110)
Δd_{12}^{calc}	-0.5	-3.4	-10.2
Δd_{23}^{calc}	+0.3	+0.8	+3.8
Δd_{12}^{exp}	-0.7±0.5	-2.1±0.2	-10.0±1.0
Δd_{23}^{exp}		+0.5±0.2	+1.9±1.0

more extended, we note that the differences $W_{unrel}^{calc} - W_{CC}^{s}$ are much larger than in Cu. The close-packed Au(111) surface shows the greatest reduction in work function, as would be expected from this contribution alone. We also observe that the final work function anisotropy of Au is smaller than for Cu, in view of the greater contribution of the *d*-states. However, the separation of the change in work function into two distinct *s*- and *d*-terms is largely conceptual and non-linear effects could be present, particularly in Au, where the work function change is strong.

We have relaxed the top two interlayer distances of the principal Cu surfaces (see Table 5.4) and calculated the corresponding work functions W_{relax}^{calc}, which are shown in Table 5.3. The theoretical relaxations follow the experimental trend of inward relaxation for all Cu top layers. As for aluminium surfaces, the relaxation negligibly changes the work function. We may now compare the results of our full calculations with experimental data shown in Table 5.3. In Cu, the theoretical work function anisotropy correctly follows the experimental trend, even if our calculations overestimate the PE and ARUPS data by ~0.4 eV.[8] Contrary to copper surfaces that are generally unreconstructed experimentally, the low-index orientations of gold usually show complex reconstructions. The top layer of the Au(111) surface shows a $[(22 \pm 1) \times \sqrt{3}]$ surface unit cell of higher density than the underlying planes [125, 126]. The ground state of the Au(100) surface is formed by a close-packed rotated hexagonal monolayer on top of the bulk square lattice, with a proposed superlattice periodicity of (28×5) [127]. Au(110) surfaces are known to form (1×2) missing-row reconstructions in the surface plane, with a doubling of the unit cell perpendicular to the furrows [128, 129]. A comparison between the theoretical work functions of Au and experimental data must therefore be made cautiously. Nevertheless, the ordering of the theoretical work functions is also reproduced in Au.

---

[8] This difference with the experimental work functions can be tentatively ascribed to the pseudopotential. Test calculations of Cu surfaces using a different (ultrasoft) pseudopotential [124] have shown work functions that are lower by up to 0.2 eV than the results presented here.

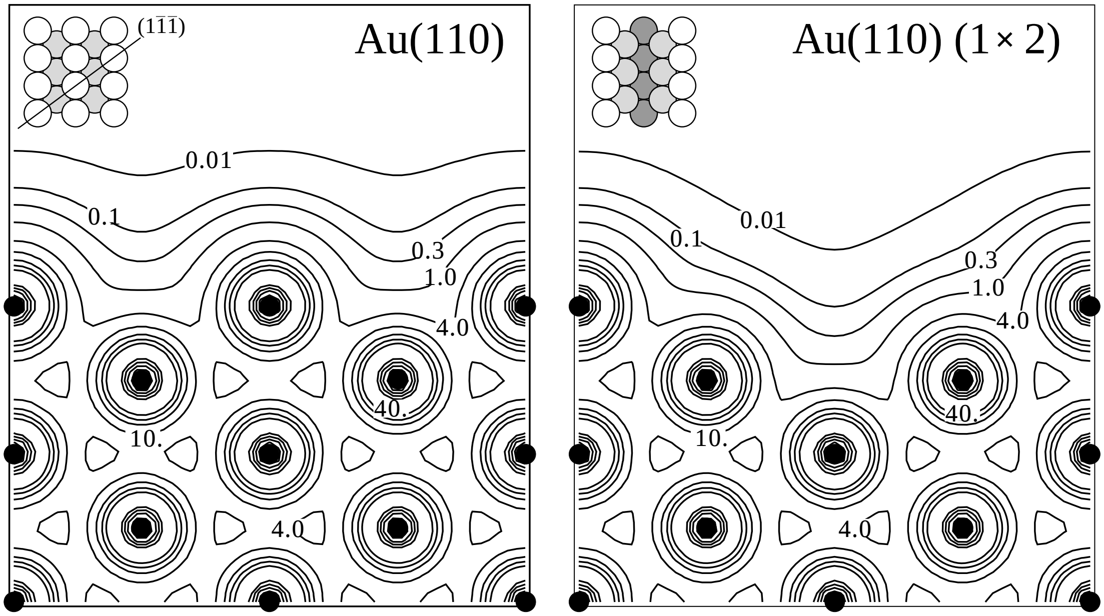

Figure 5.11: Contours of equal electronic charge density at an unrelaxed Au(110) surface (left panel) and at an unrelaxed reconstructed Au(110) (1 × 2) missing-row surface (right panel), shown cut through a (1 $\overline{1}$ $\overline{1}$) plane, not perpendicular to the missing rows, but containing the surface and second-layer atoms (black disks). The contours are indexed in electrons per unit cell and are drawn at the same densities in both panels. The insets show top-down views, with atoms deeper below the surface shown darker.

5.3.2 Influence of surface reconstruction

The Au(110) (1 × 2) missing-row surface is the only reconstructed Au surface amenable to *ab initio* computations. We have calculated its work function using a unrelaxed slab containing 8 filled planes with half-filled layers on either side, for a total of 18 Au atoms per supercell. The self-consistent electronic density is compared with the unreconstructed surface density in Figure 5.11. The theoretical work function of the reconstructed surface is 5.38 eV, very close to the unreconstructed value of 5.41 eV (compared with our numerical accuracy), even though the surface charge densities appear very different in the two panels of Figure 5.11.

The similarity of the work functions of the reconstructed and unreconstructed Au(110) surfaces can be understood by considering rearrangements of the charge density of the unreconstructed surface that yield rigorously identical work functions. In Figure 5.12, the total charge density in a supercell is conceptually separated into three regions. Regions A and B are parallel slabs situated on either side of a [1$\overline{1}$0] row of surface atoms and extending up to the neighbouring ions in the second surface layer. Region C is a Wigner-Seitz unit cell centered around a bulk

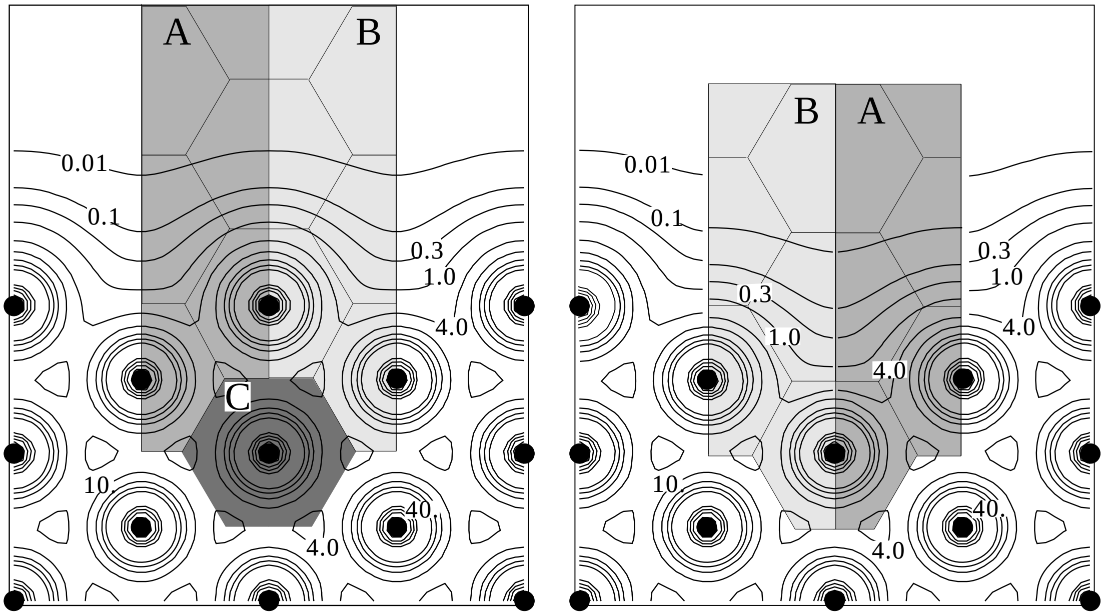

Figure 5.12: Left panel: The charge density at an unrelaxed Au(110) surface is partitioned into regions A/B (light grey areas), on either side of a surface atom, and C, a Wigner-Seitz unit cell around a bulk atom (dark grey area). Right panel: By removing region C and translating regions A and B, an approximation of the charge density at the Au(110) (1×2) missing-row surface is obtained. Both panels are shown cut through a $(1\ \overline{1}\ \overline{1})$ plane. The contours are indexed in electrons per unit cell and are drawn at the same densities in both panels.

atom deep in the crystal below the $[1\overline{1}0]$ row, containing by symmetry no total charge or dipole. By removing region C and translating regions A and B to fill the gap, the work function of the surface is unchanged since the macroscopic surface dipole of the unreconstructed surface D_{110} is conserved. In this way, the exact ionic density of the *reconstructed* missing-row surface is recovered. Furthermore, by observing the contours of equal electronic charge density, we note that this rearrangement of charge provides an approximation of the exact electronic Au(110) (1×2) charge density. The real electronic density only differs from the model above the atoms at the centres of the (111)-like microfacets, where it accounts for the slight change in work function.

The Au(110) (1×2) missing-row surface differs from other reconstructions in that the work function is generally expected to change with the surface reconstruction. As a comparison, we have performed calculations of hypothetical missing-row reconstructions of Au(111) and Au(100) surfaces, where the work function is observed to diminish (by -0.27 and -0.10 eV respectively). In these two cases, by rearranging the unreconstructed charge density, in a similar fashion to Figure 5.12, we cannot recover the reconstructed electronic charge since the missing rows introduce deep furrows into an otherwise smooth surface. The reduction in work function of the hypothetical reconstructed surfaces can then be attributed to strong reverse dipoles induced by Smoluchowski smoothing in the newly-created furrows.

5.4 Conclusions

In this chapter, we have performed self-consistent *ab initio* calculations of infinitely-extended surfaces of several typical elemental metals. We have studied successively sodium, aluminium, copper and gold, where we have reproduced the experimental trends of the work function anisotropies and of the surface relaxations. In each case, we have studied the physical mechanisms that determine the work-function ordering of the main crystallographic orientations.

We have seen that the filled states near the Fermi energy control the surface properties of metals since they extend furthest into the vacuum. They give rise to large surface dipoles which sensitively affect the work function. When the bands around the Fermi energy have a dominant s-character, the clean metal surfaces show a standard work function anisotropy that follows the Smoluchowski rule. The work function of sodium, a bcc metal with a single s valence electron, typifies this behaviour and correspondingly increases from the (111) to the (100) and to the (110) surface.

We have explained the aluminium work function anomaly by means of a microscopic approach. The anisotropy trend of the work function in Al can be explained by a charge transfer for the surface ions from the atomic-like p-orbitals perpendicular to the surface plane to those parallel to the surface, when compared to the orbital occupation numbers of the ions in the bulk. The anomalous outward relaxation of the Al(100) and Al(111) top layers can similarly be understood in terms of a charge transfer among surface p-orbitals. The exceptional nature of the Al work function and the Al surface atomic relaxation, when compared to other fcc metals, results from a dominant p-atomic-like character of the density of states near the Fermi energy. Most elemental metals with a larger valence Z than Al tend to lose their cubic structure, as seen in the periodic table of Figure 2.11, and the work function is then also influenced by the macroscopic anisotropy of the crystal structure.

In noble fcc metals such as Cu or Au, the localised d-orbitals, positioned slightly below the Fermi energy, do not contribute as strongly as the s-electrons to the work function anisotropy. However, the hybridisation between the s- and d-orbitals influences the number of filled states of both types, leading to complex charge rearrangements on the surface atoms that induce changes in the work function that can be opposite to the Smoluchowski rule, as seen most clearly in unreconstructed Au surfaces. The modifications in occupation numbers of the various orbitals on the surface atoms, as well as the possible surface reconstructions, must therefore be taken into account to recover experimental work function trends accurately.

Maxwell had plenty of time to think
While dipping his pen in the ink.
    Today’s computations
    With Maxwell’s equations
Don’t leave you the time for a wink.

Amikam Aharoni

Chapter 6

Work functions at facet edges

6.1 Introduction

MOST clean metal surfaces have work functions that range from 3 to 5 eV, while the work function difference between two inequivalent surface orientations of the same metal can be between 0.1 and 0.8 eV. The anisotropic fraction thus represents a substantial proportion of the total work function. This leads to an interesting theoretical problem, namely, the calculation of the electrostatic potential and the local work function outside a finite crystal, particularly if non-equivalent facets are exposed to the vacuum. At large distances from a finite crystal, the crystalline anisotropy is negligible and the electrostatic potential is clearly isotropic. Closer to the crystal, the electrostatic potential varies from one facet to another, in accordance with the work function anisotropy. Indeed, just outside a neutral crystal of finite dimensions, the electrostatic potential is fixed by the work function of the adjacent facet (see Chapter 2). When the work function differs between two neighbouring facets, the electrostatic potential must vary on a microscopic scale close to the facet edge. In particular, the mechanism allowing for two unequal work functions to merge smoothly around an edge has remained largely unexplored up to now. The purpose of this chapter is to study, by means of *ab initio* calculations, the behaviour of the electrostatic potential and the local work function around metal facet edges.

We concentrate here on atomic-sharp edges between high-density facets in nanowires. The electrostatic potential around metallic facet edges has not been extensively studied theoretically on a microscopic scale up to now. An early theoretical study of a 90° jellium wedge [130] concentrated on the potential inside the metal, modelling the electronic density by a product of two one-dimensional surface distributions. The same wedge has also been studied more recently in the Thomas-Fermi approximation in relation with edge energies [10]. However, this model is known to be a poor approximation for surfaces, since the associated work function vanishes [44]. Experimentally, atomic-sharp edges are accessible by build-up of low-index facets due to surface diffusion in the presence of an electric field. This technique has been exploited in microtip fabrication for scanning tunnelling microscopy [131].

The nanowires we examine in this chapter have facets sufficiently large to reproduce single-surface electronic properties. Metallic wires with similar thicknesses are actually used in nano-scale devices [132] and can be fabricated by several techniques [133–137]. These nanowires have been imaged by scanning tunnelling microscopy [134, 135] or high-resolution transmission electron microscopy [132, 133]. Such experimental developments have motivated recent theoretical interest in structural [138, 139] and electronic [140–142] properties of unsupported nanowires [143].

As a prototype system exhibiting a measurable work function anisotropy, we focus on aluminium. We determine the charge density and the electrostatic potential near an edge between two equivalent and non-equivalent Al facets in Section 6.2. The importance of accounting for the ionic surface relaxation near facet edges is highlighted in Section 6.3. The broad features of the potential distribution outside a metal crystal are examined from a simple model of the surface dipoles in Section 6.4. Finally, we consider the effect of the image potential on the local work function outside a facet edge in Section 6.5, before concluding in Section 6.6.

6.2 Facet edges in aluminium crystals

A perfect facet edge is located at the boundary between two non-parallel clean crystalline surfaces. In order to characterise a facet edge, it is convenient to give the Miller indices $\{hkl\}$ of the two surfaces that join along it, but this information is not always sufficient to determine the facet edge uniquely. In cubic crystals, there can be up to 24 different acute angles, and 24 corresponding obtuse angles, between two crystal faces of given forms $\{hkl\}$ and $\{h'k'l'\}$. Between two faces of the same form $\{hkl\}$, a maximum of 16 different acute angles are possible [144]. The number of distinct angles is in many cases strongly reduced by symmetry. However, the number of inequivalent facet edges may be larger than the number of different angles, even with a monoatomic basis, as a consequence of the various translation states within the atomic planes perpendicular to a given direction. In Table 6.1, we display the number of inequivalent facet edges for the low-index fcc and bcc surfaces.

We have concentrated in this study on Al(100) and Al(111) facets and their mutual convex edges, which, as seen in Table 6.1, are few in number. These are the

Table 6.1: Total number of inequivalent convex angles between two crystal faces of given forms $\{hkl\}$ and $\{h'k'l'\}$ in cubic crystals. The numbers shown in brackets give the inequivalent facet edges in fcc/bcc crystals with a monoatomic basis. The two inequivalent (100)-(110) orthogonal facet edges a/b of a fcc crystal are shown below, as an example, where grey and white circles denote atoms in different parallel planes.

	{111}	{100}	{110}
{111}	2 (2/7)	2 (2/4)	3 (3/3)
{100}		1 (1/2)	3 (4/3)
{110}			3 (7/3)

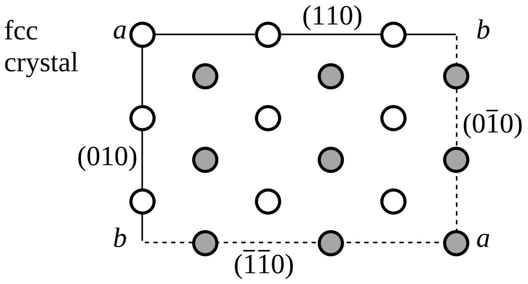

facets of highest density, and are known to possess the lowest surface energies [24, 145]. Real Al crystal surfaces therefore preferentially present these orientations [146], which also exhibit a measurable difference in work function. The charge densities and surface potentials at facet edges are determined from *ab initio* calculations by considering supercells containing metallic nanowires surrounded by vacuum regions.

For the facet edges between Al(100) and Al(111), we use 25 atoms in a 5 by 5 array, with 4 vacuum planes parallel to the (111) facet and 5 vacuum planes parallel to the (100) facet, with 8 k-points in the reduced Brillouin zone. For the Al(100)-Al(010) facet edge, respectively Al(111)-Al($\bar{1}$11), we use 25 atoms in a 5 by 5 array, with 5 vacuum planes along each dimension and 7, respectively 10, reduced k-points. In Figure 6.1, we display a three-dimensional view of the nanowire adapted for the Al(111)-Al($\bar{1}$11) facet edges and its associated supercell. In this geometry, the nanowire has a section in form of a parallelogram and is infinitely long. The supercell is chosen with two basis vectors parallel to the crystal facets and a third perpendicular basis vector along the facet edge of interest.

We use a Troullier-Martins pseudopotential [82] in the Kleinman-Bylander approximation [83]. The valence charge density is determined self-consistently by expanding the electronic wave functions on a set of plane-waves of kinetic energy up to 14 Ry.

6.2.1 Charge density at facet edges

Just as an extended crystalline surface can be characterised by a double-layer distribution of charge, the spilling of the electronic charge into the vacuum near

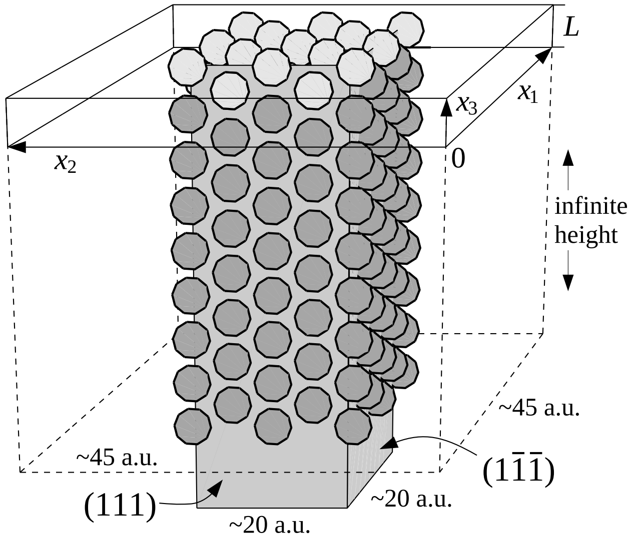

Figure 6.1: View in three dimensions (3D) of a typical nanowire for studying facet edges. The atoms forming the unit-cell basis (light grey circles) are shown in the supercell (solid lines), and are surrounded by vacuum. By repeating the unit cell (dashed lines), the column of atoms forms an edge between a (111) facet and a $(\bar{1}11)$ facet (greyed planes).

a facet edge creates a similar surface charge distribution. However, contrary to extended crystalline facets, the surface charge at a facet edge cannot unambiguously be measured by its dipolar moment and, near an extended edge, is best represented in a two-dimensional section perpendicular to the two facets. In order to extract the surface charge distribution near facet edges, we have developed a two-dimensional (2D) averaging procedure. Once the self-consistent three-dimensional charge density $\rho(x_1, x_2, x_3)$ is determined, a linear average parallel to the facets is performed to obtain a plane-projected 2D average electronic density $\overline{\rho}(x_1, x_2)$:

$$\overline{\rho}(x_1, x_2) = \frac{1}{L} \int_0^L dx_3 \, \rho(x_1, x_2, x_3), \tag{6.1}$$

where the coordinates x_1, x_2, and x_3 are measured along the supercell edges, L is the supercell height, and the third axis is chosen parallel to the two facets of interest. In order to obtain stable values of the charge density and potential inside the metal, the microscopic atomic-scale structure is evacuated by means of a 2D macroscopic average:

$$\overline{\overline{\rho}}(x_1, x_2) = \frac{1}{A} \int_{-d_1/2}^{d_1/2} dx'_1 \int_{-d_2/2}^{d_2/2} dx'_2 \, \overline{\rho}(x_1 + x'_1, x_2 + x'_2), \tag{6.2}$$

where d_1 and d_2 are the dimensions along the basis vectors of the 2D lattice unit cell of the crystal and A is its area. Orthogonal basis vectors have been assumed in Equation 6.2. Further details about this procedure may be found in Appendix A.2.

The two-dimensional averaging technique is illustrated in Figure 6.2 for a 90° facet edge between two equivalent Al(100) surfaces. The plane-projected valence electron charge density and the result of the 2D macroscopic average on the total charge are shown, thereby highlighting the surface dipole. The electronic density

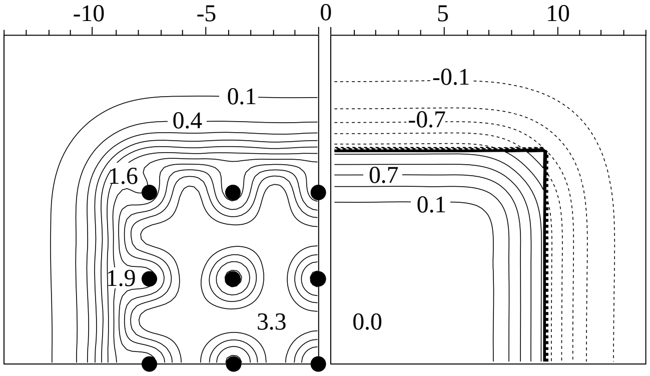

Figure 6.2: Plane-projected electronic charge density (left panel) and total macroscopic charge density (right panel) at a facet edge between two unrelaxed Al(100) surfaces. Dashed lines correspond to negative values. The contours are uniformly spaced by 0.3 electrons per unit cell. The black disks indicate the atomic columns. The axes are graduated in atomic units.

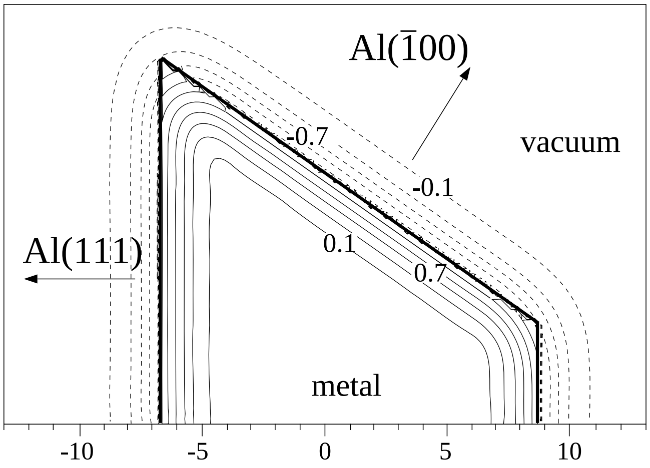

Figure 6.3: Contour plot of the total macroscopic charge density at the two inequivalent facet edges between unrelaxed Al(100) and Al(111) surfaces. The contours are uniformly spaced by 0.3 electrons per unit cell. Dashed lines correspond to negative values. The thick line shows the limit of the macroscopic ionic charge. The axes are graduated in atomic units.

is seen to smooth the sharp edge of the rectangular macroscopic ionic charge at the corner. The influence of the facet edge on the charge density extends up to the atomic columns surrounding the edge, beyond which stable densities characteristic of infinite facets are recovered.

We now turn to the facet edge between two non-equivalent surfaces, which possess different work functions and correspondingly dissimilar surface dipoles. Figure 6.3 shows the total macroscopic charge around the two different edges between Al(100) and Al(111) facets, without any surface relaxation. Near the obtuse edge, the electronic density closely follows the angled surface, with slight smoothing within ∼4 a.u. Around the acute angle, the electronic smoothing is notably stronger. The intrinsic difference between the two facets is not readily seen in the contour plot of the charge density, but leads, as we will see in the next section, to noticeable differences in the contour plot of the electrostatic potential.

6.2.2 Electrostatic potential around facet edges

To calculate the potential outside the nanowire and particularly at large distances from it, we must make abstraction of the repeated wires in neighbouring supercells. In order to determine the macroscopic electrostatic potential $\overline{\overline{v}}(x_1, x_2)$ outside a single isolated wire from the corresponding macroscopic charge $\overline{\overline{\rho}}(x_1, x_2)$, we use a modified 2D multipole scheme [147]. In this technique, the plane is divided into two separate regions by a circle surrounding the total macroscopic charge, chosen for convenience entirely within the supercell. To determine the potential inside this ring, we integrate the Poisson law in reciprocal space from the self-consistent charge density using the periodic boundary conditions imposed by the supercell. The potential is also determined in this way at a number of discrete points uniformly spread around the circle. If the disk is assumed to be in a perfect vacuum and not surrounded by supercell neighbours, the potential outside the disk can be expanded in terms of this set of values, as is detailed in Appendix A.3. To estimate the local work function $W_L(x_1, x_2)$, the bulk Fermi level E_F is subtracted from the macroscopic electrostatic potential $\overline{\overline{v}}(x_1, x_2)$:

$$W_L(x_1, x_2) = \overline{\overline{v}}(x_1, x_2) - E_F. \tag{6.3}$$

However, in this way, many-body effects, and particularly the image force felt outside the metal (which is not captured by the LDA approach), have not been included. Far from the metal surface, the image force may be neglected and we recover the correct local work-function value. In Section 6.5, we argue that the image force behaves monotonously around facet edges and that it should not contribute to the work function anisotropy in the vacuum.

The electrostatic potential created around an Al(100)-Al(010) facet edge, without any surface relaxation, is shown in Figure 6.4, where the Al nanocrystal is displayed in its entirety. The potential zero is set at the Fermi energy (of a bulk crystal), thus obtaining an approximation of the local work function. Just outside the centre of each facet, we reobtain the infinite-plane work function, calculated one-dimensionally (4.42 eV). The potential dips markedly near the edges, as seen from the contour lines extending further into the vacuum. This lowering in the electrostatic potential is created by a reduction of the surface dipole density near the facet edge. A similar picture was obtained in the theoretical study of stepped jellium surfaces [31], where the potential contour lines were seen to protrude near the tops of the ledges. Scanning tunnelling microscopy images of the local work function of Au/Cu(111) surfaces have also shown an experimental lowering of the potential near step edges (see Figure 2.15 and [55]). The aspect of the electrostatic potential calculated at a facet edge *ab initio* is strikingly different from that obtained for a jellium in the Thomas-Fermi approximation [10], where a

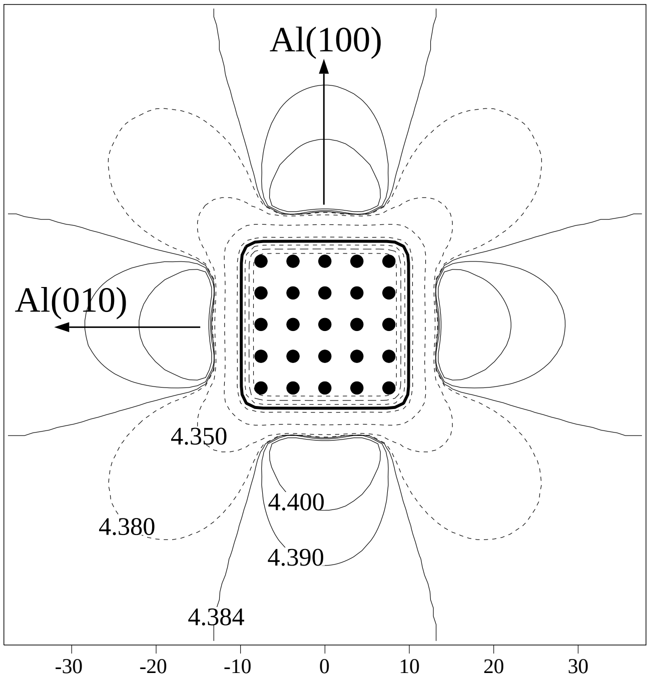

Figure 6.4: Contour plot of the macroscopic electrostatic potential distribution (in eV) around a facet edge between two Al(100) surfaces, without surface relaxation. The potential zero has been set at the Fermi energy (thick line). Continuous (dashed) lines indicate regions above (respectively below) the potential at infinity. The black disks indicate the atomic columns. The axes are graduated in atomic units.

near-monotonous smoothing around the edge was observed.

When leaving the nanocrystal in Figure 6.4 from an edge, for instance in the (110) direction, the potential increases monotonously to its value at infinity. Perpendicularly to the Al(100) facets, the potential shows a maximum corresponding to the value of the infinite-plane work function, before decreasing to its value at infinity. This decrease is characteristic of the finite size of the metallic slab, and shows that the edge influences the potential far outside the metal. Since we obtain outside the middle of each facet the value of the work function calculated for an infinite Al(100) surface, the size of our nanocrystal is expected to be sufficient to understand qualitatively the effect of edges on the potential outside macroscopic crystals. For larger crystals of similar geometry, we expect the general behaviour of the electrostatic potential calculated here to be retained far away from the crystal. However, larger spatial regions at the potential of the infinite-plane work function will develop outside each facet, with highly localised reduced potential areas near the facet edges. In Section 6.4.1, we will see that such a description is indeed consistent with the prediction of a model assuming surface dipoles uniformly distributed on the facets, but reduced near the facet edges.

One should not deduce from this first example that the electrostatic potential is always reduced near facet edges. Figure 6.5A shows the potential outside edges between two Al(111) facets, without any ionic relaxation. At the acute edge between two Al(111) facets, the electrostatic potential is seen to be locally raised. Pursuing our interpretation of work function anisotropy trends in alu-

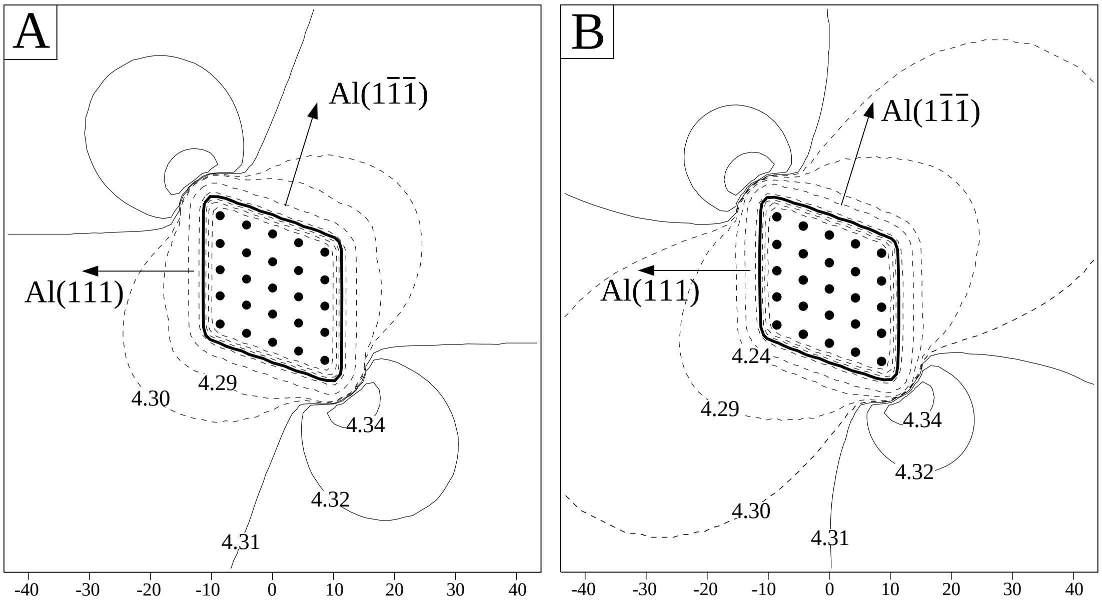

Figure 6.5: Contour plot of the macroscopic electrostatic potential distribution (in eV) around facet edges between two Al(111) surfaces. Panel A omits (and panel B respectively includes) surface relaxation. The potential zero has been set at the Fermi energy (thick line). Continuous (dashed) lines indicate regions above (respectively below) the potential at infinity. The disks indicate the atomic columns. The axes are graduated in atomic units.

Figure 6.6: Contour plot of the macroscopic electrostatic potential distribution (in eV) around unrelaxed facet edges between two $\mathrm{Al}_{Z=1}(111)$ virtual-crystal surfaces. The $\mathrm{Al}_{Z=1}$ virtual atoms, defined in the text, are placed on an Al fcc lattice. The potential zero has been set at the Fermi energy (thick line). Continuous (dashed) lines indicate regions above (respectively below) the potential at infinity. The disks indicate the atomic columns. The axes are graduated in atomic units.

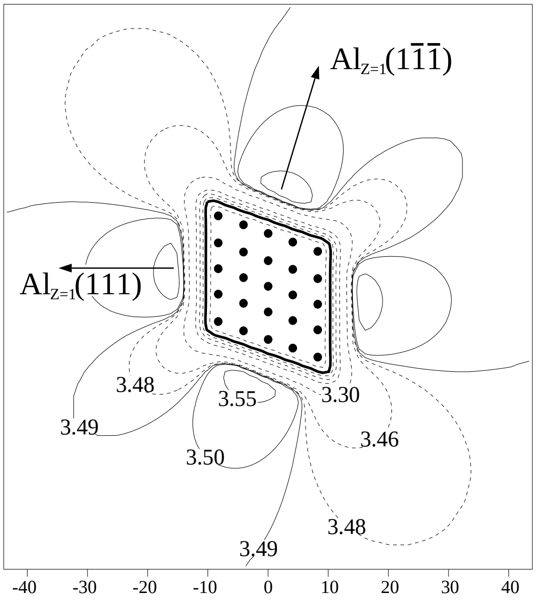

minium presented in Section 5.2, the local rise in potential outside the edges between low-work-function Al(111) facets can be explained in terms of a change in the occupation numbers of the atomic-like p-orbitals on the edge atoms. At a facet edge, the asymmetry between the three directional p-orbitals is different from that of an atom in an extended facet. Only one $p_{\|}$-orbital on the edge atom is parallel to both facets, whereas two $p_{\|}$-orbitals are parallel to an extended surface. Compared to atoms at the surface of extended Al(111) facets, a decrease in the occupation of the $p_{\|}$-states is present at the edges studied here and a corresponding increase in the occupation of the atomic-like $p_{\perp}$-states perpendicular to the facet edges is induced. This redistribution of charge among the inequivalent orbitals of the edge atoms creates a local increase in potential outside the acute edge.

This interpretation is supported by a numerical experiment, similar to those presented in Section 5.2, where we change the number of electrons associated with each Al ion. In Figure 6.6, we display a crystal of $\mathrm{Al}_{Z=1}$ virtual atoms—formed by linearly scaling the Al pseudopotential by 1/3—arranged in the same geometry as Figure 6.5A. Outside the centres of the facets, the potential compares favourably with the work function calculated for a laterally-infinite surface of this orientation and valence (from Figure 5.6: W=3.58 eV). However, compared to real Al, the general aspect of the potential outside the nanocrystal has changed considerably. The potential now shows extended regions of low work function at both the acute and the obtuse edges. We believe this behaviour represents the general case for metals which do not possess an open shell of p-states (and for edges between equivalent facets). This is confirmed by a further study of a Na bcc nanowire with 60° and 120° edges between (110) facets (see Figure 6.7), where an analogous localised reduction in the electrostatic potential is seen near the edges.[1]

The local work function around unrelaxed edges between two inequivalent Al facets is shown in Figure 6.8A. The small difference between the surface charge densities of the two orientations induces an observable potential anisotropy. The presence of a potential gradient outside the metal near the facet edge allows the two different work functions to merge smoothly. On account of the lower symmetry of the crystal morphology, we observe that the work function varies more strongly near the edges than in the case of equivalent facets. Here, on travelling to infinity, the electrostatic potential always increases perpendicularly to the Al(111) facets, which possess a low work function. Perpendicularly to the high-work-function Al(100) surface, the potential shows a maximum before decreasing as the distance

---

[1] The parameters used for this nanowire are 36 atoms in a 6 by 6 array, with 6 equivalent vacuum layers in each direction. We use a plane-wave kinetic-energy cutoff of 14 Ry and 8 reduced k-points.

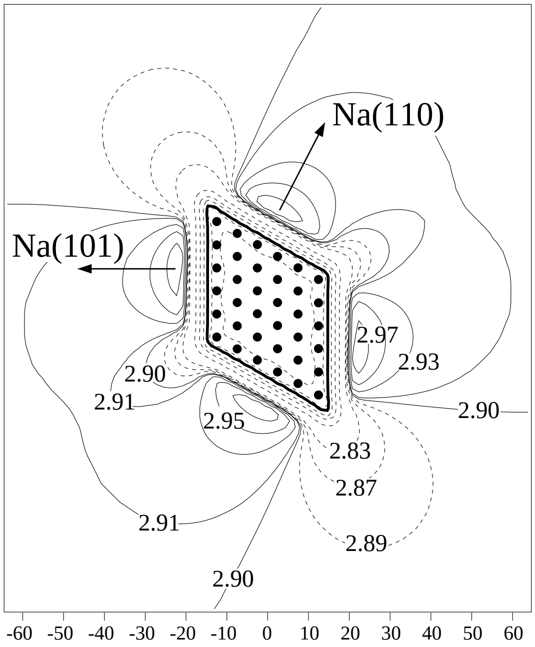

Figure 6.7: Contour plot of the macroscopic electrostatic potential distribution (in eV) around unrelaxed 60° and 120° edges between two Na(110) facets. The potential zero has been set at the Fermi energy (thick line). Continuous (dashed) lines indicate regions above (respectively below) the potential at infinity. The disks indicate the atomic columns. The axes are graduated in atomic units.

to the surface increases. At infinity, the electrostatic potential is intermediate between the two face-dependent work functions.

6.3 Effect of ionic relaxation

We have calculated the ionic relaxation near the facet edges of high-density Al surfaces by allowing the top layer of surface ions in our set of nanowires (see Section 6.2) to move to their equilibrium positions. In this way, the crystalline interplane spacing is retained in the central region of the nanowire and the macroscopic averages can be conveniently performed. The resulting equilibrium structures for the three nanocrystals are displayed in Figure 6.9. The corner ions are seen to relax strongly inwards: at the edge between two Al(100) facets, the corner ion is displaced by 4.1% of a lattice unit along the diagonal [110] direction, while at the acute (obtuse) edge between Al(111) facets, the corner ion is displaced by 2.7% (respectively 2.2%) of a lattice unit along the [100] (respectively [110]) diagonal. The nearest neighbours of the corner ion compensate this inward movement by relaxing slightly outwards. At the acute angle between an Al(100) and an Al(111) facet, the corner ion moves by 10.3% of a lattice unit towards the metal interior. The other surface ions of this nanocrystal show a combination of normal and tangential relaxation. This global trend of inward relaxation can be understood from the electrostatic model of Finnis and Heine (see Section 2.3.1). By extending this model to facet edges, we see that the edge ions should relax inwards because of the smoothing of the electronic density around the facet edges, as observed in

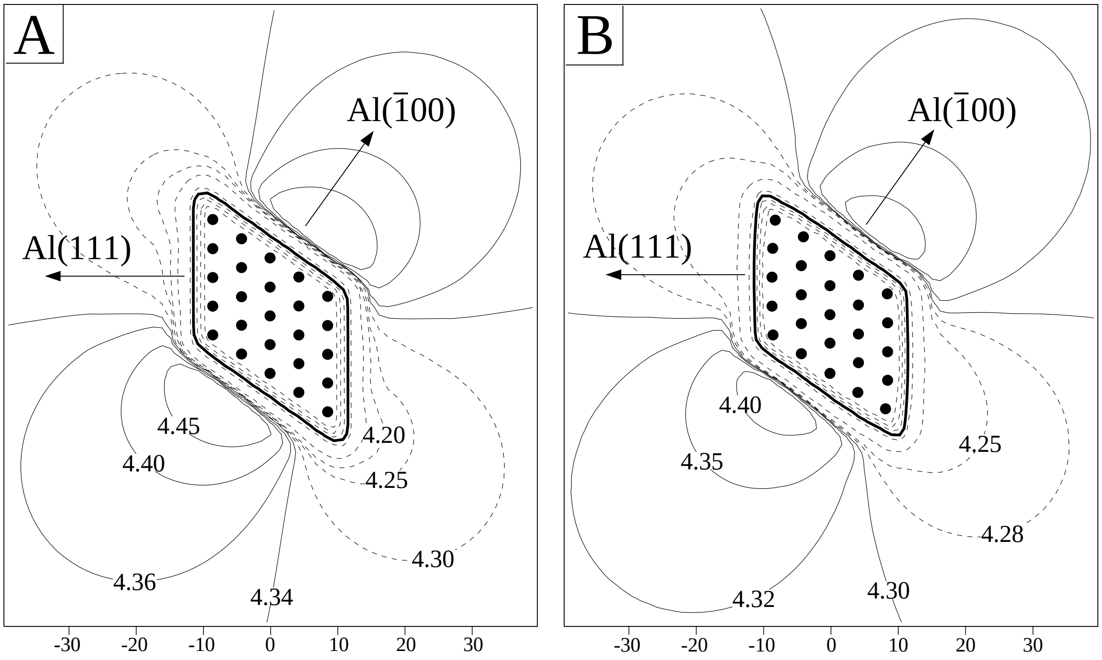

Figure 6.8: Contour plot of the macroscopic electrostatic potential distribution (in eV) around the two different facet edges between Al(100) and Al(111) facets. Panel A omits (and panel B respectively includes) surface relaxation. The potential zero has been set at the Fermi energy (thick line). Continuous (dashed) lines indicate regions above (respectively below) the potential at infinity. The disks indicate the atomic columns. The axes are graduated in atomic units.

Section 6.2.1.

The surface relaxation at Al(100) facets does not significantly influence the electrostatic potential outside the metal. However, as seen when comparing Figures 6.5A and 6.5B, the surface relaxation around edges between Al(111) facets has an important effect on the electrostatic potential outside the metal. When including the relaxation, the work function of a laterally-extended Al(111) surface (4.23 eV) is more closely approximated just outside the nanocrystal. A larger region of constant work function then develops in the neighbourhood of the (111) facets. A similar situation is observed when comparing Figures 6.8A and 6.8B, which respectively omit and include the surface ionic relaxation near the edges between inequivalent facets. Once again, the infinite-plane work functions are better recovered outside the facets, both in the Al(100) direction and in the Al(111) direction, when the surface relaxation is included. We see that the ionic relaxation allows the infinite-plane work functions to be recovered closer to the edge. Whereas the ionic surface relaxation does not appreciably influence the work function of infinite metal surfaces, these results show that it must be taken into account when

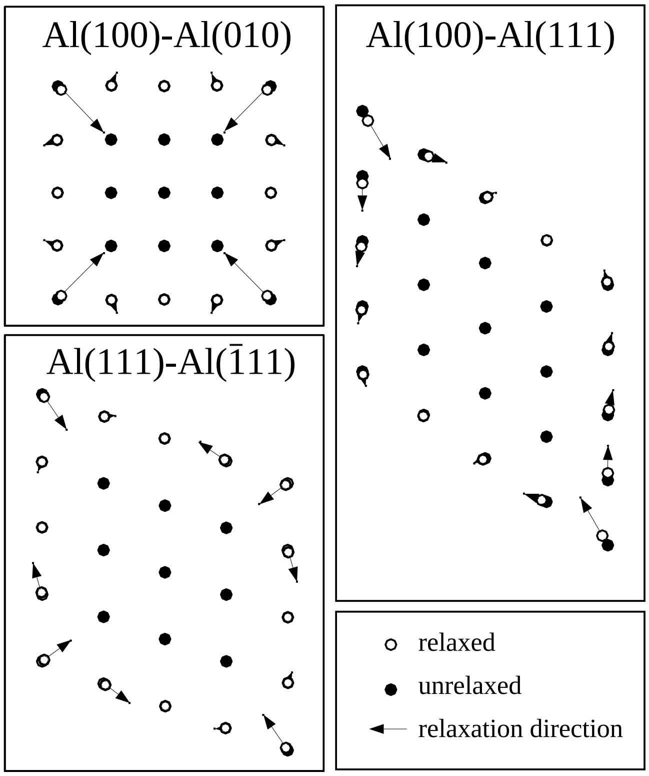

Figure 6.9: Relaxation of surface atoms near edges between Al(100) and Al(111) facets. The black circles indicate the unrelaxed atomic columns, and the white circles the relaxed positions. The arrows indicate the direction of the relaxation. Their lengths are proportional to the relaxation distance, multiplied by a factor 15 for the Al(100)-Al(010) and Al(111)-Al($\bar{1}$11) edges (left panels) and by a factor 5 for the Al(100)-Al(111) edges (right panel).

studying the electrostatic potential near metal facet edges.

6.4 Surface dipole models

Our first-principles studies of nanocrystals suggest that facet edges are generally characterised by a highly-localised change in dipole density compared with infinite surfaces. We have sought to understand qualitatively the effect of a variation in dipole density near a facet edge by reproducing the electrostatic potential in the vacuum from model distributions of the surface dipoles. In this way, by extrapolating from our exact calculations by mainly analytical models, we can predict the apparent work functions of macroscopic crystals that are inaccessible to exact computations as a result of their large dimensions. In view of image effects, the electrostatic potential is expected to reflect the local work function outside a macroscopic crystal at distances beyond 100 nm. The apparent work function, at an infinite distance from the crystal, is independent of all image effects and can be computed exactly from the electrostatic terms only. In keeping with the results of our *ab initio* simulations, we focus essentially on two-dimensional crystals that preserve the bulk periodicity along the third dimension.

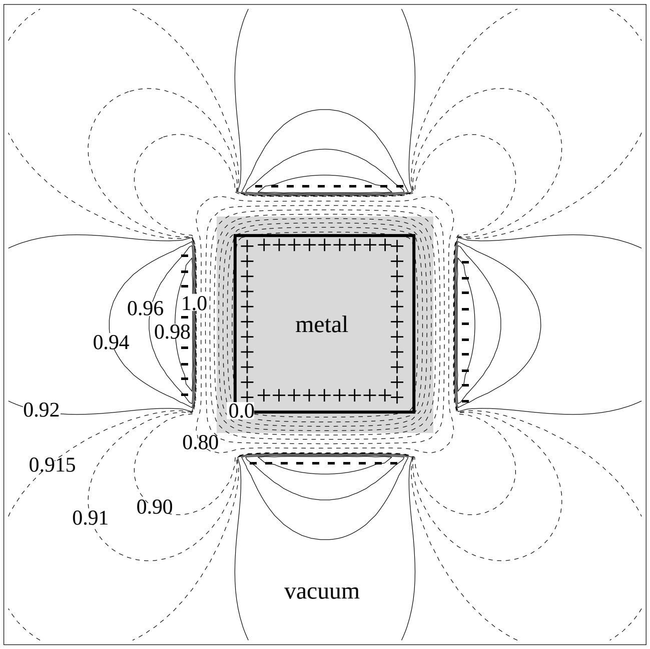

Figure 6.10: Contour plot of the electrostatic potential created by a model distribution of the surface dipole for a small square crystal (greyed area) with equivalent facets. The surface charge consists of two parallel uniform sheets (+/-), forming a finite capacitor. The contours are indexed in multiples of the potential step W_0 created by an infinite planar capacitor. Continuous (dashed) lines indicate regions above (respectively below) the potential at infinity.

6.4.1 Finite crystal with equivalent facets

To model the surface of a metallic crystal with equivalent facets, we approximate the surface dipole by finite planes of charge. The spilling of the electrons in the vacuum creates a surface dipole which we reduce to two oppositely-charged planes, separated by a distance on the order of the Thomas-Fermi wavelength. On a macroscopic scale, the dipole is uniform across perfectly-clean facets, with a possible reduction in intensity near the edges. As a consequence, we use uniformly-charged parallel planes of charge arranged around the crystal surface. Since the facets are all equivalent and possess the same work function, no charge transfer takes place between the crystal facets.

In Figure 6.10 we consider the case of an elongated crystal of square section. We have imposed a surface dipole consisting of uniformly-charged parallel planes abruptly terminated at the facet edges. This leads to a complete absence of dipoles along the crystal diagonals, and thus a great reduction in the dipole density in the edge neighbourhood. In this coarse approximation, we are therefore neglecting the electronic smoothing around the edge. Nevertheless, the resulting potential shows an analogous distribution to that obtained self-consistently for the edge between two Al(100) facets (see Figure 6.4), where the surface dipole is known to be reduced at the facet edge. We note that in Figure 6.10, the potential is locally increased perpendicularly to the middle of the facets, while in the edge region, it is below the potential at infinity. Near the edges, the characteristic leaking of the contour lines into the vacuum, as well as the presence of contour lines extending

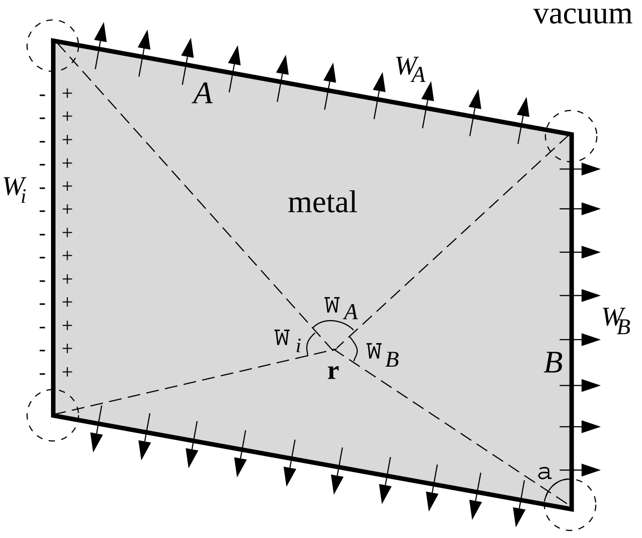

Figure 6.11: Modelling facets of a two-dimensional macroscopic metallic crystal by planes of point dipoles. Far from each facet edge (dotted circles), the uniform double layer of charge (+/- symbols) is replaced by a plane of point dipoles (arrows). The dipolar contribution to the potential at any point **r**, inside or outside the crystal, is found by averaging the potential step W_i of each facet weighted by its apparent angle Ω_i.

to infinity, is well reproduced. These effects result from a reduced dipole density near the facet edges and are seen neither if a superposition of atomic charges is used as a model charge distribution nor in the Thomas-Fermi approximation [10]. Compared with the *ab initio* calculation, the apparent work function—given by the energy of the contour line extending to infinity and here equal to $\overline{W} = 0.92\ W_0$—is seen to be more strongly reduced with respect to the potential at the centre of the facet. This reflects the fact that the surface dipole density near real aluminium facet edges does not completely vanish, as is assumed in this model.

In macroscopic crystals of large dimensions, the influence of the localised change in dipole density near the facet edges can be neglected and the surfaces can be viewed as uniform planes of point dipoles (see Figure 6.11). For elongated crystals of arbitrary polygonal section, if we fix the electrostatic potential at infinity to zero, the potential V^d induced by the planes of dipoles at any point $\mathbf{r} = (x, y)$ is analytically given by a weighted average over the face-dependent potential steps (indexed by i) [148]:

$$V^d(\mathbf{r}) = \frac{1}{2\pi} \sum_i s_i\ \Omega_i\ W_i. \tag{6.4}$$

Ω_i is the apparent two-dimensional angle from **r** of the plane of dipoles associated with a potential step W_i. s_i is a sign coefficient equal to -1 (respectively +1) if the surface dipole points away from (towards) **r**. Equation 6.4 shows that if all the crystal facets possess the same potential step W_0, the electrostatic potential outside the metal is constant and equal to zero. Inside the metal, the potential $V^d(\mathbf{r})$ is also uniform, as required, and is equal to $V^d(\mathbf{r}) = -W_0$. These results are independent of the shape of the crystal and can be generalised to three dimensions by considering solid angles Ω_i and normalising the sum in Equation 6.4 to $1/4\pi$ [148]. We note that in the above discussion, we could have identified W_0 with the work function of the facets, and not necessarily with the full surface dipole, since the Fermi energy gives a constant shift inside the metal with respect to the average electrostatic potential. In this case, the potential V^d would represent an estimate of the local work function (referred to the value at infinity).

We have thus shown that the apparent work function $\overline{W}$ of a finite macroscopic crystal with equivalent facets is given by the work function W_0 obtained in a one-dimensional calculation. This result is independent of the angles between the facets and is valid for facets of macroscopic dimensions. If the facets are reduced to a few atomic planes, and in the standard case of a reduction in dipole density at the facet edge, the apparent work function $\overline{W}$ will be slightly lower than the work function W_0 of an infinitely-extended facet.

6.4.2 Finite crystal with non-equivalent facets

If a finite metallic crystal is bounded by facets with different work functions, macroscopic charge transfers between the various facets are expected (see Section 2.3). These surface charges strongly influence the electrostatic potential in the vacuum. In this section, we propose a general procedure for calculating charge transfers in model systems, and apply it to surface charge redistributions in two-dimensional crystals with two different work functions.

We assume the metal surface can be modelled by a continuous arrangement of dipoles, taken to describe the potential step between the Fermi energy and the electrostatic potential just outside the crystal (see Figure 6.11 and the accompanying discussion). If the crystal facets possess different work functions, the potential $V^d(\mathbf{r})$ induced by the surface dipoles is not constant inside the metal. The variation of the dipolar potential inside the metal is corrected by the presence of a surface charge density $\sigma(\mathbf{r})$ on the metal facets. The surface charge induces a supplementary electrostatic potential $V^\sigma(\mathbf{r})$ that we impose equal, inside the metal, to the opposite of the dipolar potential (within a constant W):

$$V^\sigma(\mathbf{r}) = -V^d(\mathbf{r}) - W. \tag{6.5}$$

The value of the constant W is fixed by the requirement that the total surface charge vanishes, since the crystal is globally neutral. If S is the crystal surface, we impose:

$$\int_S \sigma(\mathbf{r})\ \mathbf{dr} = 0. \tag{6.6}$$

The surface charge density on each facet depends on the entire crystal geometry. We can determine it numerically using a technique similar to the charge simulation method [149, 150].[2] The potential variation inside the metal is first reproduced to within a guessed constant W by arranging a dense set of discrete charges (or line charges in the case of elongated crystals) on the surface S. The total charge is examined, the potential constant W is adjusted accordingly, and the process is repeated. When the total charge vanishes, the potential constant gives the apparent work function $\overline{W}$, equal in this model to the potential difference between the region at infinity and the metal interior.

Geometrical considerations of Equation 6.4 show that the potential variation follows a number of scaling laws that we can conveniently exploit. We note that $V^d(\mathbf{r})$ depends only on a set of angles. If the crystal dimensions, collectively written as $\{L_i\}$, are homogeneously expanded by a factor λ, keeping all angles fixed, we note that the potential is globally unchanged:

$$V^d_{\{\lambda L_i\}}(\lambda \mathbf{r}) = V^d_{\{L_i\}}(\mathbf{r}). \tag{6.7}$$

The potential induced by the surface charge density must follow the same scaling law, which leads to a surface charge density that is inversely proportional to the size of the crystal (in two or three dimensions):

$$\sigma_{\{\lambda L_i\}}(\lambda \mathbf{r}) = \frac{1}{\lambda}\sigma_{\{L_i\}}(\mathbf{r}). \tag{6.8}$$

This observation is independent of the crystal geometry and leads to minute charge densities in macroscopic crystals.

We now consider the special case of two-dimensional crystals that have the shape of a parallelogram with facets of lengths A and B, that are equivalent two by two. We model the surface double layer by uniform planes of dipoles that are associated with surface-dependent work functions W_A and W_B respectively (see Figure 6.11). The variation in electrostatic potential, outside the crystal, is a linear function of the difference in the two work functions. This result is derived from Equation 6.4 by considering the various angles Ω_i when $\mathbf{r}$ is outside the crystal. It is convenient, in the following discussion, to take the potential inside the metal as the reference energy for $V(\mathbf{r}) = V^d(\mathbf{r}) + V^\sigma(\mathbf{r})$ and to decompose the electrostatic potential $V(\mathbf{r})$ into:

$$V(\mathbf{r}) = \begin{cases} 0 & \text{if } \mathbf{r} \text{ is inside the metal} \\ (W_A - W_B)\, v_{A,B,\alpha}(\mathbf{r}) + W_B & \text{if } \mathbf{r} \text{ is outside the metal} \end{cases} \tag{6.9}$$

$v_{A,B,\alpha}(\mathbf{r})$ is a reduced potential that depends on the facet lengths A and B as well as on the angle between the facets α, but is independent of the work functions

---

[2] Contrary to some applications of the charge simulation method, the surface charge densities calculated here are real.

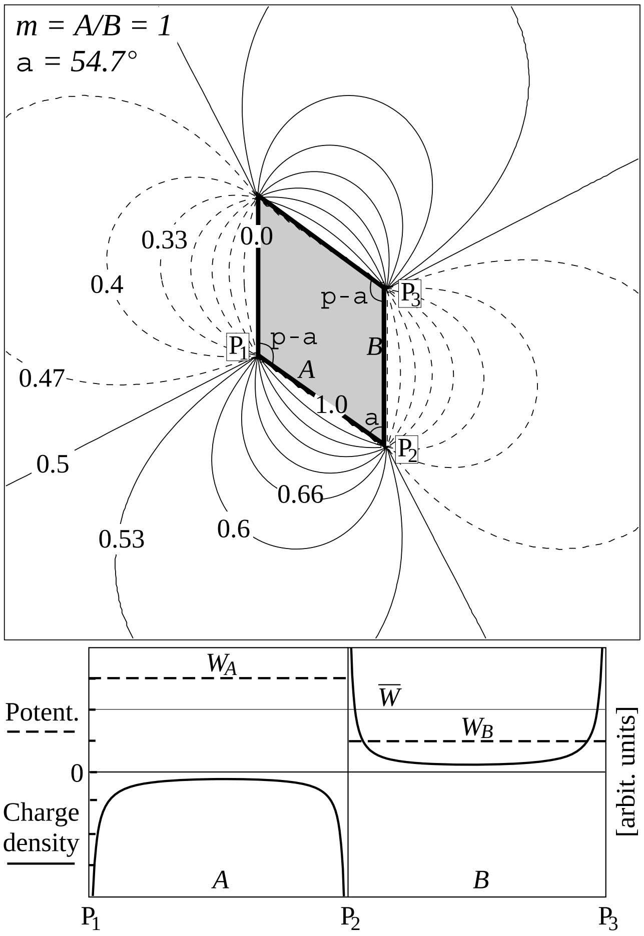

Figure 6.12: Electrostatic potential outside a model crystal with non-equivalent facets of length A and B, with an aspect ratio $m = A/B = 1$. The angle between the facets is $\alpha = 54.7°$. Upper panel: Contours of the reduced potential $v(\mathbf{r})$ (see main text). Continuous (dashed) lines show areas above (respectively below) the potential at infinity. Lower panel: potential just outside the crystal surface (dashed lines) and surface charge density along the two facets (thick solid lines). The apparent work function is the average of the two face-dependent values $\overline{W} = (W_A + W_B)/2$.

W_A and W_B. Using this definition, the reduced potential $v_{A,B,\alpha}(\mathbf{r})$ varies from 0 (just outside facet B) to 1 (outside facet A) in the vacuum. If the origin of the coordinate system is chosen in the centre of the parallelogram, we note that for all real λ, the potential scaling is written:

$$v_{\lambda A,\lambda B,\alpha}(\lambda\mathbf{r}) = v_{A,B,\alpha}(\mathbf{r}). \tag{6.10}$$

In the following analysis, we only need to consider reduced potentials $v_{m,\alpha}(\mathbf{r})$ that depend on the angle α and the aspect ratio $m = A/B$. The apparent work function $\overline{W}$ is now written (using Equation 6.9):

$$\overline{W} = (W_A - W_B)\overline{w}_{m,\alpha} + W_B, \tag{6.11}$$

where $\overline{w}_{m,\alpha}$ is the value of $v_{m,\alpha}(\mathbf{r})$ at an infinite distance from the crystal.

In Figure 6.12 we show a contour plot of the total reduced potential distribution $v_{m,\alpha}(\mathbf{r}) = v^d(\mathbf{r}) + v^\sigma(\mathbf{r})$ outside a crystal with four facets of equal length ($m = A/B = 1$). The angle between the facets is equal to that between a (111) and a (100) surface in a face-centered cubic metal. In view of the symmetry, the

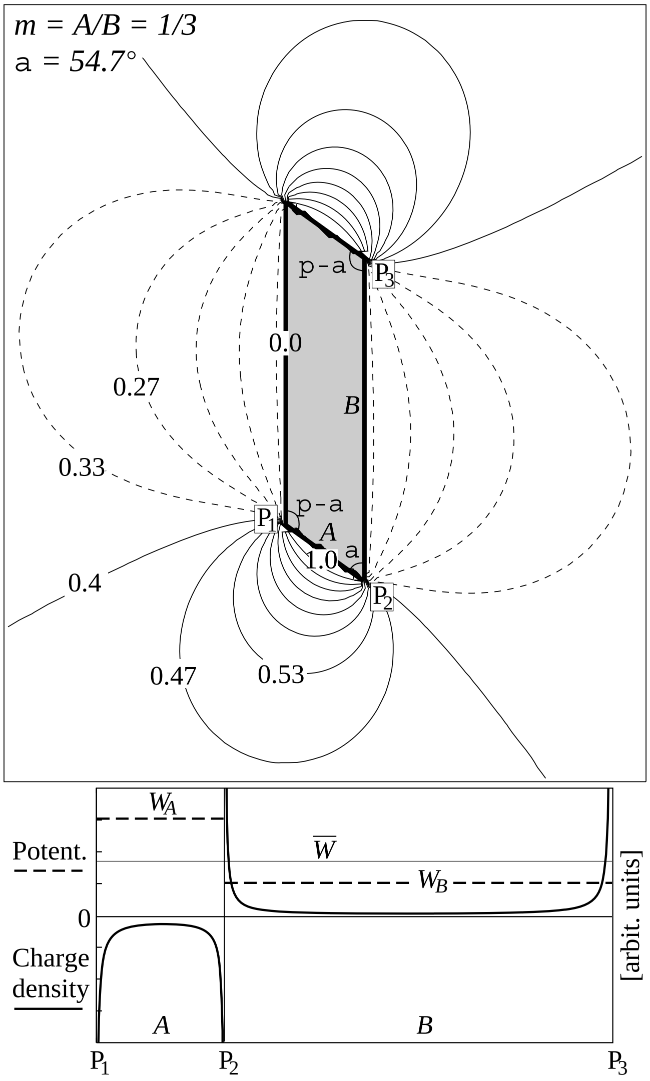

Figure 6.13: Electrostatic potential outside a model crystal with non-equivalent facets of length A and B, with an aspect ratio $m = A/B = 3$. The angle between the facets is $\alpha = 54.7°$. Upper panel: Contours of the reduced potential $v(\mathbf{r})$ (see main text). Continuous (dashed) lines show areas above (respectively below) the potential at infinity. Lower panel: potential just outside the crystal surface (dashed lines) and surface charge density along the two facets (thick solid lines). The reduced apparent work function is $\overline{w} = 0.344$.

apparent work function is equal here to the average of the two face-dependent values $\overline{W} = (W_A + W_B)/2$. The surface charge density is shown in the lower panel of Figure 6.12. For all the parallelograms studied here, as is noted in this figure, the facets of higher work function carry a negative charge. In view of the two different work functions coexisting at each facet edge, the potential is discontinuous along the outside perimeter of the parallelogram. This leads to a surface charge density that diverges at each vertex of the parallelogram. However, at real facet edges, the smoother variation of surface dipole density near the facet edge is expected to induce a finite charge transfer between the various crystal facets. Figure 6.13 shows the more general case of a metal crystal with facets of unequal length ($m = A/B = 1/3$). The apparent work function ($\overline{w} = 0.344$) is now biased towards the facet with the larger surface area. The surface charge density is correspondingly lower on the larger facet.

We have calculated the apparent reduced work functions $\overline{w}_{m,\alpha}$ for all possible parallelograms. In the special case of rectangular crystals, we have plotted the apparent work function $\overline{w}_{m,\pi/2}$ as a function of the aspect ratio m in Figure 6.14. By symmetry, we note that for all angles α:

$$\overline{w}_{1/m,\alpha} = 1 - \overline{w}_{m,\alpha}. \tag{6.12}$$

We also compare in Figure 6.14 the result of our model with the average value of the face-dependent work functions weighted by their respective surface areas, which is the correct formula for the apparent work function of cylindrical polycrystalline samples (see Section 2.3). In our geometry, it appears this formula is too strongly biased towards the work function of the larger facet. To study the apparent work function variation with the angle α, we introduce a parameter β that gives the deviation from a rectangle: $\beta = \pi/2 - \alpha$. Once again, by symmetry, we note that:

$$\overline{w}_{m,\pi/2-\beta} = \overline{w}_{m,\pi/2+\beta}. \tag{6.13}$$

As β deviates from zero, the variation of $\overline{w}_{m,\pi/2+\beta}$ is then at most of second order in β. Our numerical study has shown that the sensitivity of the apparent work function on β is very small. In Figure 6.14, the work function of a highly-slanted crystal is compared to that of a rectangle. Even in this extreme case, the apparent work function only deviates by at most 1.5% from the result for a rectangle. For two-dimensional crystals in the shape of a parallelogram, we thus find a nearly-universal behaviour of the apparent work function as a function of the ratio of the facet lengths.

These simulations have allowed us to calculate the potential distribution outside a metal with anisotropic work functions. Our procedure for including the effect of a charge transfer between the different facets is widely applicable and can be put into practice for any crystal geometry. We have calculated the apparent work functions of two-dimensional macroscopic crystals with sections in the shape of parallelograms and seen that the apparent work functions show a quasi-universal dependence on the lengths of the crystal facets with different work functions.

6.5 Image potential near facet edges

In order to describe correctly the local work function outside metallic surfaces, the exchange-correlation potential $\epsilon_{xc}(\mathbf{r})$ should be added to the electrostatic potential energy. Far from a planar metal surface, the exact exchange-correlation potential is known to follow the classical image law and decay as $-e^2/4r$ with the distance r to the crystal surface. While the classical potential diverges unphysically at

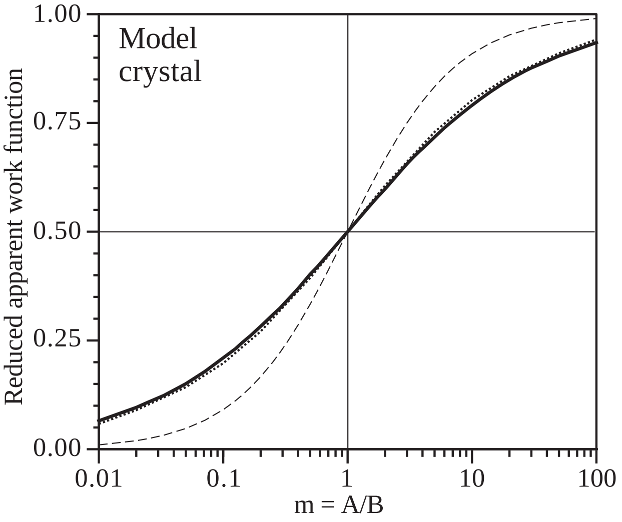

Figure 6.14: Reduced apparent work function $\overline{w}$ of a crystal with non-equivalent facets, as a function of the aspect ratio m, for a rectangle (solid line) and a highly-slanted parallelogram with $\alpha = 10°$ (dotted line). The dashed line gives the surface-area-averaged reduced work function.

the metal surface, it describes correctly the exchange-correlation potential felt by an electron in the vacuum beyond the range of the microscopic surface dipole, provided that r is taken as the distance to the effective image-plane surface [34]. This long-range behaviour is not included in the LDA approximation and is thus absent in our *ab initio* simulations. The LDA $\epsilon_{xc}(\mathbf{r})$ potential decays exponentially in the vacuum with the charge density, and is therefore qualitatively incorrect far from the surface.

For a classical charge in the vicinity of an infinite conducting wedge, the electrostatic potential in the vacuum is known analytically in terms of a collection of image sources [151]. Their locations and values depend on the position of the source charge and the angle of the wedge. Using the formalism developed in Reference 151, we have calculated the image potential felt by a classical electron outside a metallic facet edge, by integrating the work effected against the image force on taking the charge to infinity. The calculation is described in detail in Appendix A.4. In Figure 6.15 we have plotted the classical image potential around both a 90° and an acute metal wedge, corresponding respectively to a fcc (100)-(010) facet edge and a fcc (100)-(111) facet edge. In both cases, the two-dimensional image potential behaves monotonously around the facet edge, quickly recovering a distribution normal to the facets characteristic of an infinite plane.

As in the case of an infinite surface, the classical image potential near a conducting wedge is expected to provide a good approximation of the exchange-correlation potential outside a metallic facet edge further than ~10 a.u. from the surface [152]. From the monotonous behaviour of the image potential near the facet edge, we conclude that our calculations of the electrostatic potential near metal facet edges, presented in the previous sections, are sufficient to describe

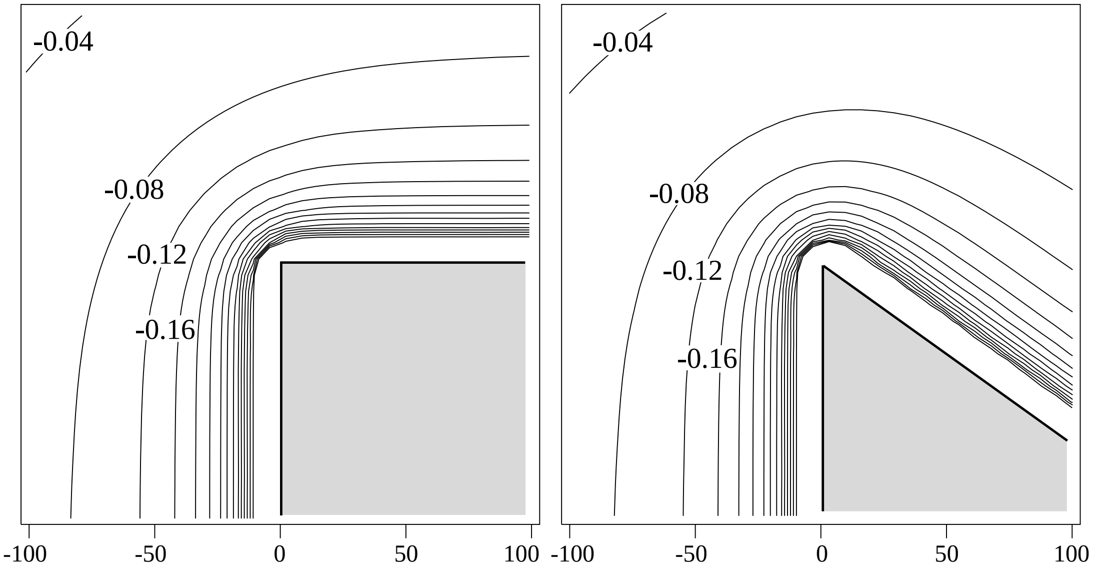

Figure 6.15: Classical image potential, in eV, near metallic wedges (shaded areas). Left panel: 90° degree wedge. Right panel: 54.7° degree wedge (corresponding to an edge between a (111) and a (100) facet in a face-centered cubic metal). The contour lines are equally spaced by 0.04 eV. The axes are graduated in atomic units.

correctly the variation of the local work function beyond the immediate neighbourhood of the crystal surface.

6.6 Conclusions

The electrostatic potential around various sharp edges between equivalent Al facets has been determined *ab initio*, exhibiting a more complex distribution than in previous approximate theoretical studies. At an edge between equivalent facets, we often observe a decrease in dipole density that induces a local reduction in the electrostatic potential just outside the facet edge. The edges between two equivalent Al(111) facets are an exception to this rule and are understood in terms of a charge redistribution among the atomic-like *p*-orbitals of the edge atoms.

We have shown for the first time how two different work functions can coexist on either side of a edge between inequivalent facets, and how they merge close to the facet edge. The relaxation of the surface ions near facet edges influences the electrostatic potential in the vacuum more strongly than in the case of infinite planar surfaces. It must be taken into account in order to recover the infinite-plane orientation-dependent work functions close to facet edges.

Simple models of the surface dipole density have allowed us to comprehend how the electronic charge is distributed near facet edges and how it differs from the case of an infinite plane. By extrapolating from our *ab initio* studies of the surface dipole densities of nanowires, we can predict the apparent work functions of larger macroscopic crystals with non-equivalent facets.

Modern Research

In my youth I was always dead keen
On the lab and the practical scene:
    The electrics, the glassware,
    The wax, string and brassware...
But now there is only a screen.

Joan M. Freeman

To Algebra God is inclined -
The world is a thought in His Mind.
    It seems so erratic
    Because it's quadratic,
And the roots are not easy to find.

J. C. B. Date

Chapter 7

Conclusions

IN this thesis, we have been concerned with calculating from first principles, in the framework of density functional theory, the work functions of various clean elemental metal crystals. These state-of-the-art calculations have been performed for theoretical interest in this fundamental electronic property of surface physics and to clarify the origins of some experimental data, such as the observation of work function anisotropies, that were not previously fully understood.

Before interpreting the experimental data from theory, we have made sure that our *ab initio* work functions are of sufficient accuracy. The precision of theoretical work functions has up to now been limited by quantum size effects induced by the artificial use of thin slabs of metal, which are imposed by present-day computational resources. Our procedure, developed fully in Chapter 4, allows us to calculate the work functions of metals without relying on the position of the thin-film Fermi energy, which is sensitively influenced by the slab thickness. By focusing on integrated quantities, such as the total charge density, and by applying a macroscopic-averaging technique, we have shown how more stable work functions are obtained when the film thickness decreases down to a few atomic layers. We have applied our technique to aluminium thin films, where large quantum size effects are expected because of the high electronic density and nearly-free-electron character of the valence electrons. In view of the results obtained, we deduce that our procedure is broadly applicable to derive accurate work functions—as well as work-function changes under physisorption or chemisorption—for a broad range of materials.

Building on our accurate calculational technique, we have been able to observe theoretical work function anisotropies in a number of elemental metals. In Chapter 5, we reproduced the experimental trends in the work functions of sodium, aluminium, copper and gold. The Smoluchowski model, which attributes work function anisotropies to the surface smoothing of an inhomogeneous electronic fluid, has only limited success in predicting the dependence of the work function on the surface orientation. We have shown that its deficiencies result from its failure to account for the orbital nature of the occupied electronic states. The arrangement of electronic charge around the surface atoms, in particular, is crucial for understanding work function trends. By contrast, the potential resulting from the ionic surface relaxations is nearly perfectly screened and does not significantly contribute to the work functions. In *sp* metals, for example, the observed work function anisotropy has been shown, in this thesis, to result from the rearrangement of charge from the atomic-like *p* orbitals pointing into the vacuum to those within the surface plane, and to follow a trend opposite to that given by the Smoluchowski rule. We demonstrated that the redistribution of charge on the surface atoms also influences the ionic relaxation, and in particular can account for the exceptional outward relaxation of high-density aluminium surface planes. In copper and gold, the presence of semi-core *d* orbitals is shown to produce complex hybridisations with the *s* valence electrons and to induce charge transfers among the orbitals of the surface atoms. The resulting effects on the work functions again do not necessarily follow the predictions of simple models.

We extended our study of face-dependent work functions to *ab initio* computations of finite facets in Chapter 6. We have studied the potential outside edges between both equivalent and non-equivalent facets, and showed in the latter case how two different work functions coexist on either side of a facet edge. In general, a reduction in the dipole density is observed at the edges between equivalent facets, which induces a lower local work function than outside an extended surface. For small crystals, where edge effects contribute strongly, this modification is seen to reduce the apparent work function at an infinite distance from the metal. For larger crystals, when inequivalent facets are exposed to the vacuum, we have shown, with a simple model of the surface dipoles, that the energy required to take an electron to infinity is essentially governed by the face-dependent work functions and the facet surface areas. The exact calculation of the local work function outside a finite crystal is a still-unresolved problem that is more complex than the evaluation of the electrostatic potential. In particular, the contribution of the many-body image force must be included. In this thesis we have calculated, as a first step, the classical distribution of the image potential outside a metallic edge.

A number of other fundamental issues still deserve further study. For example, given an elemental metal and the possibility of choosing the atomic surface arrangement, the minimum and maximum work functions possible for a macroscopic surface have not yet been established. This issue is related to the separation of the work function into an intrinsic component and one related to the specific surface orientation. Increasing the surface step density is known to generally lower the work function but no theory has fixed a definitive lower limit as yet. Further theoretical work is also required to interpret experimental data in crystals other than elemental metals. In view of the directional electronic bonds in semiconductors and the non-vanishing effective charges, the electron affinities of semiconductor surfaces should exhibit an anisotropy at least as strong as the work functions of metals. Indeed, experimental studies are being pursued in this direction, notably for clean and hydrogen-covered diamond surfaces, where an observable work-function anisotropy [153] and a work function reconstruction dependence [154] have been seen. A theoretical study of these new observations would no doubt be most interesting.

The skill to do math on a page
Has declined to the point of outrage.
    Equations quadratica
    Are solved on mathematica,
And on birthdays we don’t know our age.

David Morin, Eric Zaslow, E’beth Haley, John Golden, Nathan Salwen

Appendix A

Calculational details

A.1 Pseudopotential parameters and equilibrium crystal structures

OUR calculations of metal surfaces (in Chapters 4, 5 and 6) are performed at the theoretical equilibrium lattice constants, which must be determined in advance. To obtain these lattice constants, we perform, as a first step, a series of bulk calculations varying the lattice parameter around the estimated equilibrium point. The total energy and the internal stress are calculated in each case using the techniques of Chapter 3. The Troullier-Martins pseudopotentials (see Section 3.5) that we use, both in this section and throughout this thesis, are generated from radial atomic calculations with the parameters shown in Table A.1. For Cu and Au, we have performed relativistic self-consistent determinations of the atomic charge densities.

At equilibrium, the total energy is minimised and a vanishing internal stress is obtained. The equilibrium lattice constant a_0 is determined by fitting the calculated total energies with an empirical Murnaghan equation of state [155]:

$$E(\Omega) = \frac{\Omega_0 B_0}{B_0'} \left[\frac{1}{B_0'-1} \left(\frac{\Omega_0}{\Omega} \right)^{B_0'-1} + \frac{\Omega}{\Omega_0} \right] + E_0 \tag{A.1}$$

where E and Ω are the energy and unit cell volume (the zero subscript indicating the values at equilibrium). B_0 and B_0' are the bulk modulus and its derivative with respect to pressure, respectively:

$$B_0 = \frac{1}{\kappa(\Omega_0)} \tag{A.2}$$

$$B_0' = \frac{\partial B_0}{\partial P}(\Omega_0) \tag{A.3}$$

	Valence	R^s_{cut}	R^p_{cut}	R^d_{cut}	R^f_{cut}	V_L	E_{cut}
Na	$3s^1$	2.50	2.50	2.50		d	16
Al	$3s^2 3p^1$	2.20	2.20	2.20		p	16
Cu	$3d^{10} 4s^1$	2.08	2.08	2.30	2.30	f	70
Au	$5d^{10} 6s^1$	2.50	2.50	2.50		s	40

Table A.1: Parameters of the Troullier-Martins pseudopotentials used in this work: the valence configuration is indicated in the second column. R^i_{cut} is the cutoff radius, in atomic units, for the pseudopotential component i (s, p, d and f), and V_L is the local potential component for the KB approximation. E_{cut} shows the minimum cutoff energy, in Ry, that should be used for the plane-wave expansions of the wave functions.

where $P = -\partial E/\partial\Omega$ is the pressure and $\kappa = -(1/\Omega)(\partial\Omega/\partial P)$ is the compressibility. The Murnaghan equation of state is derived quite generally by assuming that the reciprocal of the compressibility is a linear function of the pressure P.

In the cubic materials examined here, B_0 and B_0' are related [156] to 2nd-order elastic constants (c_{ij}) and 3rd-order stiffness parameters (c_{ijk}), often found in the literature [157], by:

$$\begin{aligned} B_0 &= \frac{c_{11} + 2c_{12}}{3} && \text{(A.4)} \\ B_0' &= 1 - \frac{1}{B_0}\left(c_{112} + \frac{8}{9}c_{456}\right) && \text{(A.5)} \end{aligned}$$

The parameters E_0, Ω_0 (which determines a_0), B_0 and B_0' are fitted to the calculated energy values, as shown in Fig. A.1 for aluminium. The Murnaghan fit is seen to describe correctly both the total energy and the internal stress as the lattice constant is varied. The energy is minimised as the stress vanishes, indicating good convergence with the plane-wave cutoff energy.

The resultant lattice and elastic constants of various metals are displayed in Table A.2, where they are compared to experimental data. Sodium is a body-centered cubic metal; aluminium, copper and gold are face-centered cubic. As often observed within LDA, the lattice constants are slightly underestimated, while the calculated bulk moduli are greater than the experimental data. The values of B_0' are largely indicative, since both theoretical and experimental values suffer from some uncertainties. Nevertheless, the trend between the various metals is correctly reproduced.

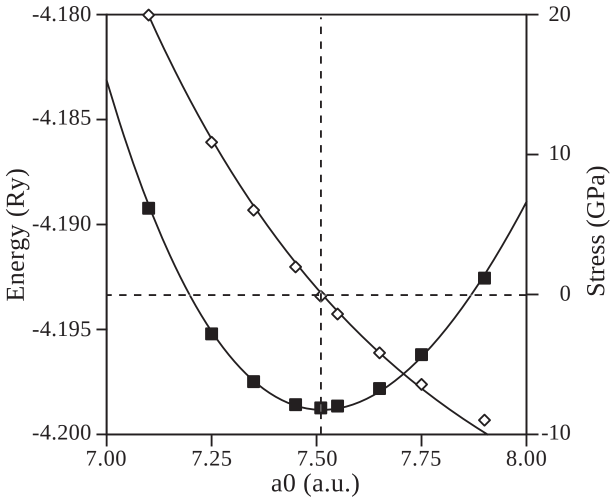

Figure A.1: Determining the theoretical lattice constant of aluminium: Squares: total energy (left-hand scale); Diamonds: internal stress (right-hand scale). The solid lines indicate the result of the Murnaghan fit. Dashed lines show the equilibrium configuration. These calculations were performed with a plane-wave cutoff of 36 Ry and 570 reduced k-points.

	E_{cut}^{bulk}	N_{rkp}	a_0	a_0^{exp}	B_0	B_0^{exp}	B_0'	$B_0'^{exp}$
Na	36	455	7.52	8.00	8.9	6.8	3.7	5.7
Al	36	570	7.51	7.66	85	77	3.6	5.4
Cu	70	570	6.68	6.82	187	140	5.1	6.9
Au	60	408	7.72	7.71	185	170	5.5	6.5

Table A.2: Theoretical equilibrium lattice constants a_0 (a.u.), bulk moduli B_0 (GPa), and their derivatives B_0' for selected metals, calculated using a cutoff E_{cut}^{bulk} (Ry), and N_{rkp} reduced k-points. Experimental values [157] are signaled by *exp* superscripts.

A.2 Macroscopic averages

In our supercell calculations (in Chapters 4, 5 and 6), the charge density $n(\mathbf{r})$ is determined in reciprocal space via its Fourier components $n(\mathbf{G})$, corresponding to plane waves with wave vectors $\mathbf{G} = h\mathbf{b}_1 + k\mathbf{b}_2 + l\mathbf{b}_3$ in the reciprocal lattice. The $\mathbf{b}_i$ (respectively $\mathbf{a}_i$) form the reciprocal (real) basis and h, k, l are integers. The plane waves of kinetic energy up to a certain cutoff are retained in the expansion of $n(\mathbf{r})$:

$$n(\mathbf{r}) = \sum_G n(\mathbf{G}) \exp(i\mathbf{G}\cdot\mathbf{r}), \tag{A.6}$$

$$n(\mathbf{G}) = \frac{1}{\Omega}\int_\Omega \mathbf{dr}\, n(\mathbf{r}) \exp(-i\mathbf{G}\cdot\mathbf{r}), \tag{A.7}$$

where Ω is the volume of the unit cell. If we are interested in plotting a one-dimensional average of the charge density along a basis vector $\mathbf{a}_3$, as is performed in Chapter 4, and assuming that $\mathbf{a}_3$ is orthogonal to $\mathbf{a}_1$ and $\mathbf{a}_2$, only the Fourier

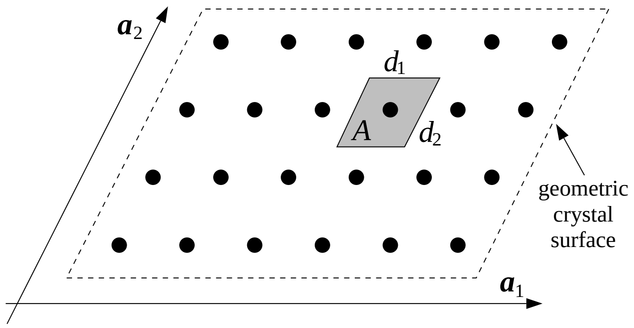

Figure A.2: Two-dimensional macroscopic average over a parallelogram of dimensions (d_1, d_2) and area A (greyed region). The geometric crystal surface is defined at the edge of the macroscopic ionic charge (dashed lines). The black circles show the atomic columns.

components corresponding to multiples of $\mathbf{b}_3$ need be considered in the plane wave expansion of the charge density. The plane-averaged charge density $\overline{n}(z)$ then becomes a one-dimensional periodic function of period $|\mathbf{a}_3|$, which, inside the crystal, exhibits a microscopic atomic-like structure over a distance equal to the lattice interplane spacing d.

In view of obtaining stable reference energies inside a metal, it is interesting to define a macroscopic average of the charge density $\overline{\overline{n}}(z)$ (and subsequently of the potential, see Section 4.4.2) to evacuate the atomic-scale variations of length d, resulting from the crystalline structure. This is accomplished by convoluting the charge with a rectangular step function of width d: $s(z) = 1/d\,\theta(z - d/2)\,\theta(-z + d/2)$, where $\theta(z)$ is the Heaviside function:

$$\overline{\overline{n}}(z) = \int_{-\infty}^{+\infty} \overline{n}(z')\, s(z - z')\, dz' = \frac{1}{d} \int_{z-d/2}^{z+d/2} \overline{n}(z')\, dz'. \tag{A.8}$$

In reciprocal space, the convolution is transformed into a multiplication of the corresponding Fourier components:

$$\overline{\overline{n}}(G) \;=\; \Omega \overline{n}(G) s(G) \;=\; \overline{n}(G) \frac{\sin(Gd/2)}{Gd/2}. \tag{A.9}$$

Since the plane averaging and macroscopic averaging are linear, they commute with the integration of the Poisson equation, leading to exactly similar equations relating the macroscopic potential components $\overline{\overline{V}}(G)$ with the components of the plane-averaged potential $\overline{V}(G)$.

An analogous operation is easily defined in two dimensions, for a planar charge density $\overline{n}(x, y)$. If we choose to average over a rectangular area of size (d_1, d_2) centered around the point of interest, as is performed in Section 6.2, then:

$$\overline{\overline{n}}(G_1, G_2) \;=\; \overline{n}(G_1, G_2) \frac{\sin(G_1 d_1/2)}{G_1 d_1/2} \frac{\sin(G_2 d_2/2)}{G_2 d_2/2}. \tag{A.10}$$

If the real-space units vectors $\mathbf{a}_1$ and $\mathbf{a}_2$ are not orthogonal, the two-dimensional macroscopic average is performed over a small parallelogram of area A, rather than a rectangle (see Figure A.2).

A.3 Electrostatic potential in 1D and 2D

The electrostatic potential $V(\mathbf{r})$ resulting from a charge density $n(\mathbf{r})$ is determined by integrating the Poisson equation $\nabla^2 V(\mathbf{r}) = -8\pi\, n(\mathbf{r})$ (with distances in atomic units and energies in Rydbergs). For charge distributions in one, two, and three dimensions, this leads to the following well-known results :

$$\begin{aligned} \text{1D:} \qquad V(z) &= -4\pi \int dz'\, n^l(z')\, |z - z'| && \text{(A.11)} \\ \text{2D:} \qquad V(\mathbf{r}) &= -4 \int \mathbf{dr}'\, n^s(\mathbf{r}')\, \ln(|\mathbf{r} - \mathbf{r}'|) && \text{(A.12)} \\ \text{3D:} \qquad V(\mathbf{r}) &= 2 \int \mathbf{dr}'\, n(\mathbf{r}')\, \frac{1}{|\mathbf{r} - \mathbf{r}'|} && \text{(A.13)} \end{aligned}$$

where n^l, n^s, and n are respectively the linear, surface and volumetric charge densities.

In one dimension and for a spatially-bounded charge density that sums to zero, the electrostatic potential difference ΔV between the two sides of the charge distribution is given by the charge dipole:

$$\Delta V = 8\pi \int dz\, z\, n^l(z). \tag{A.14}$$

This expression is used to calculate the mean step in electrostatic potential across an infinitely-extended metal surface (see Section 4.4.2).

For extended periodic systems, the integration of the Poisson equation is best performed in reciprocal space. The Fourier components of the potential $V(\mathbf{G})$ are related to those of the charge density $n(\mathbf{G})$ by:

$$V(\mathbf{G}) = \frac{8\pi}{|\mathbf{G}|^2}\, n(\mathbf{G}), \quad \mathbf{G} \neq 0 \tag{A.15}$$

This does not fix the average value of the potential $V(\mathbf{G}\!=\!0)$, which can be chosen arbitrarily in a bulk crystal [158], and is usually set to zero. For a semi-infinite crystal, the average electrostatic potential in the metal is well defined and is fixed by imposing that the potential vanishes in the vacuum at a large distance from the surface.

In two dimensions, if the charge density is bounded by a circle of radius a around the origin, as is the case in our study of nanowires in Section 6.2.2, the

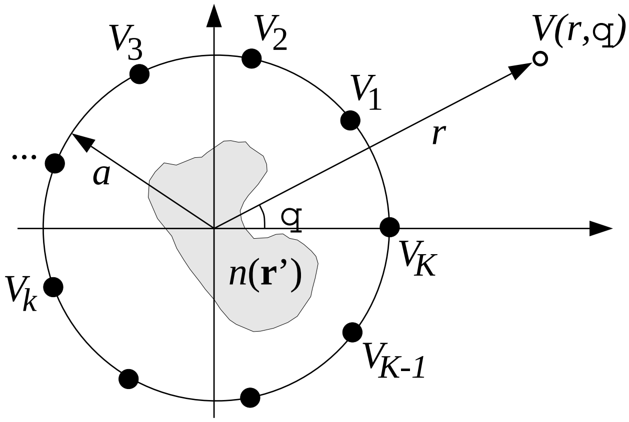

Figure A.3: Implementation of the "multipole method without multipoles" to calculate efficiently the potential $V(\mathbf{r})$, outside a 2D bounded charge density $n(\mathbf{r}')$. The potential is first evaluated at points on a circle of radius a, from which the potential outside the circle can then be determined efficiently.

electrostatic potential $V(r,\theta)$ can be written for $r > a$ as a multipole expansion [159]:

$$V(r,\theta) = -4Q \ln r + \mathrm{Re} \sum_{k=1}^{\infty} \frac{b_k}{r^k} e^{-ik\theta}, \tag{A.16}$$

where Q is the total charge and b_k is the multipole moment of order k:

$$b_k = 4 \int r dr \int d\theta \; n(r,\theta) \frac{r^k e^{ik\theta}}{k}. \tag{A.17}$$

For symmetric charge distributions, a number of coefficients b_k may vanish. For globally neutral systems ($Q = 0$), the asymptotic behaviour of the electrostatic potential for $r \to \infty$ is controlled by the first non-zero b_k coefficient. The decay of the potential is then related to its symmetry: if the potential behaves as $\cos(m(\theta - \theta_0))$, with m angular maxima, it decays as $1/r^m$.

In order to determine the potential in two dimensions around our nanowires (see Section 6.2.2), we have implemented an extension of the fast multipole method, which allows an efficient calculation of the potential at any point $\mathbf{r}$ outside a spatially-bounded charge density [147]. We define a set of points, indexed by k, uniformly distributed on a circle of radius a surrounding the charge density $n(\mathbf{r}')$. We calculate the potential V_k at these points (see Fig. A.3) by an *ad hoc* procedure (explained in Section 6.2.2). The number of points, K, controls the accuracy of the potential calculated at $\mathbf{r}$.

For a total charge density Q and K points distributed around the circle, located at $\mathbf{r} = (r{=}a, \theta{=}s_k)$, with $s_k = 2\pi k/K$, the potential $V(r,\theta)$, in polar coordinates, is then approximated for $r > a$ by:

$$V(r,\theta) \simeq -4Q \ln(r) + \frac{1}{K} \sum_{k=1}^{K} f_k \tag{A.18}$$

$$\frac{1 - (\frac{a}{r})^2 - 2(\frac{a}{r})^{(M+1)} \cos((M+1)(\theta - s_k)) + 2(\frac{a}{r})^{(M+2)} \cos(M(\theta - s_k))}{1 - 2\frac{a}{r}\cos(\theta - s_k) + (\frac{a}{r})^2}$$

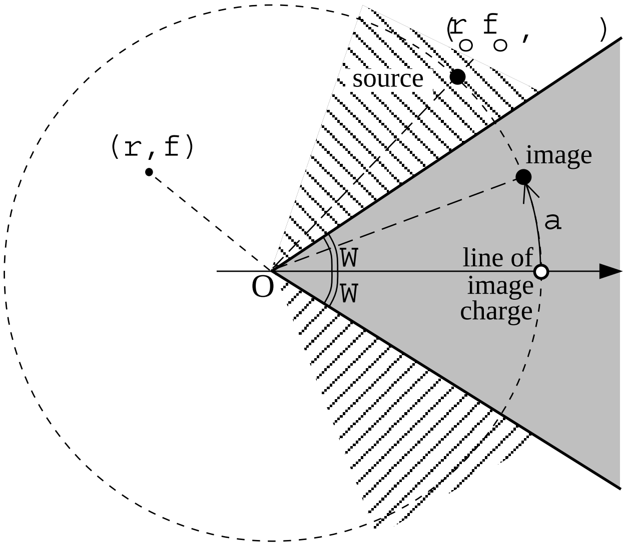

Figure A.4: Classical image charges for a conducting wedge (shaded area) of angle 2Ω. A source charge is located at (ρ_o, ϕ_o) outside the metal. If the source is in the hatched area, a real image is located at $(\rho_o, \alpha = 2\Omega - \phi_o)$. For all external sources, a line of image charge at imaginary angle intersects real space at $(\rho_o, 0)$.

where $K = 2M + 1$, $f_k = V_k + 4Q \ln(a)$, and V_k is the potential at the point $(r = a, \theta = s_k)$. In the case of uncharged crystals, of interest here, we have $Q = 0$.

A.4 Image potential near a conducting wedge

The solution of the three-dimensional Poisson equation for a classical point charge in the presence of a perfectly conducting metallic wedge, of infinite extent and arbitrary angle, has recently been established analytically [151]. The total potential outside the wedge is equal to the sum of the source term created by the point charge and the scattered field induced by the conducting wedge, which can be conveniently formulated in terms of a collection of image sources.

We summarize here only the essential ingredients from Reference 151 that are needed to calculate the image potential presented in Section 6.5. In cylindrical coordinates, the free-space Green function $G(\zeta)$ giving the potential at (ρ, ϕ, z), induced by an electron at (ρ_o, ζ, z_o), is written:

$$G(\zeta) = e^2 / \sqrt{\rho^2 + \rho_o^2 + (z - z_o)^2 - 2\rho\rho_o \cos(\phi - \zeta)}. \tag{A.19}$$

We consider here a wedge of half-angle $\Omega < \pi/2$, which is the case of interest at metal facet edges (see Figure A.4), and a point source at (ρ_o, ϕ_o, z_o), with $\phi_o < \pi$. The angle origin is in the centre of the wedge. The potential induced by sources at greater angles than π can be deduced by symmetry.

The scattered exterior potential $V_s(\rho, \phi, z)$, induced by an electron in the vacuum at (ρ_o, ϕ_o, z_o), can be shown to be written in terms of a real image source in the metal at (ρ_o, α, z_o) and a line of image charge $q_c(\zeta)$ at an imaginary angle ζ:

$$V_s(\rho, \phi, z) = -G(\alpha) + \int_{-i\infty}^{i\infty} q_c(\zeta) G(\zeta) d\zeta. \tag{A.20}$$

The angle α of the real image is given by $\alpha = 2\Omega - \phi_o$, if $\Omega < \phi_o < 2\Omega$. For $\phi_o > 2\Omega$, there is no real image in the wedge. The line of image charge is given as a function of the imaginary angle ζ by:

$$q_c(\zeta) = \frac{i}{2\pi\nu}\left[\frac{\cos(\zeta/\nu)}{\sin(\phi_o/\nu) - \sin(\zeta/\nu)} - \frac{\cos(\zeta/\nu)}{\sin(\alpha/\nu) - \sin(\zeta/\nu)}\right], \tag{A.21}$$

where $\nu = (2\pi - 2\Omega)/\pi$. The line of charge at imaginary angle can be considered to intersect the wedge in real space at the centre of the wedge at $(\rho_o, 0, z_o)$. It should be noted that the values of both image charges are independent of the radial position of the source. The total potential in the vacuum $V(\rho, \phi, z)$ is formed by the sum of the source and the scattered contributions:

$$V(\rho, \phi, z) = G(\phi_o) + V_s(\rho, \phi, z). \tag{A.22}$$

From these considerations, we can extract the image potential around a conducting wedge. The image potential represents the work necessary to move an electron from (ρ_o, ϕ_o, z_o) to infinity, against the force induced by the scattered potential only, taking into account the displacement of the images as the source electron is removed. We evaluate first the radial force F_ρ generated by the scattered potential at (ρ_o, ϕ_o, z_o), due to an electron situated at this same location. By virtue of symmetry, this force is independent of z_o:

$$F_\rho(\rho_o, \phi_o) = \frac{\partial V_s}{\partial \rho}(\rho_o, \phi_o, z_o). \tag{A.23}$$

If the electron is extracted along a straight path radiating from the wedge apex, the work is effected only against F_ρ. We find:

$$F_\rho(\rho_o, \phi_o) = -\frac{e^2}{2\rho_o^2\, 2\sin(\phi_o - \Omega)} - \int_{-i\infty}^{i\infty} q_c(\zeta)\frac{e^2}{2\rho_o^2\, 2\sin((\phi_o - \zeta)/2)}d\zeta. \tag{A.24}$$

The image potential $V_{im}(\rho_o, \phi_o)$ can be then calculated by integrating F_ρ from ρ_o to infinity. The radial integration is easily evaluated, and shows that the image potential is equal to half the static scattered potential evaluated at (ρ_o, ϕ_o, z_o):

$$V_{im}(\rho_o, \phi_o) = \int_{\rho_o}^{\infty} d\rho\ F_\rho(\rho, \phi) = \frac{1}{2}V_s(\rho_o, \phi_o, z_o). \tag{A.25}$$

This last relation between the image potential V_{im} and the scattered part of the total potential V_s is the same as for a planar metallic surface. For an electron at a distance r_o above a laterally-infinite surface, the scattered potential at r_o is $V_s(r_o) = -e^2/2r_o$, while the image potential is $V_{im}(r_o) = -e^2/4r_o$.

A candid professor confesses
That the secret of half his success is
    Not his science, as such,
    Not his marvels so much
As his bright irresponsible guesses.

Thomas Thorneley

Bibliography

[1] H. B. Michaelson. The work function of the elements and its periodicity. J. Appl. Phys. **48** (11), 4729–4733, November 1977.

[2] T. Fauster and W. Steinmann. Two-Photon Photoemission Spectroscopy of Image States. In P. Halevi, editor, *Photonic Probes of Surfaces*, volume 2 of *Electromagnetic Waves: Recent Developments in Research*, chapter 8, pages 347–411. North-Holland, Amsterdam, 1995.

[3] H. B. Michaelson. Relation Between an Atomic Electronegativity Scale and the Work Function. IBM J. Res. Develop. **22** (1), 72–80, January 1978.

[4] N. D. Lang and W. Kohn. Theory of Metal Surfaces: Work Function. Phys. Rev. B **3** (4), 1215–1223, February 1971.

[5] R. Smoluchowski. Anisotropy of the Electronic Work Function of Metals. Phys. Rev. **60**, 661–674, November 1941.

[6] A. Modinos. The electronic work function of the different faces of tungsten. Surf. Sci. **75**, 327–341, 1978.

[7] A. Kiejna and K. F. Wojciechowski. Work Function of Metals: Relation between Theory and Experiment. Progress in Surf. Sci. **11**, 293–338, 1982.

[8] V. Russier and J. P. Badiali. Calculation of the electronic work function of Cu and Ag from an extended jellium model. Phys. Rev. B **39** (18), 13193–13200, June 1989.

[9] M. Heinrichsmeier, A. Fleszar, W. Hanke, and A. G. Eguiluz. Nonlocal density-functional calculations of the surface electronic structure of metals: Application to aluminum and palladium. Phys. Rev. B **57** (23), 14974–14982, June 1998.

[10] G. Schreckenbach, R. Kaschner, and P. Ziesche. Force sum rules, stress theorems and Thomas-Fermi treatment of a 90° jellium edge. Phys. Rev. B **46** (12), 7864–7867, September 1992.

[11] P. Hohenberg and W. Kohn. Inhomogeneous Electron Gas. Phys. Rev. **136** (3B), B864–B871, November 1964.

[12] W. Kohn and L. J. Sham. Self-Consistent Equations Including Exchange and Correlation Effects. Phys. Rev. **140** (4A), A1133–A1138, November 1965.

[13] E. Wigner and J. Bardeen. Theory of the Work Function of Monovalent Metals. Phys. Rev. **48**, 84–87, July 1935.

[14] J. Hölzl and F. K. Schulte. Work Function of Metals. In G. Höhler and E. A. Niekisch, editors, *Solid Surface Physics*, volume 85 of *Springer Tracts in Modern Physics*, chapter 1, pages 1–150. Springer-Verlag, Berlin, 1979.

[15] F. K. Schulte. Chemical potentials and workfunctions of metal surfaces in the theory of an inhomogeneous electron gas. J. Phys. C: Solid State Phys. **7**, L370–L373, 1974.

[16] N. W. Ashcroft and N. D. Mermin. *Solid State Physics*. Saunders College, Philadelphia, 1976.

[17] K. Wandelt. The local work function: Concept and implications. Appl. Surf. Sci. **111**, 1–10, 1997.

[18] A. G. Eguiluz, M. Heinrichsmeier, A. Fleszar, and W. Hanke. First-principles Evaluation of the Surface Barrier for a Kohn-Sham Electron at a Metal Surface. Phys. Rev. Lett. **68** (9), 1359–1362, March 1992.

[19] A. Kiejna and K. F. Wojciechowski. *Metal Surface Electron Physics*. Pergamon, Elsevier, Amsterdam, 1996.

[20] D. P. Woodruff and T. A. Delchar. *Modern techniques of surface science*. CUP, Cambridge, 2nd edition, 1994.

[21] R. G. Forbes. What do we mean by “work function”? In R. J. Behm, N. Garcia, and H. Rohrer, editors, *Scanning Tunneling Microscopy and Related Methods*, NATO ASI Series, Series E: Applied Sciences 184, pages 163–172. Kluwer Academic Publishers, Dordrecht, 1990.

[22] N. A. Burnham, R. J. Colton, and H. M. Pollock. Work-Function Anisotropies as an Origin of Long-Range Surface Forces. Phys. Rev. Lett. **69** (1), 144–147, July 1992.

[23] C. Herring and M. H. Nichols. Thermionic Emission. Rev. Mod. Phys. **21** (2), 185–270, April 1949.

[24] V. Sahni, J. P. Perdew, and J. Gruenebaum. Variational calculations of low-index crystal face-dependent surface energies and work functions of simple metals. Phys. Rev. B **23** (12), 6512–6523, June 1981.

[25] S. Baroni, R. Resta, A. Baldereschi, and M. Peressi. Can we tune the band offset at semiconductor heterojunctions? In G. Fasol, A. Fasolino, and P. Lugli, editors, *Spectroscopy of Semiconductor Microstructures*, pages 251–271. Plenum Publ. Corp., NY, 1989.

[26] S. Lundqvist and N. H. March, editors. *Theory of the Inhomogeneous Electron Gas*. Plenum Press, NY, 1983.

[27] D. A. Kirzhnits. Quantum Corrections to the Thomas-Fermi Equation. Sov. Phys. JETP **5** (1), 64–71, August 1957.

[28] C. F. von Weizsäcker. Zur Theorie der Kernmassen. Zeitschrift für Physik **96**, 431–458, 1935.

[29] B. Krahl-Urban, E. A. Niekisch, and H. Wagner. Work function of stepped tungsten single crystal surfaces. Surf. Sci. **64**, 52–68, 1977.

[30] K. Besocke, B. Krahl-Urban, and H. Wagner. Dipole moments associated with edge atoms; a comparative study on stepped Pt, Au and W surfaces. Surf. Sci. **68**, 39–46, 1977.

[31] H. Ishida and A. Liebsch. Calculation of the electronic structure of stepped metal surfaces. Phys. Rev. B **46** (11), 7153–7156, September 1992.

[32] R. Stumpf and M. Scheffler. *Ab initio* calculations of energies and self-diffusion on flat and stepped surfaces of Al and their implications on crystal growth. Phys. Rev. B **53** (8), 4958–4973, February 1996.

[33] M. W. Finnis and V. Heine. Theory of lattice contraction at aluminum surfaces. J. Phys. F: Metal Phys. **4**, L37–L41, March 1974.

[34] N. D. Lang and W. Kohn. Theory of Metal Surfaces: Induced Surface Charge and Image Potential. Phys. Rev. B **7** (8), 3541–3550, April 1973.

[35] R. Monnier and J. P. Perdew. Surfaces of real metals by the variational self-consistent method. Phys. Rev. B **17** (6), 2595–2611, March 1978.

[36] R. Monnier, J. P. Perdew, D. C. Langreth, and J. W. Wilkins. Change-in-self-consistent-field theory of the work function. Phys. Rev. B **18** (2), 656–666, July 1978.

[37] J. C. Rivière. Work Function: Measurements and Results. In M. Green, editor, *Solid State Surface Science*, volume 1, chapter 4, pages 179–289. Marcel Dekker, New-York, 1969.

[38] Z. Knor. The Interplay of Theory and Experiment in the Field of Surface Phenomena on Metals. In M. W. Roberts and J. M. Thomas, editors, *Surface and Defect Properties of Solids*, volume 6, chapter 3, pages 139–178. The Chemical Society, London, 1977.

[39] G. Chiarotti, editor. *Physics of Solid Surfaces*, volume 24b of *Landolt-Börnstein, New Series III*, chapter 3.1.2.4, pages 56–67. Springer-Verlag, Berlin, 1993.

[40] M. L. Glasser and A. Bagchi. Theories of the photoelectric effect from metal surfaces. Technical Report 76-031, Univ. of Maryland, Center of Materials Research, College Park, Maryland, August 1975.

[41] R. H. Fowler. The analysis of photoelectric sensitivity curves for clean metals at various temperatures. Phys. Rev. **38**, 45–56, July 1931.

[42] J. K. Grepstad, P. O. Gartland, and B. J. Slagsvold. Anisotropic Work Function of Clean and Smooth Low-index Faces of Aluminum. Surf. Sci. **57**, 348–362, 1976.

[43] D. W. Juenker. Electron Emission in Moderate Accelerating Fields. J. Appl. Phys. **28** (12), 1398–1405, December 1957.

[44] M. C. Desjonquères and D. Spanjaard. *Concepts in Surface Physics.* Springer-Verlag, Berlin, 2nd edition, 1996.

[45] R. P. Leblanc, B. C. Vanbrugghe, and F. E. Girouard. Thermionic Emission from a Niobium Single Crystal. Can. J. Phys. **52** (17), 1589–1593, September 1974.

[46] C. H. Hinrichs, W. A. Mackie, I. Cohen, J. Alin, D. Schnitzler, and I. Noel. Work function measurements using an improved thermionic projection microscope. Rev. Sci. Instrum. **65** (12), 3689–3696, December 1994.

[47] C. Oshima, M. Aono, T. Tanaka, S. Kawai, R. Shimizu, and H. Hagiwara. Thermionic emission from single-crystal LaB_6 tips with [100], [110], [111], and [210] orientations. J. Appl. Phys. **51** (2), 1201–1206, February 1980.

[48] J. Politzer and T. E. Feuchtwang. The potential barrier for field emission from a multi-faceted tip, and the extension of the Fowler-Nordheim theory to include patch-fields. Surf. Sci. **19**, 443–463, 1970.

[49] R. M. Wolf, J. W. Bakker, and B. E. Nieuwenhuys. Design and performance of a scanning probe-hole field emission microscope. Surf. Sci. **246**, 420–427, 1991.

[50] J. R. Coaton and A. M. Marsden, editors. *Lamps and Lighting.* Arnold, London, 4th edition, 1997.

[51] M. Nonnenmacher, M. P. O'Boyle, and H. K. Wickramasinghe. Kelvin probe microscopy. Appl. Phys. Lett. **58** (25), 2921–2923, June 1991.

[52] P. A. Anderson. The Contact Difference of Potential Between Tungsten and Barium. The External Work Function of Barium. Phys. Rev. **47**, 958–964, June 1935.

[53] J. T. Yates, Jr. *Experimental Innovations in Surface Science.* Springer-Verlag, Berlin, 1998.

[54] C. Marlière. Quantum size effect detected by work function measurements during indium deposition on polycrystalline, texturized gold substrate. Vacuum **41**, 1192–1194, 1990.

[55] Y. Hasegawa, J. F. Jia, K. Inoue, A. Sakai, and T. Sakurai. Elemental contrast of local work function studied by scanning tunneling microscopy. Surf. Sci. **386**, 328–334, 1997.

[56] J. F. Jia, K. Inoue, Y. Hasegawa, W.S. Yang, and T. Sakurai. Variation of the local work function at steps on metal surfaces studied with STM. Phys. Rev. B **58** (3), 1193–1196, July 1998.

[57] R. García-García and J. J. Sáenz. Is scanning tunneling microscopy a useful tool for probing the surface potential? Surf. Sci. **251/252**, 223–227, 1991.

[58] L. Olesen, M. Brandbyge, M. R. Sørensen, K. W. Jacobsen, E. Lægsgaard, I. Stensgaard, and F. Besenbacher. Apparent Barrier Height in Scanning Tunneling Microscopy Revisited. Phys. Rev. Lett. **76** (9), 1485–1488, February 1996.

[59] J. Jacobsen, B. Hammer, K. W. Jacobsen, and J. K. Nørskov. Electronic structure, total energies, and STM images of clean and oxygen-covered Al(111). Phys. Rev. B **52** (20), 14954–14962, November 1995.

[60] J. M. Pitarke, P. M. Echenique, and F. Flores. Apparent Barrier Height for Tunneling Electrons in STM. Surf. Sci. **217**, 267–275, 1989.

[61] M. C. Payne, M. P. Teter, D. C. Allan, T. A. Arias, and J. D. Joannopoulos. Iterative minimization techniques for *ab initio* total-energy calculations: molecular dynamics and conjugate gradients. Rev. Mod. Phys. **64** (4), 1045–1097, October 1992.

[62] H. L. Skriver and N. M. Rosengaard. Surface energy and work function of elemental metals. Phys. Rev. B **46** (11), 7157–7168, September 1992.

[63] H. Eschrig. *The Fundamentals of Density Functional Theory*, volume 32 of *Teubner-Texte zur Physik.* B. G. Teubner, Stuttgart, 1996.

[64] R. M. Dreizler and E. K. U. Gross. *Density Functional Theory.* Springer-Verlag, Berlin, 1990.

[65] R. O. Jones and O. Gunnarsson. The density functional formalism, its applications and prospects. Rev. Mod. Phys. **61** (3), 689–746, July 1989.

[66] W. Kohn. Density Functional Theory: Fundamentals and Applications. In F. Bassani, F. Fumi, and M. P. Tosi, editors, *Highlights of Condensed-Matter Theory*, pages 1–15, Amsterdam, 1985. Course LXXXIX, International School of Physics "Enrico Fermi", North-Holland.

[67] S. B. Trickey, editor. *Density Functional Theory of Many-Fermion Systems*, volume 21 of *Advances in Quantum Chemistry*. Academic Press, San Diego, 1990.

[68] O. H. Nielsen and R. M. Martin. Quantum-mechanical theory of stress and force. Phys. Rev. B **32** (6), 3780–3791, September 1985.

[69] J. P. Perdew and A. Zunger. Self-interaction correction to density-functional approximations for many-electron systems. Phys. Rev. B **23** (10), 5048–5079, May 1981.

[70] D. M. Ceperley and B. J. Alder. Ground State of the Electron Gas by a Stochastic Method. Phys. Rev. Lett. **45** (7), 566–569, August 1980.

[71] J. P. Perdew, J. A. Chevary, S. H. Vosko, K. A. Jackson, M. R. Pederson, D. J. Singh, and C. Fiolhais. Atoms, molecules, solids, and surfaces: Applications of the generalized gradient approximation for exchange and correlation. Phys. Rev. B **46** (11), 6671–6687, September 1992.

[72] S. Ossicini, C. M. Bertoni, and P. Gies. Non-local exchange and correlation in the jellium model of surfaces. Surf. Sci. **178**, 244–255, 1986.

[73] J. E. Alvarellos and E. Chacón. Self-consistent weighted density approximation for simple metal surfaces. Surf. Sci. **269/270**, 590–595, 1992.

[74] J. Ihm, A. Zunger, and M. L. Cohen. Momentum-space formalism for the total energy of solids. J. Phys. C: Solid State Phys. **12**, 4409–4422, 1979.

[75] H. J. Monkhorst and J. D. Pack. Special points for Brillouin-zone integrations. Phys. Rev. B **13** (12), 5188–5192, June 1976.

[76] A. Baldereschi. Mean-Value Point in the Brillouin Zone. Phys. Rev. B **7** (12), 5212–5215, June 1973.

[77] S. Froyen. Brillouin-zone integration by Fourier quadrature: Special points for superlattice and supercell calculations. Phys. Rev. B **39** (5), 3168–3172, February 1989.

[78] C.-L. Fu and K.-M. Ho. First-principles calculations of the equilibrium ground-state properties of transition metals: Applications to Nb and Mo. Phys. Rev. B **28** (10), 5480–5486, November 1983.

[79] F. Wagner, Th. Laloyaux, and M. Scheffler. Errors in Hellman-Feynman forces due to occupation-number broadening and how they can be corrected. Phys. Rev. B **57** (4), 2102–2107, January 1998.

[80] M. Aldén, H. L. Skriver, and B. Johansson. Surface core-level shifts for simple metals. Phys. Rev. B **50** (16), 12118–12130, October 1994.

[81] W. E. Pickett. Pseudopotential methods in condensed matter applications. Computer Physics Reports **9**, 115–198, 1989.

[82] N. Troullier and J. L. Martins. Efficient pseudopotentials for plane-wave calculations. Phys. Rev. B **43** (3), 1993–2006, January 1991.

[83] L. Kleinman and D. M. Bylander. Efficacious Form for Model Pseudopotentials. Phys. Rev. Lett. **48** (20), 1425–1428, May 1982.

[84] M. Methfessel, D. Hennig, and M. Scheffler. Trends of the surface relaxations, surface energies, and work functions of the $4d$ transition metals. Phys. Rev. B **46** (8), 4816–4829, August 1992.

[85] J. C. Boettger, U. Birkenheuer, S. Krüger, N. Rösch, and S. B. Trickey. Theoretical investigation of Na adsorption on the Al(111) surface. Phys. Rev. B **52** (3), 2025–2031, July 1995.

[86] J. Neugebauer and M. Scheffler. Adsorbate-substrate and adsorbate-adsorbate interactions of Na and K adlayers on Al(111). Phys. Rev. B **46** (24), 16067–16080, December 1992.

[87] F. K. Schulte. A theory of thin metal films: electron density, potentials and work function. Surf. Sci. **55**, 427–444, 1976.

[88] P. J. Feibelman and D. R. Hamann. Quantum-size effects in work functions of free-standing and adsorbed thin metal films. Phys. Rev. B **29** (12), 6463–6467, June 1984.

[89] I. P. Batra, S. Ciraci, G. P. Srivastava, J. S. Nelson, and C. Y. Fong. Dimensionality and size effects in simple metals. Phys. Rev. B **34** (12), 8246–8257, December 1986.

[90] J. C. Boettger and S. B. Trickey. Quantum size effects in equilibrium lithium ultrathin layers. Phys. Rev. B **45** (3), 1363–1372, January 1992.

[91] J. C. Boettger. Persistent quantum-size effect in aluminum films up to twelve atoms thick. Phys. Rev. B **53** (19), 13133–13137, May 1996.

[92] C. J. Fall, N. Binggeli, and A. Baldereschi. Deriving accurate work functions from thin-slab calculations. J. Phys. C: Condens. Matter **11** (13), 2689–2696, April 1999.

[93] A. Zunger and A. J. Freeman. Self-consistent numerical-basis-set linear-combination-of-atomic-orbitals model for the study of solids in the local density formalism. Phys. Rev. B **15** (10), 4716–4737, May 1977.

[94] J. E. Jaffe and A. C. Hess. Gaussian basis density functional theory for systems periodic in two or three dimensions: Energy and forces. J. Chem. Phys. **105** (24), 10983–10998, December 1996.

[95] J. R. Chelikowsky, M. Schlüter, S. G. Louie, and M. L. Cohen. Self-consistent Pseudopotential Calculation for the (111) Surface of Aluminum. Solid State Comm. **17**, 1103–1106, 1975.

[96] G. Bastard. *Wave mechanics applied to semiconductor heterostructures.* Editions de physique, Les Ulis, France, 1990.

[97] C. Berthod, N. Binggeli, and A. Baldereschi. Formation energy, lattice relaxation, and electronic structure of Al/Si/GaAs(100) junctions. Phys. Rev. B **57** (16), 9757–9762, April 1998.

[98] A. Hamawi and L. Walldén. Quantum size effect for Na films on Si(100). Surf. Sci. **285**, 93–101, 1993.

[99] J. P. Harbison, T. Sands, R. Ramesh, N. Tabatabaie, H. L. Gilchrist, L. T. Florez, and V. G. Keramidas. Metallic quantum wells grown by molecular-beam epitaxy. J. Vac. Sci. Technol. B **8** (2), 242–245, Mar/Apr 1990.

[100] H. Erschbaumer, A. J. Freeman, C. L. Fu, and R. Podloucky. Surface states, electronic structure and surface energy of the Ag(001) surface. Surf. Sci. **243**, 317–322, 1991.

[101] M. Heinrichsmeier, A. Fleszar, and A. G. Eguiluz. LDA calculation of the surface states on the (001), (110), and (111) surfaces of aluminum. Surf. Sci. **285**, 129–141, 1993.

[102] K.-P. Bohnen and K.-M. Ho. First principles calculations of lattice relaxation and surface phonons on Al(100). Surf. Sci. **207**, 105–117, 1988.

[103] L. Reinaudi, M. Del Popolo, and E. Leiva. Work function calculation for thick metal slabs with local pseudopotentials. Surf. Sci. **372**, L309–L314, 1997.

[104] C.-O. Almbladh and U. von Barth. Exact results for the charge and spin densities, exchange-correlation potentials, and density-functional eigenvalues. Phys. Rev. B **31** (6), 3231–3244, March 1985.

[105] C. J. Fall, N. Binggeli, and A. Baldereschi. Anomaly in the anisotropy of the aluminum work function. Phys. Rev. B **58** (12), R7544–R7547, September 1998.

[106] T. Rodach, K.-P. Bohnen, and K.-M. Ho. First-principles study of the Na(110) surface. Surf. Sci. **209**, 481–491, 1989.

[107] J. P. Rogers III, J. S. Nelson, P. H. Cutler, and T. E. Feuchtwang. First-principles method for calculating electronic properties of layered structures. Phys. Rev. B **40** (6), 3638–3642, August 1989.

[108] K.-P. Bohnen. Lattice relaxation at alkali metal surfaces. Surf. Sci. **147**, 304–328, 1984.

[109] J. M. MacLaren, J. B. Pendry, P. J. Rous, D. K. Saldin, G. A. Somorjai, M. A. Van Hove, and D. D. Vedensky. *Surface Crystallographic Information Service: A Handbook of Surface Structures.* D. Reitel, 1987.

[110] J. R. Noonan and H. L. Davis. Confirmation of an exception to the "general rule" of surface relaxations. J. Vac. Sci. Technol. A **8** (3), 2671–2676, May/June 1990.

[111] H. L. Davis, J. B. Hannon, K. B. Ray, and E. W. Plummer. Anomalous interplanar expansion at the (0001) surface of Be. Phys. Rev. Lett. **68** (17), 2632–2635, April 1992.

[112] J. N. Andersen, H. B. Nielsen, L. Petersen, and D. L. Adams. Oscillatory relaxation of the Al(110) surface. J. Phys. C: Solid State Phys. **17**, 173–192, 1984.

[113] A. Ruini, R. Resta, and S. Baroni. Dynamical-charge neutrality at a crystal surface. Phys. Rev. B **57** (10), 5742–5745, March 1998.

[114] M. Weinert and R. E. Watson. Contributions to the work function of crystals. Phys. Rev. B **29** (6), 3001–3008, March 1984.

[115] W. Gordy. A New Method of Determining Electronegativity from Other Atomic Properties. Phys. Rev. **69** (11–12), 604–607, June 1946.

[116] P. O. Gartland. Anisotropy in the photoelectric work function of a copper single crystal. Physica Norvegica **6**, 201, 1972.

[117] J. Lecoeur, J. P. Bellier, and C. Koehler. Comparison of crystallographic anisotropy effects on potential of zero charge and electronic work function for gold (111), (311), (110) and (210) orientations. Electrochimica Acta **35** (9), 1383–1392, 1990.

[118] G. V. Hansson and S. A. Flodström. Photoemission study of the bulk and surface electronic structure of single crystals of gold. Phys. Rev. B **18** (4), 1572–1585, August 1978.

[119] S. G. Louie, S. Froyen, and M. L. Cohen. Nonlinear ionic pseudopotentials in spin-density-functional calculations. Phys. Rev. B **26** (4), 1738–1742, August 1982.

[120] J. W. Davenport, R. E. Watson, and W. Weinert. Linear augmented Slater-type orbital method for electronic structure calculations. III. Structural and cohesive energies of the 5*d* elements Lu-Au. Phys. Rev. B **32** (8), 4883–4891, October 1985.

[121] S. Å. Lindgren, L. Walldén, J. Rundgren, and P. Westrin. Low-energy electron diffraction from Cu(111): Subthreshold effect and energy-dependent inner potential; surface relaxation and metric distances between spectra. Phys. Rev. B **29** (2), 576–588, January 1984.

[122] R. Mayer, C.-S. Zhang, K. G. Lynn, W. E. Frieze, F. Jona, and P. M. Marcus. Low-energy electron and positron diffraction measurements and analysis on Cu(100). Phys. Rev. B **35** (7), 3102–3110, March 1987.

[123] H. L. Davis and J. R. Noonan. Multilayer relaxation in metallic surfaces as demonstrated by LEED analysis. Surf. Sci. **126**, 245–252, 1983.

[124] D. Vanderbilt. Soft self-consistent pseudopotentials in a generalized eigenvalue formalism. Phys. Rev. B **41** (11), 7892–7895, April 1990.

[125] N. Takeuchi, C. T. Chan, and K. M. Ho. Au(110): A theoretical study of the surface reconstruction and the surface electronic structure. Phys. Rev. B **43** (17), 13899–13906, June 1991.

[126] D. L. Abernathy, D. Gibbs, G. Grübel, K. G. Huang, S. G. J. Mochrie, A. R. Sandy, and D. M. Zehner. Reconstruction of the (111) and (001) surfaces of Au and Pt: thermal behavior. Surf. Sci. **283**, 260–276, 1993.

[127] Y.-F. Liew and G.-C. Wang. High resolution low energy electron diffraction characterization of reconstructed Au(100) surfaces. Surf. Sci. **227**, 190–196, 1990.

[128] M. Copel, P. Fenter, and T. Gustafsson. The reconstruction and relaxation of Ir(110) and Au(110) surfaces. J. Vac. Sci. Technol. A **5** (4), 742–746, Jul/Aug 1987.

[129] E. Vlieg, I. K. Robinson, and K. Kern. Relaxations in the missing-row structure of the (1x2) reconstructed surfaces of Au(110) and Pt(110). Surf. Sci. **233**, 248–254, 1990.

[130] L. L. Kesmodel and L. M. Falicov. The electronic potential in a metal close to a surface edge. Solid State Comm. **16**, 1201 –1204, 1975.

[131] V. T. Binh. Characterization of microtips for scanning tunneling microscopy. Surf. Sci. **202**, L539–L549, 1988.

[132] H. Ohnishi, Y. Kondo, and K. Takayanagi. Quantized conductance through individual rows of suspended gold atoms. Nature **395**, 780–783, October 1998.

[133] T. Kizuka, K. Yamada, S. Deguchi, M. Naruse, and N. Tanaka. Cross-sectional time-resolved high-resolution transmission electron microscopy of atomic-scale contact and noncontact-type scannings on gold surfaces. Phys. Rev. B **55** (12), R7398–R7401, March 1997.

[134] J. I. Pascual, J. Méndez, J. Gómez-Herrero, A. M. Baró, N. García, and V. T. Binh. Quantum Contact in Gold Nanostructures by Scanning Tunneling Microscopy. Phys. Rev. Lett. **71** (12), 1852–1855, September 1993.

[135] F. J. Himpsel, T. Jung, and J. E. Ortega. Nanowires on stepped metal surfaces. Surf. Rev. and Lett. **4** (2), 371–380, 1997.

[136] A. A. Setlur, J. M. Lauerhaas, J. Y. Dai, and R. P. H. Chang. A method for synthesizing large quantities of carbon nanotubes and encapsulated copper nanowires. Appl. Phys. Lett. **69** (3), 345–347, July 1996.

[137] A. I. Yanson, G. R. Bollinger, H. E. van den Brom, N. Agraït, and J. M. van Ruitenbeek. Formation and manipulation of a metallic wire of single gold atoms. Nature **395**, 783–785, October 1998.

[138] O. Gülseren, F. Ercolessi, and E. Tosatti. Noncrystalline Structures of Ultrathin Unsupported Nanowires. Phys. Rev. Lett. **80** (17), 3775–3778, April 1998.

[139] G. Taraschi, J.-L. Mozos, C. C. Wan, H. Guo, and J. Wang. Structural and transport properties of aluminum atomic wires. Phys. Rev. B **58** (19), 13138–13145, November 1998.

[140] R. N. Barnett and U. Landman. Cluster-derived structures and conductance fluctuations in nanowires. Nature **387**, 788–791, June 1997.

[141] A. N. Smogunov, L. I. Kurkina, S. I. Kurganskii, and O. V. Farberovich. Electronic structure of simple metal whiskers. Surf. Sci. **391**, 245–251, 1997.

[142] C. Yannouleas, E. N. Bogachek, and U. Landman. Energetics, forces, and quantized conductance in jellium-modeled metallic nanowires. Phys. Rev. B **57** (8), 4872–4882, February 1998.

[143] P. A. Serena and N. García, editors. *Nanowires*, volume 340 of *NATO ASI Series, Series E: Applied Sciences*. Kluwer, Dordrecht, 1997.

[144] J. S. Kasper and K. Lonsdale, editors. *International Tables for X-Ray Crystallography*, volume II. Kluwer, Dordrecht, 3rd edition, 1989.

[145] J. P. Perdew, H. Q. Tran, and E. D. Smith. Stabilized jellium: Structureless pseudopotential model for the cohesive and surface properties of metals. Phys. Rev. B **42** (18), 11627–11636, December 1990.

[146] A. Zangwill. *Physics at Surfaces*. CUP, Cambridge, 1988.

[147] Ch. R. Anderson. An implementation of the fast multipole method without multipoles. SIAM J. Sci. Stat. Comput. **13** (4), 923–947, July 1992.

[148] E. Durand. *Électrostatique*, volume I–II. Masson & Cie, Paris, 1966.

[149] H. Singer, H. Steinbigler, and P. Weiss. A charge simulation method for the calculation of high voltage fields. IEEE Trans. Power Apparatus and Systems **PAS-93** (5), 1660–1668, 1974.

[150] N. H. Malik. A Review of the Charge Simulation Method and its Applications. IEEE Trans. Elec. Insulation **24** (1), 3–20, February 1989.

[151] K. I. Nikoskinen and I. V. Lindell. Image Solution for Poisson's Equation in Wedge Geometry. IEEE Trans. on Antennas and Propagation **45** (2), 179–187, February 1995.

[152] A. G. Eguiluz and W. Hanke. Evaluation of the exchange-correlation potential at a metal surface from many-body perturbation theory. Phys. Rev. B **39** (14), 10433–10436, May 1989.

[153] L. Diederich, O. M. Kuttel, P. Aebi, and L. Schlapbach. Electron affinity and work function of differently oriented and doped diamond surfaces determined by photoelectron spectroscopy. Surf. Sci. **418**, 219–239, 1998.

[154] G. R. Brandes and A. P. Mills, Jr. Work function and affinity changes associated with the structure of hydrogen-terminated diamond (100) surfaces. Phys. Rev. B **58** (8), 4952–4962, August 1998.

[155] F. D. Murnaghan. The compressibility of media under extreme pressures. Proc. N. A. S. **30**, 244–247, 1944.

[156] F. D. Murnaghan. *Finite Deformations of an Elastic Solid.* Wiley, New York, 1951.

[157] K.-H. Hellwege, editor. *Physics of Solid Surfaces*, volume 11 of *Landolt-Börnstein, New Series III*, pages 1–11, 256–277. Springer-Verlag, Berlin, 1979.

[158] L. Kleinman. Comment on the average potential of a Wigner solid. Phys. Rev. B **24** (12), 7412–7414, December 1981.

[159] P. M. Morse and H. Feshbach. *Methods of theoretical physics*, volume 2. McGraw-Hill, New-York, 1953.

[160] E. O. Parrott, editor. *The Penguin Book of Limericks.* Penguin, London, 1983.

[161] D. E. Knuth. *Computers & Typesetting*, volume A. Addison Wesley, Reading, Massachusetts, 1986.

[162] L. Lamport. *A Document Preparation System: LaTeX, User's Guide & Reference manual.* Addison Wesley, Reading, Massachusetts, 1986.

[163] R. Seroul and S. Levy. *A Beginner's Book of TeX.* Springer-Verlag, New-York, 1991.

A quantum mechanic's vacation
Had his colleagues in dire consternation.
    For while studies had shown
    That his speed was well known,
His position was pure speculation.

Anon

Acknowledgements

THIS work could not have begun without the presence of Dr. Nadia Binggeli, who not only introduced me to the field of *ab initio* calculations, but also taught me how me proceed with rigourous scientific research. Nadia is the only person to have followed this project on a regular basis, and her strong support during the daily ups and downs was most appreciated.

I would also like to thank Prof. Baldereschi for accepting me as a PhD student and for suggesting an investigation into the field of work functions. I fully appreciated the freedom I was granted in organising my time and my research.

Special thanks to my friends Julien Bardi, Claude-Alain Piguet and Alain Bally for numerous coffees, lunches, and holidays together. And to Fabio Favot and Kamran "Kami" Houshangpour for bringing their perpetual good spirits to the Institute. Thanks to Fabian Zwick, Pablo Fernández and Giovanni Cangiani for consecutively sharing my office, and to Max Di Ventra and the other members of the IPA for further discussions.

I am very grateful and most honoured that Dr W. Andreoni, Prof. F. Bassani and Prof. K. Kern have accepted to be members of the jury.

Finally, I thank my family for always being extremely supportive during these long years of study, even though my field of expertise has sometimes seemed slightly mysterious in their eyes.

Lausanne, February 1999 *C. J. Fall*

The limericks are taken from [160] as well as from the American Physical Society web pages (www.aps.org/apsnews). The opinions presented in these poems do not necessarily coincide with those of the author of this thesis. The historical photos come from a variety of web sources, most notably from the History of Mathematics archive (www-history.mcs.st-andrews.ac.uk/history) and the Nobel prize web site (www.nobel.se).

The calculations were performed at EPF-Lausanne on a CRAY Y-MP/M94, a DEC alphaserver 4100 5/400, a Silicon Graphics Indigo 2 workstation and a Macintosh 7600/1200, as well as at the CSCS in Manno, Ticino, on a NEC SX-4/16 Supercomputer.

This document was typeset with LaTeX [161–163] on March 15, 2003 at 10:39.

‘‘I’m English!’’ he said, with a scowl
‘‘My name, I should think, would be ‘Joule’
    And yet, as a rule
    I must answer to ‘Joule’ -
Confound that ambiguous vow’l!’’

Edward H. Green

Curriculum Vitæ

Nom	**FALL**
Prénoms	**Caspar James**
Né	le 7 janvier 1972
à	Welwyn Garden City, Angleterre
Nationalité	Britannique

1995–1999	Doctorant à l'Institut de Physique Appliquée, EPFL, Lausanne dès octobre 1996: Assistant pour le cours d'expérimentation numérique du Prof. A. Baldereschi octobre 1995 - octobre 1996: Assistant pour le cours avancé de physique du solide du Prof. A. Baldereschi et du Prof. A. Quattropani
mars 1995	Diplôme d'Ingénieur Physicien EPFL Travail pratique de diplôme, intitulé *Two-dimensional Quantum Confinement in Crescent-Shaped Quantum Wires*, réalisé à l'Institut de Micro- et Optoélectronique, sous la direction du Prof. E. Kapon
1990–1995	Etudes de Physique, EPFL, Lausanne
juin 1990	Maturité scientifique (type C)
1987–1990	Gymnase de Chamblandes, Pully, Vaud